8-20-2021

Laser Surface Treatment and Laser Powder Bed Fusion Additive Manufacturing Study Using Custom Designed 3D Printer and the Application of Machine Learning in Materials Science

Hao Wen

LASER SURFACE TREATMENT AND LASER POWDER BED FUSION ADDITIVE MANUFACTURING STUDY USING CUSTOM DESIGNED 3D PRINTER AND THE APPLICATION OF MACHINE LEARNING IN MATERIALS SCIENCE

A Dissertation

Submitted to the Graduate Faculty of the
Louisiana State University and
Agricultural and Mechanical College
in partial fulfillment of the
requirements for the degree of
Doctor of Philosophy

in

The Department of Engineering Science

by
Hao Wen
B.A., Jimei University, China, 2012
M.S., Stevens Institute of Technology, New Jersey, 2014
Ph.D., Louisiana State University
December 2021

Acknowledgements

All chapters of this dissertation are supported by the National Science Foundation, Consortium for innovation in manufacturing and materials (CIMM) program (grant number # OIA-1541079), and Louisiana Materials Design Alliance (LAMDA, grant number NSF #OIA-1946231).

Table of Contents

List of Tables

List of Figures

Abstract

Selective Laser Melting (SLM) is a laser powder bed fusion (L-PBF) based additive manufacturing (AM) method, which uses a laser beam to melt the selected areas of the metal powder bed. A customized SLM 3D printer which can handle small quantity of metal powders was built in the lab to achieve versatile research purposes. The hardware design, electrical diagrams and software functions are introduced in Chapter 2. Several laser surface engineering and SLM experiments were conducted using this customized machine which showed the functionality of the machine and some prospective fields that this machine can be utilized. Chapter 3 evaluated the effects of laser beam irradiation-based surface modifications of Ti-10Mo alloy samples under either Ar or N_2 environment to the corrosion resistance and cell integration properties. The customized 3D printer was used to conduct the laser surface treatment. The electrochemical behaviors of the Ti-10Mo samples were evaluated in simulated body fluid maintained at 37 ± 0.5℃, and a cell-material interaction test was conducted using the MLO-Y4 cells. Laser surface modification in the Ar environment was found to enhance corrosion behavior, but did not affect the surface roughness, element distribution or cell behavior, compared to the non-laser scanned samples. Processing the Ti-10Mo alloy in N_2 formed a much rougher TiN surface that improved both the corrosion resistance and cell-material integration compared with the other two conditions. The mechanical behavior of spark plasma sintering (SPS) treated SLM Inconel 939 samples was evaluated in Chapter 4. Flake-like precipitates (η and σ phases) are observed on 800-SPS sample surface which increased the hardness and tensile strength compared with the as-fabricated samples. However, the strain-to-failure value decreased due to the local stress concentration. γ’/ γ’’ phases were formed on 1200-SPS sample. Although not fully formed due to the short holding time, 1200-SPS sample still showed the highest hardness value and best tensile strength and deductibility. Apply machine learning to materials science field was discussed at the fifth chapter. Firstly, a simple

(Deep Neural Network) DNN model is created to predict the Anti-phase Boundary Energy (APBE) based on the limited training data. It achieves the best performance compared with Random Forest Regressor model and K Neighbors Regressor model. Secondly, the defects classification, the defects detection, and the defects image segmentation are successfully performed using a simple CNN model, YOLOv4 and Detectron2, respectively. Furthermore, defects detection is successfully applied on video by using a sequence of CT scan images. It demonstrates that Machine Learning (ML) can enable more efficient and economical materials science research.

Chapter 1. Introduction

1.1 Background

Selective laser melting (SLM) is one of the new additive manufacturing techniques that became popular in recent few decades [1][2]. During the SLM process, a high-power laser is used to melt the selected areas of a powder bed, e.g. Stainless-Steel powders and Ti–6Al–4V powders are the most used powders. The metal powders will form a liquid molten pool if sufficient laser power is applied. Afterwards, the molten pool solidifies at a very high cooling rate and the consolidated material starts to form the product. After the cross-section of a layer is scanned, the building platform is lowered by an amount equal to the layer thickness and a new layer of powder is deposited (Figure 1.1). This process is repeated until the product is completed. After the process, the unused powder is sieved and can be reused for several times [3]. Compared with other conventional manufacturing techniques, SLM can have direct production of complex geometries based on a CAD model with high flexibility and accuracy. Besides, the fine micro-structures formed by the high cooling rate can be beneficial to certain applications [2]. However, this new technique also has some frequently observed drawbacks, such as high thermal stress, segregation phenomena, high porosity and crack concentrations etc. [3]. These problems can be improved by adjusting some of the laser parameters, for example laser power, laser spot size, scanning speed and strategy, hatch space and powder layer thickness. Additionally, a suitable powder material is a strong foundation for a successful parametric development [4]. The material properties of the metal powder, such as the surface tension, thermal conductivity and melting point etc. can play a large role [3]. For the development of new metal powders for SLM, all the above parameters need to be considered and the process is very difficult to simulate using computer software. As a result, a large amount of experiments needs to be conducted to develop a new powder with suitable laser processing parameters. Within a typical lab environment, only a small quantity of metal

powders can be achieved for exploring new alloys. However, even for the smallest commercial machine on the market, which still requires at least about 5 kilograms of powders to fill the chamber. As a result, a machine which can handle small quantity of metal powders and with the capability of adjusting all 3D printing parameters need to be developed for lab research purpose.

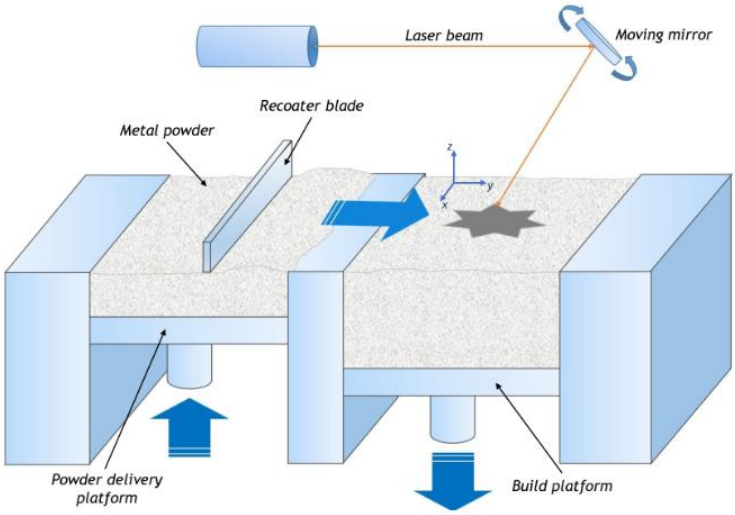

Figure 1.1. The Selective Laser Melting (SLM) process [5]

Laser surface engineering is another important area of laser application. It offers several advantages over other surface modification techniques because of the non-equilibrium synthesis. The super high cooling rates (>10^5 K/s) can produce metastable phases by exceeding the solid solubility limit beyond equilibrium phase diagram [5]. This leads to development of wide variety of microstructures with novel properties which cannot be produced by any conventional processing technique [6]. As a result, Laser surface engineering has been widely used for altering the surface composions and microstructures to improve surface properties of differing materials [6][7]. Among which, many laser modifications of metal surfaces have been studied to improve base material biocompatibilities and corrosion resistance. Laser beam irradiation can alter the sample surface roughness and chemical compositions. For a medical implant to be successful, bone and tissue must be able to adhere to the implant and remain healthy. Cell protein adsorption, receptor-ligand binding, signal transduction, and cell

attachment are significantly affected by implant surface morphologies and chemical compositions [8]. As a result, the surface morphology and chemical compositions of metallic medical implants strongly affect osseointegration, healing time, and tissue regeneration [9]. Therefore, properly engineered implant surfaces play a critical role in tissue health, adherence and ultimately the success of an implant. Within the process of developing a custermized SLM 3D printer, I exploered the biomedical properties of Ti-10Mo alloy by scanning the sample surfaces in different gas atomosphere and evaluate how the corrosion resistance and cell integration properties of Ti-10Mo alloy would alter, undergoing laser beam irradiation based surface modifications in either a pure Ar or a N_2 environment.

The high temperature Inconel alloys are intensively used in the aerospace and industrial gas turbines due to their outstanding oxidation resistance and creep properties [10,11]. Among them, IN 718 is a successful example in the application for hot structures with complex geometries due to the low levels of Al and Ti [11,12]. However, because of the coarsening of the γ" phase, the IN 718 only has very limited use above 650 °C [11]. IN 939 is a γ' hardening alloy which has higher temperature capability with adequate strength and weldability [11]. The SLM process can build the parts layer by layer with very complex geometries, and this technology has been used in manufacturing aerospace, automotive and medical devices [13]. Since the outstand advantages of SLM, many researchers have been trying to 3D print nickel-based super alloys. However, in the application of SLM printing IN 939, the SLM parts usually contain defects such as pores and cracks due to the high thermal stress and micro-segregation that are caused by the ultra-high temperature gradient and cooling rate during the laser processing [12–15]. Therefore, post-heat treatments need to be conducted to satisfy the requirements of service conditions. The traditional heat treatments (i.e. annealing, ageing) can only help to develop the desired phases of the material but have limited effects on eliminating the defects in SLM samples. Spark Plasma Sintering (SPS) treatment, which is commonly used

for powder materials, exerts a pulsed DC current with a uniaxial pressure on the sample, and generates a rapid heating in the sample. By applying SPS heat treatment on 3D printed IN 939 samples, the defects inside the sample can be eliminated due to plastic deformation, creep, and diffusion bonding. Therefore, SPS treatment can be an alternative way for post heat treatment of SLM IN 939 samples.

Machine learning has been widely applied in many areas like computer vision, general game playing, economics, data mining and bioinformatics [16–19]. Besides of the mainstream artificial intelligence field, many experts in other fields are exploring to use machine learning in their own objectives and materials science is one of the areas [20]. With the development of modern technologies, many crucial and diverse requirements for materials have been imposed by customers from many different fields, such as information science, energy, national defense, and many other areas. However, traditional methods for discovering new materials, such as the empirical trial and error method, the density functional theory (DFT)-based method and molecular dynamic (MD) simulations typically require a long research and development cycle and have difficulties keeping pace with the needs for development of materials science today. Machine learning can substantially reduce the computational costs and shorten the development cycle; hence, it is one of the most efficient ways of replacing DFT calculations, MD simulations or even repetitive laboratory experiments [20]. Among the machine learning models, deep learning is a family of machine learning methods that use multiple processing layers to learn data representations and it has made new progress in the application of data-driven methods in the field of materials science [20]. For example, Convolutional Neural Networks (CNN), Recurrent Neural Networks (RNN) and deep coding networks have demonstrated the capabilities in material detections, material analysis, material design and quantum chemistry [21–24]. Because of the layer by layer building process of SLM, the scanning strategies can be adjusted based on the characteristics of each layer. As a result, CNN

is a potential model in analyzing the SLM processing images to improve the part quality. Therefore, different deep learning models are applied to materials topics, such as predicting antiphase boundary energy (APBE), Scanning Electron Microscope (SEM) image defects recognitions. The DNN model is compared with other commonly used ML models in predicting the APBE, and the defects recognition has been achieved in three different complexity levels, namely the defects classification, the defects detection, and the defects image segmentation. Finally, the trained ML model is used to detect defects on CT scan videos, which provide the possibilities on SLM in-situ monitoring and eliminating defects during the printing process.

1.2. Outline of the manuscript

This manuscript includes five chapters. Chapter 1 shows the introduction and the outline of this manuscript. Chapter 2 presents the design of a custom-built 3D printer and some studies which were conducted by this machine. Chapter 3 is the study of laser surface modification of Ti-10Mo Alloy under Ar and N_2 environment for biomedical application; Chapter 4 shows the preliminary results of studying the mechanical properties of 3D printed Inconel 939 made by the Selective Laser Melting method. Chapter 5 includes the deep learning models for the potential applications of predicting antiphase boundary energy (APBE), and for the potential applications of Scanning Electron Microscope (SEM) image defects recognition with three different levels of complexities. The trained machine learning model can also be applied on videos which can be used for in-situ 3D printing monitoring.

Chapter 2. The Design of a Custom 3D Printer for Lab Research

2.1. Introduction

Selective Laser Melting (SLM) is a laser powder-bed-fusion (L-PDF) based additive manufacturing (AM) method, which uses the laser beam to melt the selected areas of the metal powder bed. By laying down multiple layers of metal powders and melt the selected areas of each layer, it will form an additive solid object [3]. This process is shown in Figure 1.1. There are already many metal 3D printer companies on the market, such as Concept Laser, Arcam, Xact Metal etc. The printed objects can range from complex industry parts to very simple cylinder samples for lab research purpose. In order to perform research on developing new AM materials using SLM method, the preparation of metal powders is necessary. People usually use gas atomization method to make spherical alloy powders in industry. However, it is too expensive and time consuming for lab new powder material development. Although we have established a powder making rig system in our lab, the quantity of the metal powder making rig can make is very limited and it is very hard to fill the powder chamber of the commercial machines. Even for the Concept-Laser Mlab cusing-R system (Lichtenfels, Germany) which is the smallest commercial SLM 3D printer, it also needs about 5 kg of powders in order to let the machine work properly. As a result, one of the main requirements of the customized 3D printer design is that it must be able to handle small quantity of mental powders which can be as few as just tens of grams. For lab research purpose, only a very small sample is needed to test the properties of a new material and the processing parameters, therefore not many metal powders are needed. Besides, the commercial 3D printers are designed to build functional parts with complex geometry. For research purpose, typically only a small block is needed for material testing in the lab environment. The hardware control systems and software functions can be much simplified for the lab 3D printers. In order to optimize the laser processing parameters for new materials, the freedom of changing all the SLM parameters are required,

such as layer thickness, laser power, scan speed, hatch spacing etc. However, to change the laser parameters for different new materials on the commercial 3D printers are very difficult to achieve since all the process parameters are set by the machine manufacturer and they are not visible to customers. Based on all the above situations and specific needs, a customized 3D printer is needed in the lab to achieve our research purpose.

2.2. Hardware design

2.2.1 The specification and capabilities of purchased components

Several components are purchased from the market in order to finish the design of the customized 3D printer. The mainly purchased components include the laser generator, scan head, F-theta lens, ScanMaster control board and step motors as shown in Figure 2.1

The laser generator is IPG YLR-200-AC-Y11 model which is a diode-pumped ytterbium fiber laser with the maximum output power of 200W operating at the wavelength of 1070 nm. All YLR series lasers are classified as high-power Class 4 laser instrument, so appropriate and approved laser safety eye wear must always be worn while the laser is operational [25]. The output power of the laser is controlled by the voltage of an external DC power supply and the Continues mode is used for laser scanning. An IPG D25 Collimator is used in order to transfer the laser into parallel light before entering the scan head.

The scan head is ProSeries II Scan Head from General Scanning Solutions. It provides the capability of deflecting optical beam in a XY plane. The synchronized actions of two galvanometer servo-controlled mirrors direct the laser beam to specific locations on a target in both the X and Y directions [26]. There is a servo driver for each axis and a 25-Pin D-sub XY2-100 communication control connector is connected to the ScanMaster control board. The motion of the mirrors is controlled by the pattern drawn in ScanMaster Designer software and the mirrors are coated with an yttrium aluminum garnet coating in order to reflect the light efficiently and prevent overheating the mirror.

The F-theta lens is purchased from Jenoptik with the focal length of 347mm. The F-theta lens can keep focus distance the same within the scan field and can focus the laser from about Ø12 mm to around 50 μm which the power density is significantly increased in order to melt the metal powders. The lens is mounted on the scan head through M85x1-6g thread.

The ScanMaster Control board is the main control board for the 3D printer. It communicates with the laser generator and the scan head. It comes with the ScanMaster Designer software which can draw different 2D graphs and 3D graphs and transfer to digital signals to control the scan head servo motors. The board is controlled by a laptop through Ethernet cable.

The step motors are for controlling the dose chamber platform and build chamber platform to go up and downs, and to control the wiper blade to go back and forth. The step motors are bought from Haydonkerk which are controlled by an Arduino step motor controller that was purchased from Amazon.

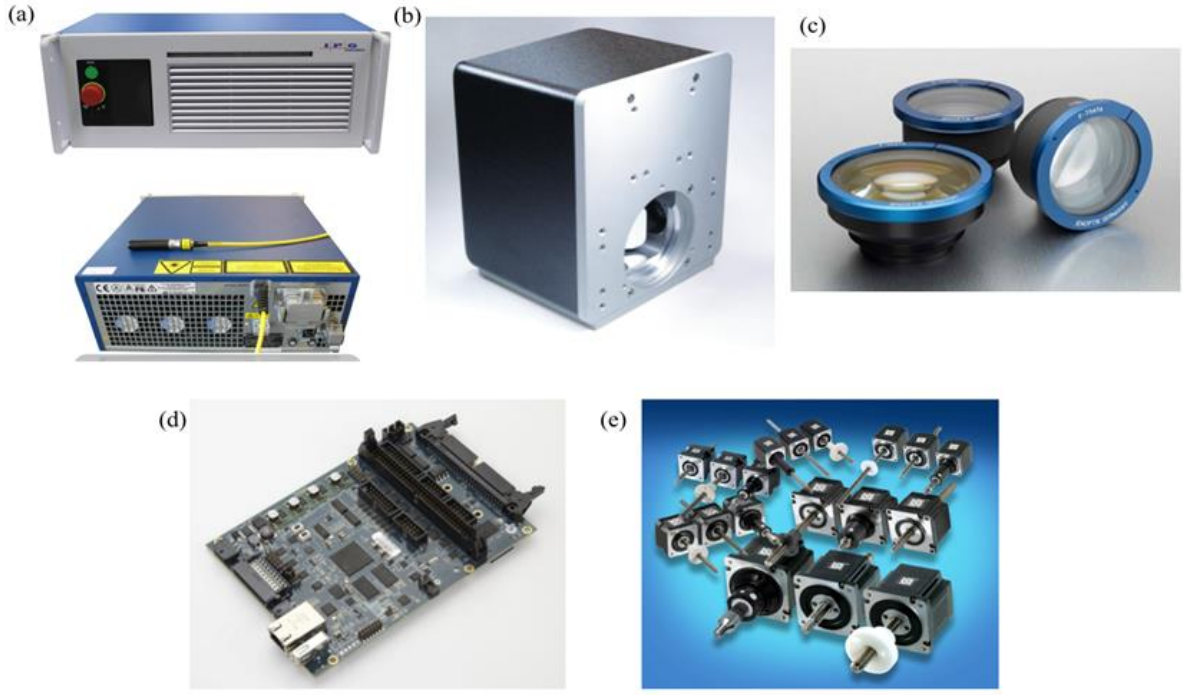

Figure 2.1. The purchased components (a) IPG 200W laser generator (b) ProSeries II scan head (c) F-theta lens (d) ScanMaster control board (e) Haydonkerk step motors

2.2.2 The design of the powder-handling unit

Figure 2.2 shows the assembly of the powder-handling unit. For simplicity all connectors are not shown in the figure. The bill of material is shown in Table 2.1. The frame (item 1) of the powder-handling unit is assembled using T-slotted bars and L-shape connectors (not shown) which were purchased from McMaster-carr. The dimensions were determined based on the size of the processing chamber. The first level plate (item 2) and the second level plate were cut to shape using 1/4" thick aluminum plates and the holes were drilled according to the components attached to the plates. Item 3 and item 14 are dose platform and build platform and they are attached to the screws that connecting the step motors (not shown) which are mounted at the back side of the first level plate. A round of felt material is attached to the platforms to form a seal between the powder chamber (item 4) wall and to make sure the platforms will not be stuck because of the metal powders which were trapped between the platform and the chamber wall. The powder chamber (item 4) was machined from a 8"x4"x2" solid aluminum block using CNC mill at LSU machine shop. The dose powder chamber is designed 25% larger than the build chamber to provide enough powder feeding. The part height is limited by the height of the processing chamber and the highest part can be built from this design is about 1 inch. Item 7 and item 13 were purchased from McMaster-carr and they are for the wiper blade to slide across the table to feed powders onto the build platform. The extra powder will fall through the hole on the powder chamber, and then be collected by the waste powder container (item 15). The wasted powder can be reused for several times after sieving. Two T-slotted bars (item 6) will hold the wiper blade rails at the same height and the height need to be adjusted to let the blade about 25 μm above the power chamber top surface. This can be done by inserting a piece of paper under the blade and remove it after installation. Item 9 is an adaptor piece which connects the rail and the belt. It is cut to shape using an aluminum L angle bar. The belt assembly (item 10) with two pulleys were purchased from McMaster-

carr and they were attached to the side of the table frame through two L angle bars (item 12) on each side. One of the pulleys is connected to a step motor (item 11) which controls the travel distance of the wiper blade. During assembly, the parts should be assembled from bottom to top, the level and distance between the rails and T-slotted bars need to be checked to make sure proper movement of wiper and step motors.

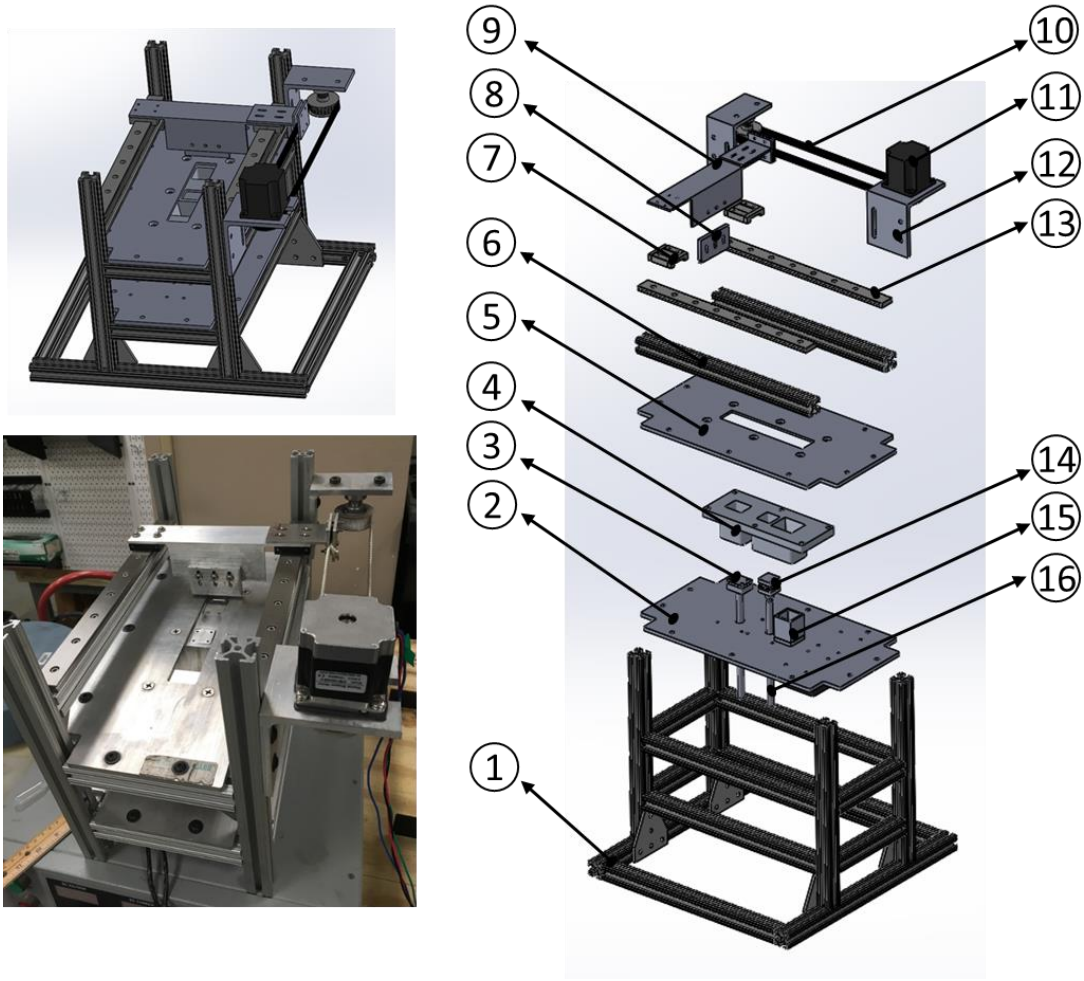

Figure 2.2. The exploded view of the powder-handling unit with an actual picture

Table 2.1. The bill of material for the powder-handling unit

Item No.	Name	Description	Commons
1	Table frame assembly	T-slotted bars, L shape connectors	The bars were cut to length at LSU machine shop
2	First level plate	1/4” thick aluminum plate	Cut to shape at LSU machine shop

Table cont’d

Item No.	Name	Description	Commons
3	Dose powder platform	1/2” thick aluminum block	Felt need to be attached around the block
4	Powder chamber	8”x4”x2” aluminum block	Machined at LSU machine shop using CNC mill
5	Second level platform	1/4” thick aluminum plate	Cut to shape at LSU machine shop
6	Rail holder	T-slotted bars	Cut to length at LSU machine shop
7	Rail slider		Purchased from McMaster-carr
8	Wiper blade holder	1/4” thick aluminum plate	Holds the rubber blade (not shown)
9	Wiper blade adaptor	2”x2” aluminum L angle bar	Machined at LSU machine shop
10	Timing belt assembly	Pulleys are included	Purchased from McMaster-carr
11	Step motor	Haydonkerk step motors	Controls the wiper travel distance
12	Pulley adaptor	4”x4” aluminum L angle bar	Attach to the side of the table frame (item 1)
13	Rail		Purchased from McMaster-carr
14	Build platform	1/2” thick aluminum block	Felt need to be attached around the block
15	Waste powder holder	Aluminum square tube	Welded at LSU machine shop
16	Step motor with screws	Haydonkerk step motors	Controls the travel distance of dose and build platforms

2.2.3 The design of processing chamber

Table 2.2. The bill of material for the processing chamber assembly

Item No.	Name	Description	Commons
1	powder-handling unit	Self-designed with multiple components	See section 2.2.2
2	Frame of processing chamber	16”x16”x20”	The bottom is blocked by a 14” diameter flange (not shown)
3	Door of processing chamber	16”x16”x0.5”	The doors are sealed by rubber oring around the frame.
4	Center ring	Mates with ISO LF Large-Flange	Purchased from MDC vacuum solutions
5	Scan head	ProSeries II Scan Head	Purchased from General Scanning Solutions
6	Collimator	Diameter of 25 mm	Comes with IPG laser

Table cont’d

Item No.	Name	Description	Commons
7	F-theta lens	Focal length 347 mm	Purchased from JENar
8	Scan head adaptor	1/4” thick aluminum plate	Attach the scan head and bottom flange
9	Flange	Custom welded	Machined at LSU machine shop
10	View Port	Zero profile viewport	Purchased from MDC vacuum solutions

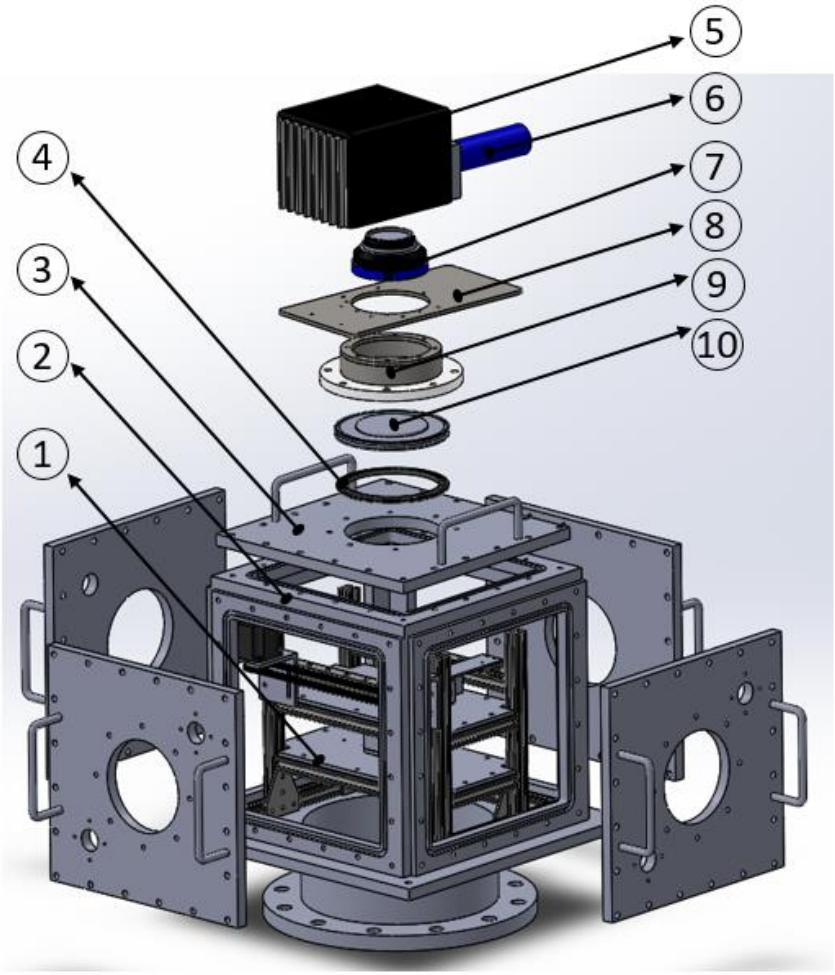

Figure 2.3. The exploded view of processing chamber assembly

The design of the processing chamber is based on the availability of an existing chamber donated to the team by LSU Chemistry Department. This chamber consists of five doors and a blocking flange at the bottom. All blocking flanges and view ports on the chamber doors are not shown in Figure 2.3. The ISO-KF standard for clamp connections (DIN 28404, ISO 1609) is the standard connection for vacuum pipes starting from the normal diameter

DN63. This ISO-KF standard clamp connections have been used for sealing the top of the vacuum chamber. Figure 2.3 shows the configuration of the sealing, which consists of a center ring (item 4), a view port (item 10) and a flange (item 9). Several bolts (not shown) are used to connect the above components to the top chamber wall and form a proper seal. The scan head assembly, which includes a collimator, a scan head and a F-theta lens, is mounted on top of the flange through an adaptor piece (item 8). For complicity, some other components are added to the processing chamber side walls, for instance, pressure gauges, gas inlet valves, vacuum valve etc. Some of these components are shown in Figure 2.4.

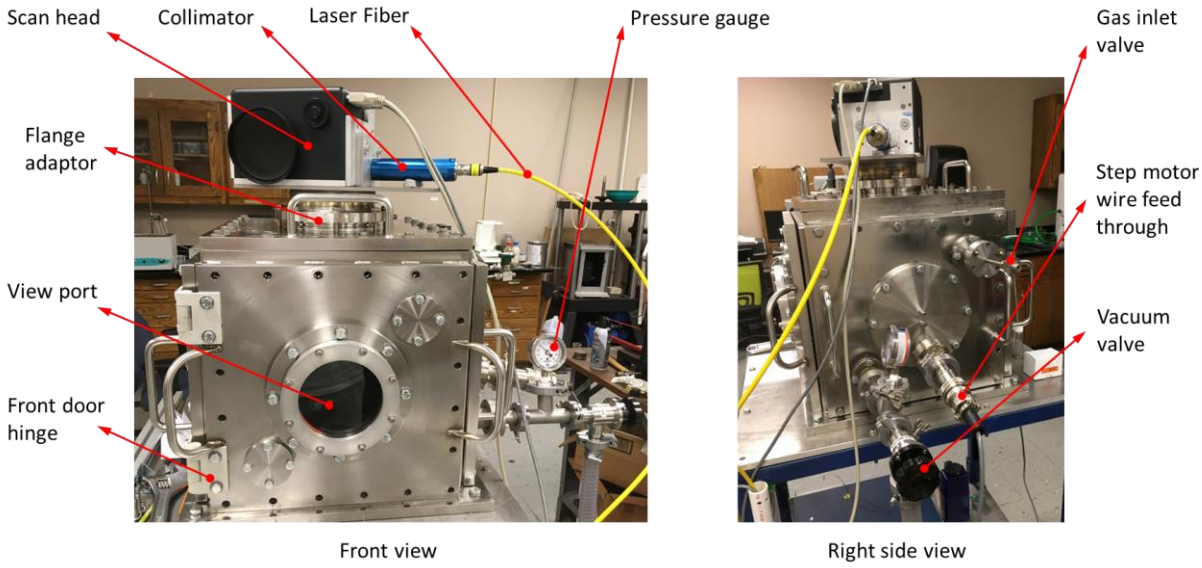

Figure 2.4. The front and right-side views of the real 3D printer established by the author

Before printing, the entire chamber needs to be cleaned thoroughly, especially when different powders are used from the previous printing. The wiper rails need to be lubricated using WD40 to ensure the wiper can operate smoothly during printing. The build platform needs to be adjusted to the same height as the powder chamber and the scan pattern needs to be adjusted on the desired position on the build platform using red guide laser. After that, the front door can be closed and tight sealed using bolts. The chamber will pull vacuum to under 150 Pascal and protective gas, such as Ar and N_2, will be filled back to the chamber through the gas inlet valve. During printing, the chamber should keep a little positive pressure to ensure

no air will enter the chamber. The printing condition can be viewed through the view port on the front door.

2.3. Electrical connections

Figure 2.5 shows the electrical diagram of the customized 3D printer. Two interlock switches are set up to make sure the chamber door is closed and the laser safety glasses are worn before starting the laser. Remote switch key and remote start button are used to turn the laser to standby mode remotely. The laser power is controlled by a DC power supply with analog input 1-10 VDC which corresponding to 10-100% of the laser power with maximum 200 W. On SMC board, the laser gate signal pin 8 of J18 connector can only provide 5V which is not enough to trigger the laser emission signal. Therefore, Pin 63 on auxiliary connector J13 and a transducer are used to provide a higher voltage (12 V). The scan head is connected with SMC board through a DB-25 cable in order to receive the scan pattern signals. SMC board communicates with a personal laptop through an Ethernet cable. A USB cable is used to connect the computer and the Arduino board and the three step motors inside the processing chamber are controlled by 12-gauge wires through a chamber feed through connector. A 24 VDC power unit provides power to scan head, SMC board and Arduino board.

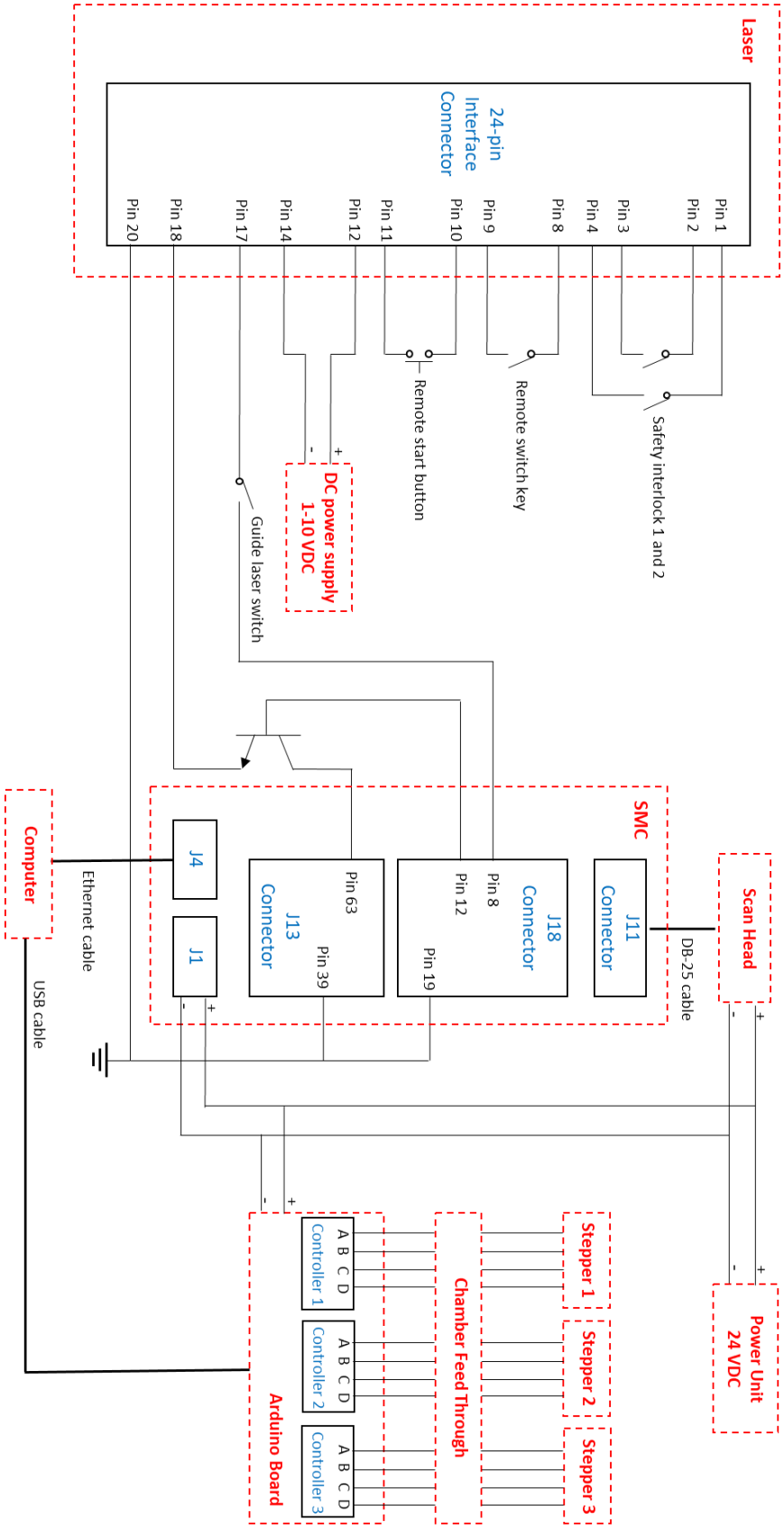

Figure 2.5. The electrical diagrams of the customized 3D printer

2.4. Software applications and codes

2.4.1 The software for step motor control and G-code

The step motors are controlled by an open source software called Universal Gcode Sender (version 1.0.9) which is downloaded from https://github.com/winder/Universal-G-Code-Sender/releases. Its corresponding firmware called “GRBL” need to be installed to the Arduino Step Motor Controller board in order to let the software work properly. G-code is widely used in the computer-aided manufacturing field, such as CNC lathes and CNC mills. It can control varies motions using code which starts with G and followed by different numbers. However, for our application, only linear motion at constant speed is needed. As a result, our step motor codes are start with G61 and G01 which corresponding to Constant speed mode and linear motion. The feeding rate is specified by a code like F50 which means move 50 mm per minute. Then the moving distance for build platform and dose powder platform should be set respectively. “+” means go up and “–” means go down. Z is set up for wiper blade and “+” means go forward and “–” means back ward. The code is grouped into two function keys “C2” and “C3” in the software, the function key “C2” is to let the build platform go down 0.05 mm and raise the dose powder platform 0.15 mm, “C3” is to let the wiper blade go forward and back one time in order to lay down a new layer of powders. Figure 2.6 is a screen shot of the software which shows the G-code for achieve the functions mentioned above. In the Machine Control mode, we can manually control each axis to adjust the positions and it is very useful for setting up the machine before each printing. In the machine status field, the position of each axis can be tracked. A standard USB cable is used to send the commands from the computer to the step motor control board.

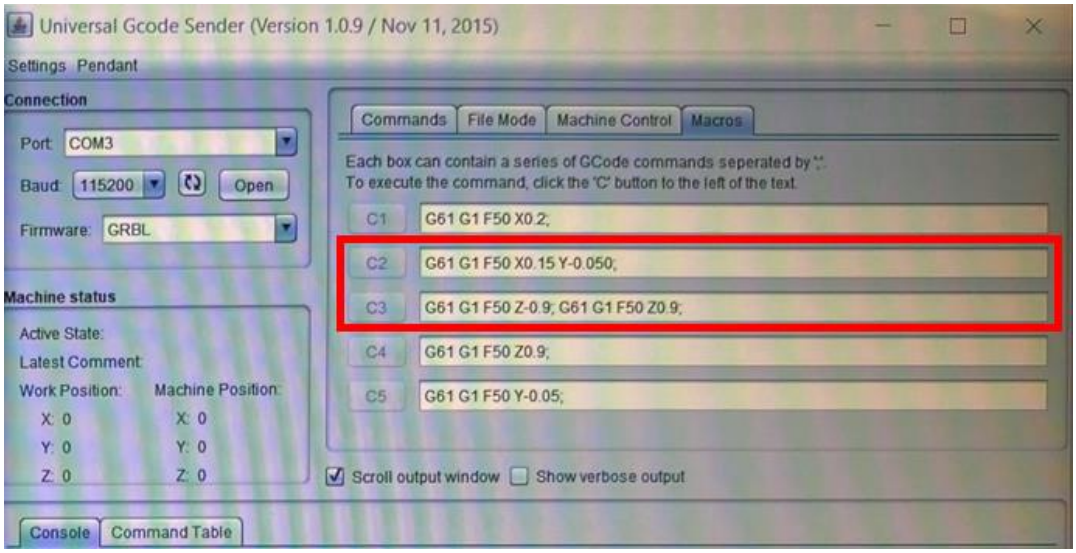

Figure 2.6. The Universal G-code Sender software interface

2.4.2 The software application of ScanMaster Designer and Automation

ScanMaster Designer is the software that comes with the ScanMaster control board, which can draw the desired scan patterns with different scan parameters. Figure 2.7 is the interface of this software and it shows an example 2D drawing which includes 16 small square blocks that corresponding to 16 different scan speeds and this pattern can print out 16 small blocks for material characterization. By doing so, multiple parameters can be tested with one print. Not only the 2D drawings, this software can also handle more complicated 3D drawings. It can slice the drawing into multiple layers and each layer is scanned sequentially to form complicated 3D geometry. The green triangle is the “Strat” control button which will enable the scan head to scan the pattern and the laser will turn on at the same time. The “Trace” function will let the scan head to fast trace the scan pattern using the red guide laser, which can be used for checking the pattern position on the build platform before each printing. The laser scan speed and laser on/off timing parameters can be adjusted under “Laser Properties”. All the above functions are marked with the red boxes in Figure 2.7.

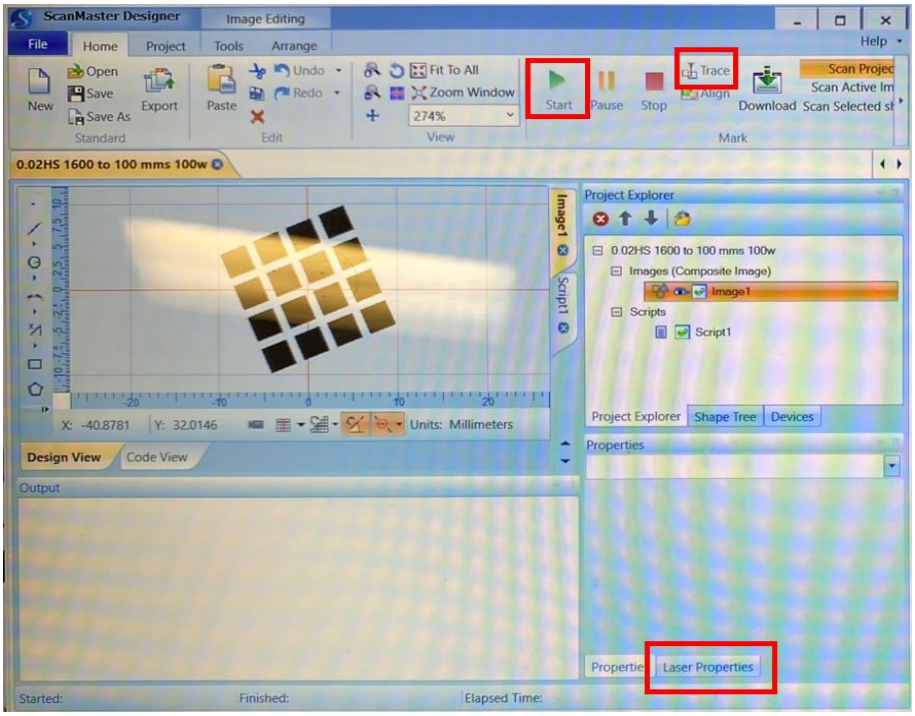

Figure 2.7. ScanMaster Designer software interface

The automation is achieved using an open source screen recording software called "tinytask145". During printing, the ScanMaster Designer software and the step motor control software are placed side by side on the computer screen. After setting up the scan pattern, the screen recording software need to be started. Then manually press "C2" and "C3" function sequentially to make the build platform goes down and dose powder platform goes up, after that the wiper blade will lay down a new layer of powders on the build platform. The screen recording software will record these actions and repeat it for multiple times. The repeating time equals the total layer number.

2.5. Thermal lensing and solutions

The first design of the processing chamber includes a gate valve (the item in the red box on Figure 2.8 (a)) which connects the scan head to the chamber top wall. The system was operating with no issues at beginning. However, after a few times of printing, the laser started to lose power after it turned on for a few seconds because we noticed that the metal powder cannot be totally melted. A laser beam checker (Figure 2.8 (d)) was purchased from Ophir-

Spiricon Products in order to investigate this problem. The laser beam checker can split the laser beam into two parts: a very small portion of laser beam is directed to a Charge-coupled Device (CCD) camera which is to check the size of the laser spot; the rest of the laser is defocused and enters into a power meter in order to check the power of the beam. After running a few tests, an abnormal phenomenon was found as shown in Figure 2.8 (b) and Figure 2.8 (c). The laser spot was very small at about 60 μm when laser just started (Figure 2.8 (b)), however, after a few seconds, the laser spot size can go up to 600 μm (Figure 2.8 (c)) and shows a ring-shaped geometry. After communicating with the specialist from the beam checker company, we find out this phenomenon is called “Thermal Lensing”.

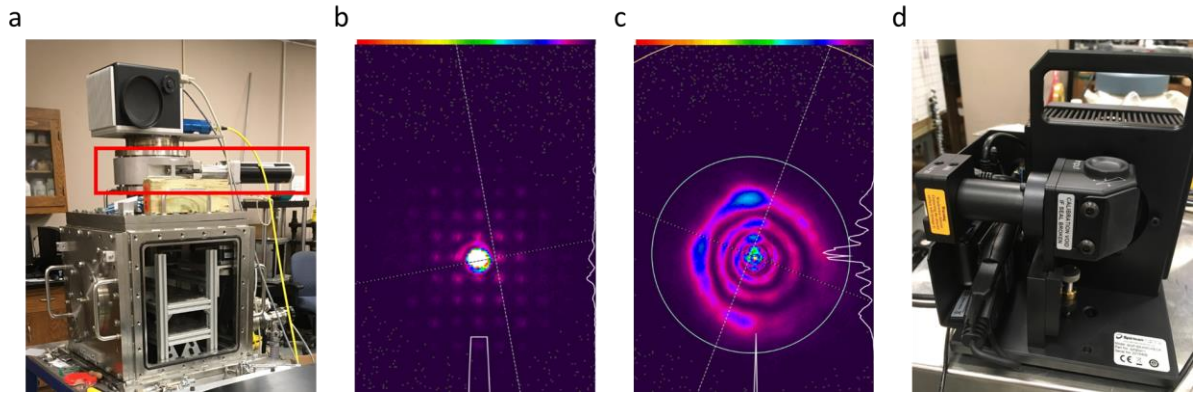

Figure 2.8. (a) Old design of outside chamber with gate valve (b) the laser spot shape when laser just on (c) the laser spot shape after laser is on for about 10 seconds (d) Beam checker from Ophir-Spiricon Products

After disassembly all the components on the laser path, finally I find out there are a lot of fine metal powders attached on the scan head mirrors. As a result, the reflectivity of the mirror decreased and some of the laser power is absorbed by the scan head mirrors which causes the coating on the mirror to deflect, and therefore the laser spot will have the shape in Figure 2.8 (c). It turned out that during printing, the metal powder dust can enter the scan head chamber through the fine screw which is used to attach the F-theta lens. Therefore, I replaced the gate valve with a view port which consist of a 2 mm thick 7056 glass and totally separated the scan head outside of the 3D printer processing chamber. The new design is already

introduced in section 2.2.3. It simplifies the operation procedure without close and open the gate valve during printing. However, this view port will decrease the laser power by about 10% due to the transmission efficiency. The beam checker test result matches the optical transmission curve shown in Figure 2.9 as point A which corresponding to the laser wavelength of 1070 nm.

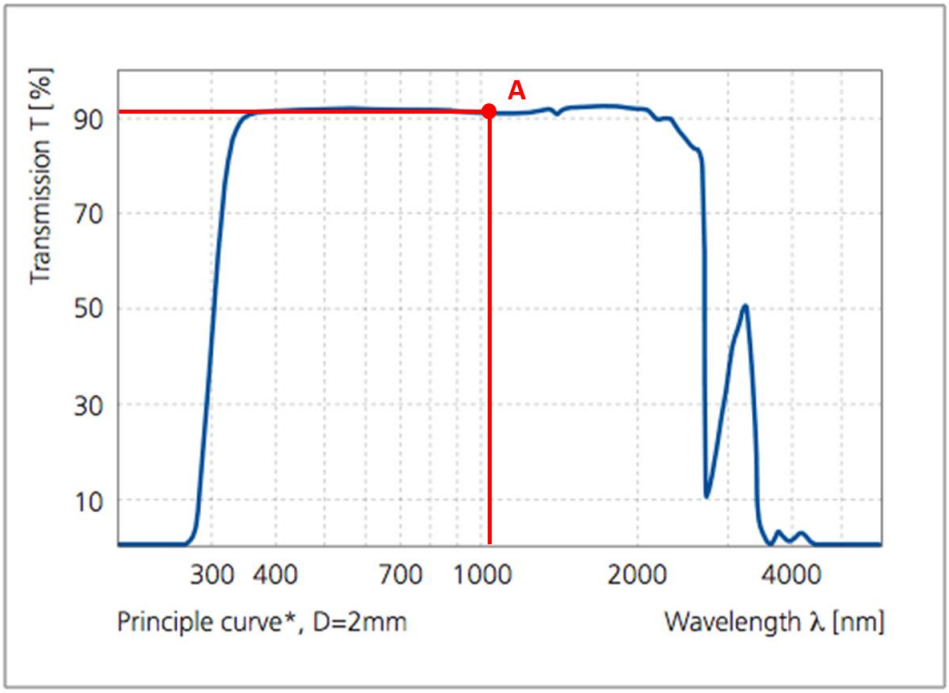

Figure 2.9. Typical optical transmission curve for 2 mm thick glass [27]

2.6. Experiments performed using the custom designed 3D printer

During the process of developing this customized 3D printer, many laser processing related research projects have been conducted by many researchers in Louisiana which involve different areas. This section will briefly list some of the research projects that mainly conducted by other researchers to illustrate the capability of this customized 3D printer. Chapter 3 and Chapter 4 will mainly focus on the author's own researches.

2.6.1 Laser surface engineering

Figure 2.10 (a) shows the schematic drawing of the machine setup which was used for laser surface engineering studies. Continuous laser mode was used, and the scan strategy is shown in Figure 2.10 (b).

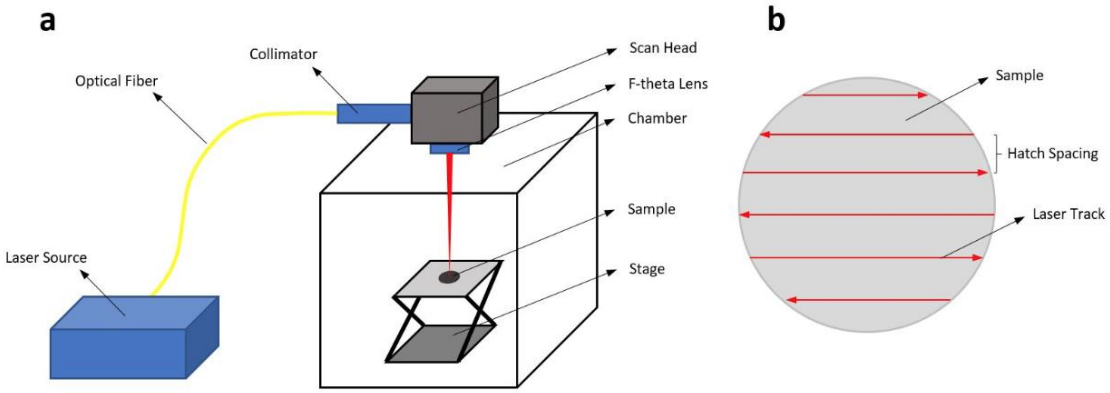

Figure 2.10. (a) Schematic drawing of the custom laser system used for surface laser processing (b) laser pattern used for scanning the surface of the samples [28]

Dr. Ali Hemmasian Ettefagh performed laser surface treatment on oxide dispersion strengthened (ODS) ferritic alloy sample surfaces which are prepared using Spark Plasma Sintering (SPS). The chemical composition of the sample is Fe-14Cr-2W-0.3Ti-xY_2O_3 (wt.%) and the x values were chosen with the amount of 0, 0.3, 0.6 and 0.9 to study the effect of the amount of oxide particles to the final results [29]. The laser surface treatment was conducted using the custom AM machine and different laser parameters were chosen with different laser powers, scan speeds and hatching spaces to achieve different power densities. In order to understand the mechanism of the reaction, surface characterizations including X-ray diffraction, Raman spectroscopy, and microhardness were performed. The corrosion performance was measured by a CHI 604C electrochemical workstation in 3.5 wt% NaCl water solution[28]. After testing, it's found that the best sample was scanned using laser power 175 W, scan speed 200mm/s and hatching space 0.025 mm with 0.3 Y_2O_3 (wt.%) content [28,29]. The corrosion resistance of the laser treated sample was 5 times higher than the bare sample in

a simulated marine condition and it was due to the formation of a protective coating on the surface.

Laser treatment of titanium surface studies were performed by Dr. Congyuan Zeng et al. In collaboration with researchers in Center for Advanced Microstructures and Devices (CAMD), in-situ synchrotron X-ray diffraction testing revealed the high temperature reaction steps between pure titanium and ambient air under transient laser processing conditions. The cross section of these samples revealed the oxygen and nitrogen depth which lead to the estimation of high-temperature diffusion coefficients into the titanium substrate [30]. Some single-track scan was performed using the custom AM machine.

Besides, the laser nitriding of titanium surfaces was also studied for biomedical applications. The pure titanium samples were scanned with different scan speeds and under different N_2 concentrations using the same setup as shown in Figure 2.10 (a). For example, one sample was processed using a laser power of 175W and a spot size of 207 μm. Three different laser scanning speeds, 100, 400, and 1600 mm/s, were selected under a pure N_2 environment and the samples were denoted as Ti-N100, Ti-N400 and Ti-N1600, respectively. To investigate the effects of N_2 concentration on the formation of titanium nitride layers (with laser power 175 W, scanning speed 400 mm/s), five N_2 concentrations were chosen as 100, 75, 50, 20 and 0 vol%, with the balance as Ar. The samples are named as, Ti-N75%, Ti-N50%, Ti-N20% and Ti-N0%, respectively [31]. The bio-compatibility evaluation was conducted using MLO-Y4 cells and corrosion test was done using simulated body fluid (SBF). The images for all the samples and cell test are shown in Figure 2.11. This test was performed at the same time as the experiment that included in Chapter 3. A conclusion is made that the dense and thick titanium nitride dendritic layer can improve bio-compatibility and corrosion resistance within SBF.

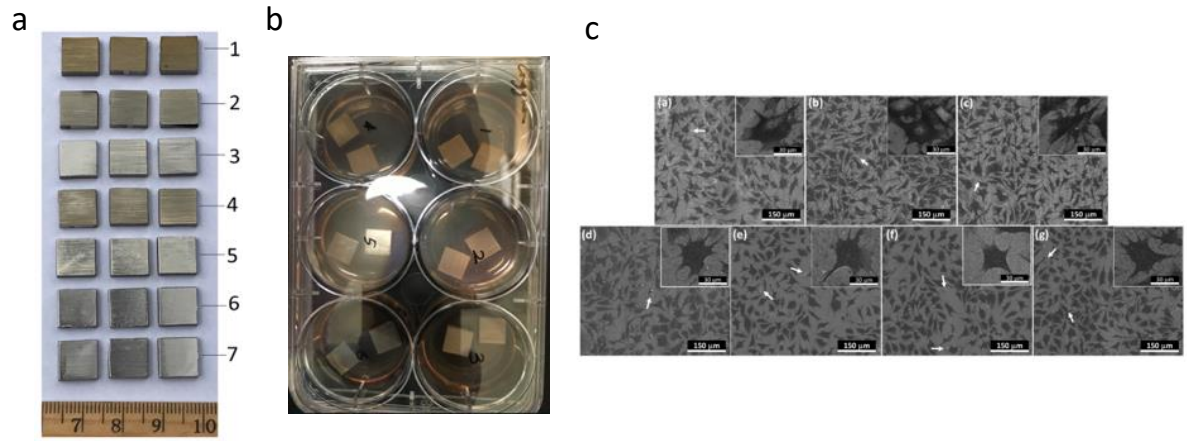

Figure 2.11. (a) Image of the as-processed titanium samples. (b) cell test performed using 6-well plate. (c) the cell morphology of each condition observed under SEM [31]

2.6.2 Printing parameter development on new metal powders

For some new powders that made in a lab environment, the optimum printing parameters are usually unknown. Due to the small quantity of powders, the customized 3D printer is ideal for developing the printing parameters for these kinds of alloys. Figure 2.12 shows some of the tested samples with different laser parameters using different materials. The substrate needs to use similar materials as the powder material in order to achieve better attachment. Each little block corresponding to a different scan speed which ranges from 100 mm/s to 1600 mm/s. The blocks will be labeled and cut off from the substrate using wire EDM for some material characterization using SEM to investigate their printing quality.

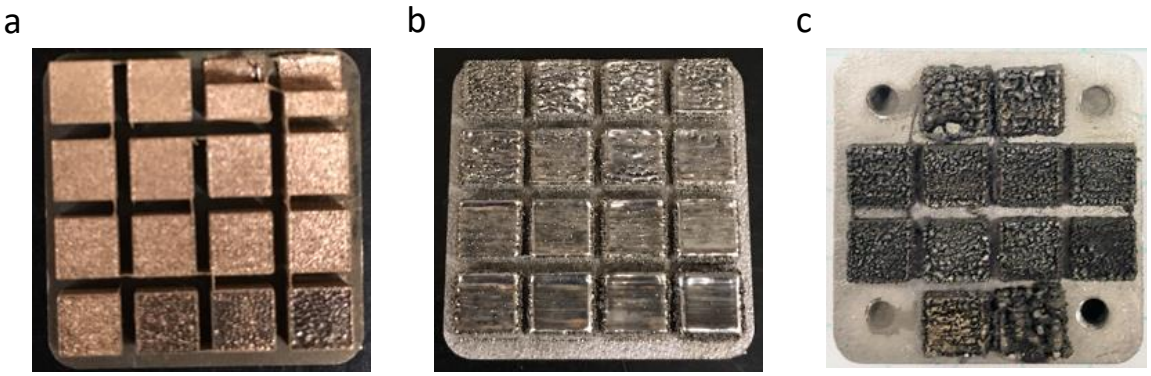

Figure 2.12. (a) commercial Cu-10Sn alloy powder (b) experimental Inconel 939 powder purchased from LPW (c) aluminum alloy powder made by ball milling (Tulane University)

From Figure 2.12 we can find out that usually commercial powders show the best result due to lots of researches have already been done to optimize the processing parameters for SLM specifically. The powders which are still under investigation, some of the samples can achieve very low porosity using low scan speed. However, these samples usually show significant distortions. The self-made alloy powders using ball milling usually show the worst result, such as the aluminum powder as shown in Figure 2.12 (c). One reason is because usually the aluminum powder surface is covered with a thin oxidized layer which has very high melting point, so the laser is very hard to melt and combine the particles together; another reason is that the powder is not in spherical shape after ball milling which will affect the flowability of the powder. As a result, the layer thickness needs to be increased in order to lay down one layer of powder, otherwise the wiper blade will remove all the powders from the sample surface. From these tests, conclusions can be made that not only the printing parameters can affect the final quality of the print, but also the material itself also plays a very import role in SLM. The powder compositions need to be optimized specifically for SLM and some simulation study need to be performed before doing experimental tests. Some other functional materials were also tested by this customized 3D printer, such as magnetic powder materials and thermal electrical materials. Dr. Seetala from Grambling State University did some test using magnetic FePt and SmCo nano/micro particles after I performed laser heating on those powders. However, for FePt/Cu nano particles, the laser heat treatment even at temperature close to vaporization temperature did not show significant change in the coercivity. For $SmCo_5$ powder, the magnetization was increased when laser power was at 50 W [32].

2.7. Conclusion

After many tests were conducted using this customized 3D printer for varies applications, a conclusion can be made that this machine is very useful for 3D printing researches or laser related researches. This machine has the flexibilities to adjust different laser

parameters to achieve different conditions. Some SLM related printing can be conducted by using very small amount of metal powders which is a very efficient and economical path for future SLM related studies.

Chapter 3. Laser Surface Treatment of Ti-10Mo Alloy under Ar and N_2 Environment for Biomedical Application

3.1. Introduction

Previous studies demonstrate that β-type titanium alloys have enhanced properties for biomedical applications, such as lower elastic modulus, better corrosion resistance, and improved tissue response when compared with α-type and α+β-type titanium alloys [33–39]. As a result, titanium alloys with non-toxic β phase stabilizer elements such as Nb, Ta, Zr, Mo, and Sn were investigated for use in biomedical applications. Molybdenum is an essential microelement and β-stabilizer with a greater stabilizing ability compared to Nb or Ta [40]. A 10 wt.% concentration of Mo in Ti-Mo alloy results in a dominant retained Beta phase and more desirable mechanical properties for biomedical applications, such as medical implants [36,40].

For a medical implant to be successful, bone and tissue must be able to adhere to the implant and remain healthy. Cell protein adsorption, receptor-ligand binding, signal transduction, and cell attachment are significantly affected by implant surface morphologies and chemical compositions [8]. As a result, the surface morphology and chemical compositions of metallic medical implants strongly affect osseointegration, healing time, and tissue regeneration [9]. Therefore, properly engineered implant surfaces play a critical role in tissue health, adherence and ultimately the success of an implant. For example, to improve osseointegration, techniques such as sandblasting, plasma spraying, and acid etching have been used to increase the bone-to-implant contact and to promote osseointegration [9,41]. However,

This chapter was reprinted with permission from Hao Wen, Congyuan Zeng, Ali Hemmasian Ettefagh, S.M. Guo. "Laser surface treatment of Ti-10Mo alloy under Ar and N_2 environment for biomedical application", Journal of Laser Applications. Copyright 2019, Laser Institute of America.

these methods may cause contaminations by introducing impurities or other elements to the implant surface. Such contaminations may negatively alter the protein adsorption behavior of cells [42,43], result in improper attachment of bones to implant, and lead to implant failure. Alternatively, laser-based surface modification methods can be used to improve corrosion, abrasion resistance, and wettability for better implant success without the adverse side effects [44]. Laser beam irradiation has also been demonstrated to eliminate contamination with good reproducibility [9]. Laser beam with a small spot size and a proper scanning speed can deliver high levels of energy to the material surfaces, produce extremely high temperatures and cooling speeds ($>10^5$ K/s). Typically, the resulting laser molten tracks have unique microstructures with metastable phases that are impossible to achieve using conventional methods, such as casting and forging [45].

Many laser modifications of metal surfaces have been studied to improve base material biocompatibilities and corrosion resistance. Laser beam irradiation can alter the sample surface roughness and chemical compositions. Oliveira et al. demonstrated that laser modified Ti-15Mo alloy implants surface have a higher bone-to-implant-contact percentage compared to non-treated samples [9]. Datta et al., Dahotre et al. and Razavi et al. have all demonstrated that laser beam irradiation in a nitride environment can form TiN coating on Ti-6Al-4V alloy surface, which can improve the cell integration and electrochemical properties for Ti-6Al-4V alloy [45–47]. For Ti-Mo alloys, up to this point, biomedical related research has primarily focused on studying the effects of alterations of the concentration of Mo on mechanical and corrosion properties [33,48–50]. Therefore, the main purpose of this study is to evaluate how the corrosion resistance and cell integration properties of Ti-10Mo alloy would alter, undergoing laser beam irradiation based surface modifications in either a pure Ar or a N_2 environment.

3.2. Experiment

3.2.1 Fabrication of Ti-10Mo alloy samples

The Ti-10wt.%Mo samples are prepared using an arc melter with 99.9% Ti powders (75 μm average particle size) and 99.5% Mo powders (56 μm average particle size). The Ti and Mo powders were first premixed for one minute at room temperature (approx. 20 °C) in a SPEX SamplePrep Mixer/Mill. The mixed Ti-Mo powders were then pressed into small ingots before arc melted using Edmund Buhler GmbH MAM-1 Arc Melter (Germany) which equipped with a water-cooled hearth and non-consumable tungsten electrode in an Ar atmosphere. The ingots were flipped and re-melted 4 times to ensure chemical homogeneity [33]. Subsequently, the ingots were cut into ~1mm thick disks using a low-speed saw and polished to 600 grade using silicon carbide papers.

3.2.2 Laser treatment under Ar and N_2

Before laser treatment, the 1mm thick Ti-10Mo disks were ultrasonically cleaned using acetone, ethanol and deionized water for 5 minutes each sequentially. Then the disks were placed in a custom designed laser system, equipped with an ytterbium fiber laser with wavelength of 1070 nm and in continuous mode (IPG model: YLR-200-AC-Y11), a IPG D25 Collimator with diameter of 25 mm, a Cambridge Technology ProSeries II scan head which is controlled by ScanMaster software, and a Jenoptik F-theta lens with flange focus length of 445.8 mm and minimum spot size of 46 μm. The laser system setup is shown in Figure 3.1 (a), and the laser processing parameters are listed in Table 3.1.

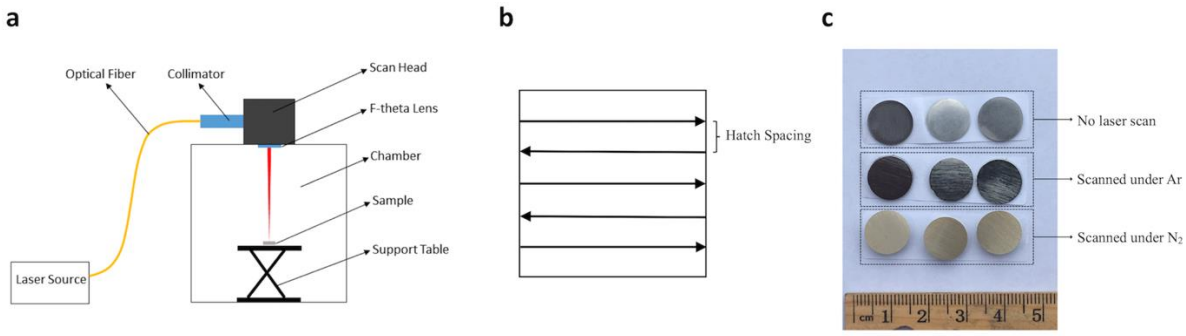

Figure 3.1. (a) Schematic diagram of laser system setup (b) illustration diagram of laser scan pattern (c) Sample surface appearance for different surface modifications

Table 3.1 Laser processing parameters

Group No.	Laser power P (W)	Spot diameter D (μm)	Scan speed v (mm/s)	Interaction time t=D/v (ms)	Laser fluence $E=Pt/(\pi D^2/4)$ (J/mm^2)	Hatch spacing(mm)	Atmosphere
1	N/A	N/A	N/A	N/A	N/A	N/A	N/A
2	75	104	100	1.04	9.18	0.05	Argon
3	75	104	100	1.04	9.18	0.05	Nitrogen

The disk surfaces were laser scanned in either pure (99.999%) Ar or pure (99.999%) N_2 at 1 atm. The scanning pattern is illustrated in Figure 3.1 (b) which covers the entire sample surface. The final sample appearances are shown in Figure 3.1 (c).

3.2.3 Material characterizations

The surface morphology and element distributions were observed under a Quanta™ 3D DualBeam™ FEG FIB-SEM scanning electron microscope (SEM) and energy-dispersive X-ray spectroscopy (EDXS). PANalytical X-ray diffraction (XRD) with Cu Kα radiation was used to analyze the phases of the sample surfaces. The surface roughness was measured by ContourGT-K 3D optical microscope. Five different areas from each sample were randomly selected for analysis, and the results were presented as mean ± standard deviation (SD). X-ray photoelectron spectroscopy (XPS) analysis was performed using a Scienta Omicron ESCA 2SR surface analysis system. The pressure of the analysis chamber was maintained at ~9.0 μPa during Ar^+ sputtering and the Ar^+ acceleration was 3.5 keV at a beam emission current of 5.0

μA. The accelerated Ar^+ can slowly remove the top surface of the samples, so that the element change in the depth direction can be analyzed. Data collection occurred between every 5-minute interval during the Ar^+ sputtering process.

3.2.4 Electrochemical measurements

To investigate the corrosion performance of Ti-Mo samples prepared under different laser process conditions, electrochemical measurements were carried out in a three-electrode system using a CH Instrument™ electrochemical workstation in simulated body fluid (SBF). SBF (1L, pH 7.40) was prepared by mixing the following ingredients: NaCl 7.996 g, NaHCO3 0.35 g, KCl 0.224 g, K2HPO4•3H2O 0.228 g, MgCl2•6H2O 0.305 g, 1 M HCl 40 ml, CaCl2 0.278 g, Na2SO4 0.071 g, (CH2OH)3CNH2 6.057 g [51]. The Ti-10Mo alloy samples were the working electrode in SBF (37 ± 0.5℃). A Pt wire was used as counter electrode and a saturated calomel electrode (SCE) was used as the reference electrode. Each Ti-Mo sample was encased in SampleKwick acrylic with a predefined exposed surface area. After immerging the sample into SBF for 15 minutes, potentiodynamic polarization was conducted in the potential range of -1 V to 2.5 V vs. SCE at a scan rate of 2 mV/s. Five samples were tested for each category of Ti-Mo samples. This section of experiment was conducted with the help of Ali Hemmasian Ettefagh from LSU.

3.2.5 Biocompatibility test

Biocompatibility for T-Mo alloy samples was tested with MLO-Y4 cells. The MLO-Y4 osteocyte-like cell line has been used by other researchers to mimic the osteocyte cell behaviors of forming woven bones [52]. The woven bone is formed from the osteoblasts that are enveloped by the mineralization front of calcifying matrix and become clustered as osteocytes in bone lacunae [53]. Woven bone plays a crucial role during the peri-implant bone early stage healing process. The formation of woven bone can bridge the gap between the host bone and the implant surface, providing secondary stabilization.

The laser treated and untreated Ti-Mo samples were ultrasonically cleaned sequentially in acetone, ethanol, and deionized water for 5 min each, followed by overnight UV exposure for sterilization. MLO-Y4 cells were seeded at a density of 2×10^4 cells/cm2 on the sample surface. Three disk shaped metal samples for each test group were placed into a single well of a standard 6-well plate and emerged in warm (37 °C) alpha minimum essential medium (α-MEM) supplemented with 5% fetal bovine serum, 5% calf serum, and 1% penicillin/streptomycin. The samples were then immediately placed in a 5% CO_2 balanced air incubator at 37°C for 24 hours. Next, 8 drops of NucBlue® Live reagent (Hoechst 33342) and propidium iodide were added to each well and incubated for thirty minutes. All cells were fixed with 3% glutaraldehyde and dehydrated using gradient ethanol concentrations (25%, 50%, 75%, 95%, and 100%) for viewing [45]. Cell morphology was examined using a Quanta™ 3D DualBeam™ FEG FIB-SEM in secondary electron mode at 5 kV. The live/dead cell images were captured under Zeiss SteREO Lumar fluorescent microscopy at 80x magnification. As NucBlue® Live reagent stains the nuclei of all cells, and propidium iodide only stains the nuclei of dead cell, cell viability was calculated as (Nt – Nd)/Nt, where Nt is the total cell numbers [NucBlue Stained]; and Nd is the dead cell numbers [propidium iodine stained].

For biocompatibility comparisons, the number of cells on the alloy samples was quantified using composite cell viability images from Zeiss SteREO Lumar fluorescent microscopy and ImageJ software (NIH, Bethesda, MD). Ten images were captured randomly on each sample surface. For each type of samples, three samples with thirty total images were used for cell density and viability statistical analysis. Data are analyzed by one-way Analysis of Variance (ANOVA) method and are presented as mean ± SD. P-value is used to quantify the statistical significance. $p<0.05$ is considered statistically significant.

3.3. Results and discussions

3.3.1 Surface morphology and material characterization

Table 3.2. Surface roughness values (mean ± SD)

Sample name	Sa (nm)	Sq (nm)	Sp (μm)	Sv (μm)	Sz (μm)
Untreated sample	320 ± 2.8	405 ± 2.1	3.12 ± 0.71	-2.98 ± 0.44	6.10 ± 0.84
Laser-Ar sample	359 ± 56.8	456 ± 79.7	1.95 ± 0.67	-2.40 ± 0.55	4.35 ± 0.89
Laser-N_2 sample	2645 ± 37.5	3495 ± 67.2	12.91 ± 0.23	-17.74 ± 0.19	30.64 ± 0.038

The surface roughness values for three types of Ti-Mo samples are listed in Table 3.2, where Sa is the arithmetic mean height; Sq is the root mean squared height; Sp is the maximum peak height; Sv is the maximum valley depth; and Sz = Sp + Sv which is the maximum height. There are no significant differences between the non-laser scanned samples (untreated) and the laser scanned samples in Ar environment (laser-Ar samples). However, the samples treated by laser under the N_2 environment (laser-N_2 samples) have significantly higher surface roughness values, compared with the other two sample types. Scratch lines caused by polishing can be observed on the untreated samples (Figure 3.2 (a)). For the laser-Ar samples, the laser scan pattern is clearly visible and indicated by vertical lines Figure 3.2 (b), that mirrors the laser scanning pattern. Although the scanning patterns are also observed on the N_2 samples (Figure 3.2 (c)), the molten track surfaces are significantly rough with corrugated features.

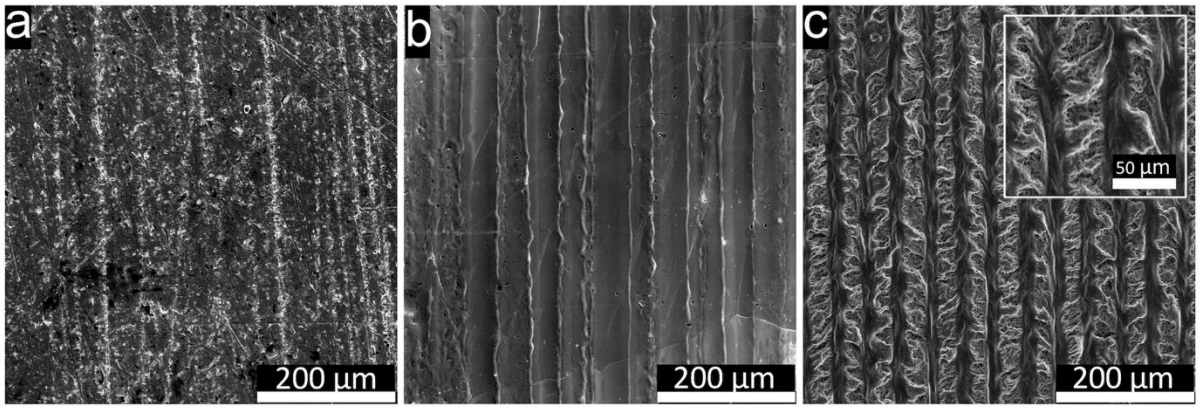

Figure 3.2. SEM image of (a) untreated sample surface (b) laser-Ar sample surface (c) laser-N_2 sample surface

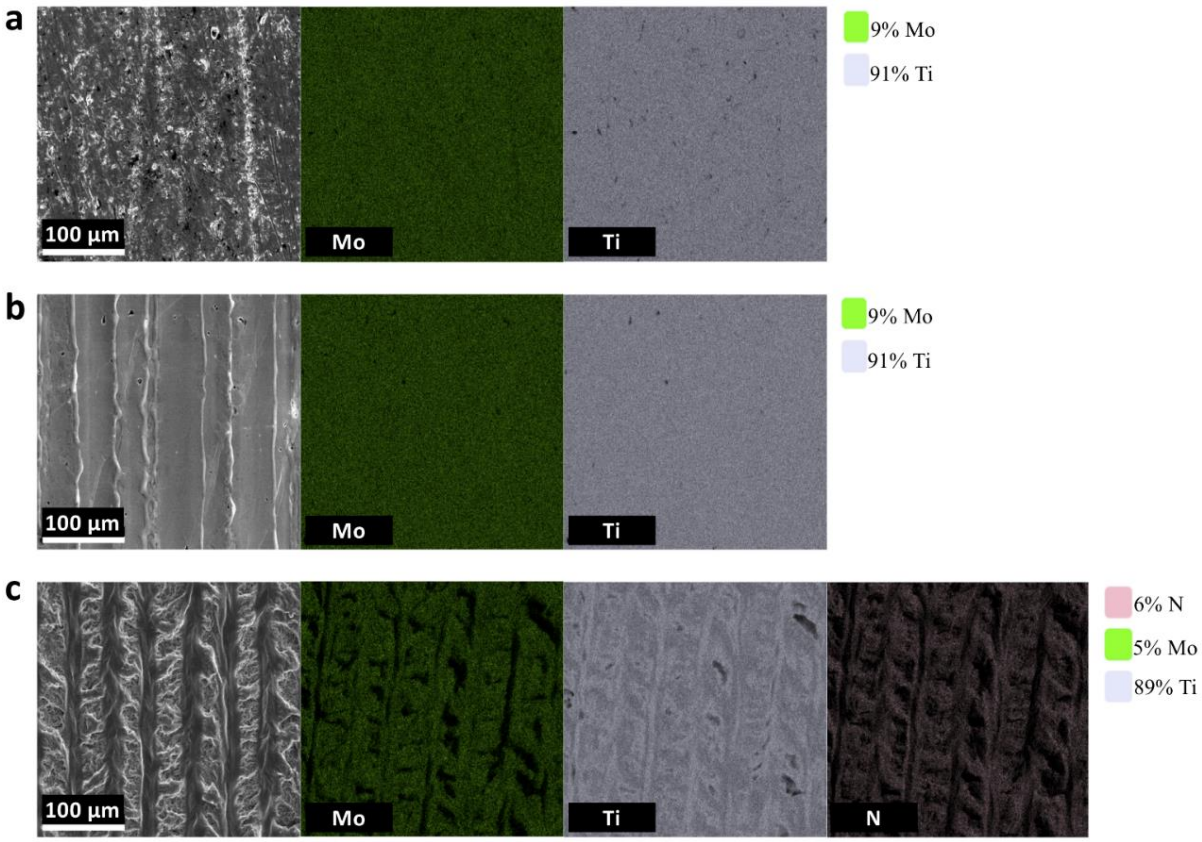

Figure 3.3. EDXS mapping image of (a) untreated sample surface (b) laser-Ar sample surface (c) laser-N_2 sample surface

The EDXS mapping image shows a homogeneous distribution of Ti and Mo elements on the untreated and laser-Ar sample surfaces. Laser scanning in the Ar environment is found not to affect the elemental compositions (Figure 3.3 (b)), indicating no contamination during the laser-Ar surface treatment process. The weight percentage of Ti is found to be 91%, and Mo to be 9%, which is close to the ideal weight ratio of Ti-10wt.%Mo (Figure 3.3 (a) and Figure 3.3 (b)). Even though the reaction time of Ti-10Mo with nitrogen under laser irradiation is short, a thin layer of nitrides with corrugated shape is formed on the sample surface, which is attributed to the chemical reactions induced by laser beam irradiation. As shown in Figure 3.4, the laser-N_2 sample cross section can be divided into three regions: the laser melted region, the heat affected zone, and the bulk Ti-10Mo base alloy. The microstructure of the laser melted zone consists of a thin continuous layer of nitrides with the growth of dendrites embedded in the melted zone, under which some randomly oriented and needle-like shaped dendrites are

produced. A similar structure is observed by Razavi et al. and Al-Mana et al. [46,54]. On average, 6% of N, 5% of Mo and 89% of Ti were detected by EDXS mapping at the laser-N_2 sample surface as shown in Fig 3.3 (c).

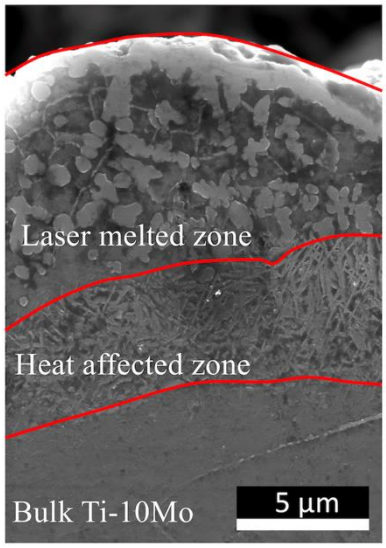

Figure 3.4. The cross section of laser-N_2 sample

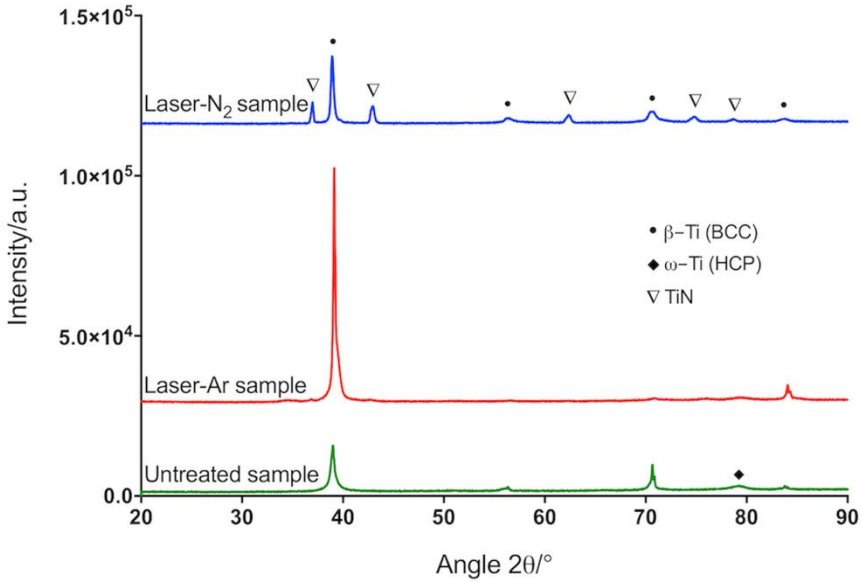

Figure 3.5. XRD results for Ti-10Mo with different surface modifications

The XRD results (Figure 3.5) indicates that the untreated sample is predominately β-Ti, with small trace of ω-Ti, due to the fast cooling rate during the arc melting process for making those small sized testing samples. The metastable ω particles are the nucleation sites

for α precipitates [55]. To investigate the mass fraction of different phases near the surface, XRD diffraction is commonly used to make such estimations. Laser scanning based surface modification enables an even faster cooling rate than that found in the arc-melting process, which is favorable to maintain the beta phase when cooled down. The proportion of ω-Ti in the laser scanned layer is decreased and more metastable β-Ti is retained, which can be observed by the disappearance of ω-Ti peak at 79 degree and the increased magnitude of β-Ti peak at 39 degrees. Using Figure 3.5 data, Eq.1 calculation confirms the increase of β-Ti phase on the surface of the samples processed with laser under the Ar environment, in comparison to the original arc-melted samples.

$$w_x = \frac{\frac{I_x}{K_x}}{I_1/_{K_1} + I_2/_{K_2} + \cdots + I_x/_{K_x}} \qquad (1)$$

where *w* is mass fraction, *I* is the diffraction intensity of the strongest peak of phase x and *K* is the Reference Intensity Ratio (RIR) value which can be obtained from standard powder diffraction file (PDF) cards. The RIR values for ω-Ti and β-Ti are 6.45 and 9.60. For laser-N_2 samples, TiN peaks are observed in the XRD result, confirming the formed nitrides which is shown in Figure 3.4 with white contrast.

3.3.2 The corrosion performance

Figure 3.6 shows the potentiodynamic polarization curves of Ti-10Mo alloy samples, which are treated under three different conditions. The corrosion potentials of both laser-Ar and laser-N_2 samples are nobler than the untreated samples, with generally smaller current densities. The untreated samples formed a passive layer at approximately 0.05 V vs. SCE and experienced no pitting up to 2.5 V vs. SCE. The passive layer is a thin oxide film that forms on the sample surface which can prevent the oxidation from proceeding. The formation of the passive layer for the laser-processed samples was slower, compared to the untreated samples.

The current density of the laser-processed samples was about the same as the untreated samples at ~1.6 V vs. SCE. The current density of laser-N_2 sample was fairly constant from ~ -0.1 V vs. SCE to 0.1 V vs. SCE. After that, the current density generally increased with the potential. For anodic polarization, the current density for the laser-N_2 samples has lower values than those of untreated and laser-Ar samples. Under anodic polarization, the TiN layer can be oxidized to a Ti-N-O compound [56]. The oxidation process contributes to the alterations in current density. Early studies have demonstrated that the oxynitride layer can slow down chloride ion ingress into the base material thus improve corrosion behavior [57,58].

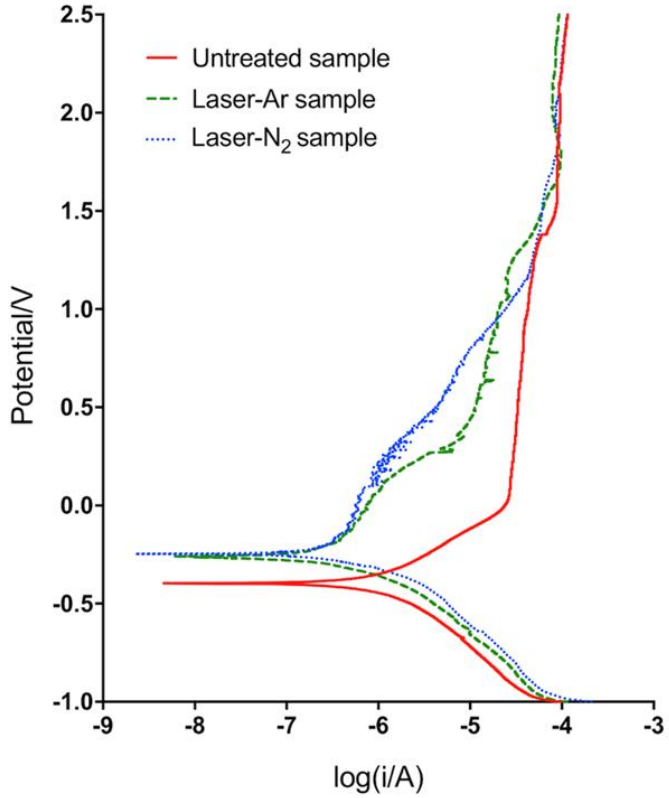

Figure 3.6. Potentiodynamic polarization curves of Ti-10Mo alloy for different surface modifications

Although the rough TiN surface has a greater surface area compared to the other two types of samples, it has the lowest corrosion current density and the highest corrosion potential. Additionally, a barrier is formed on the laser-N_2 sample surface between the SBF and the substrate material [56], indicated by the near consistent current density between ~ -0.1 V vs.

SCE to 0.1 V vs. SCE. At a potential higher than 0.1 V, the steady increase of current density is due to the corrosion of the TiN layer. However, the corrosion rate for the TiN layer is much slower than that of the base alloy Ti-Mo. Many studies have demonstrated that TiN can improve the base material corrosion resistance under various conditions [56,59–62].

Figure 3.7 (a) shows the element depth profile for laser-N_2 sample before the potentiodynamic polarization test. In Figure 3.7 (a), before the Ar^+ sputtering, the oxygen concentration was initially high and within the first 5 minutes Ar^+ sputtering, the oxygen concentration decreased rapidly and the Ti and N atom ratio reached close to 1:1, which confirms the formation of TiN on the laser-N_2 sample surface. The formation of MoN requires a high degree of ionization energy and/or a very high partial pressure of nitrogen [63], so the main component of the top surface of the Ti-Mo alloy under laser melting in the N_2 environment is TiN. As a result, the XPS result in Figure 3.7 (a) only shows a very small amount of Mo and the EDXS mapping result (Figure 3.3 (c)) shows 5% Mo.

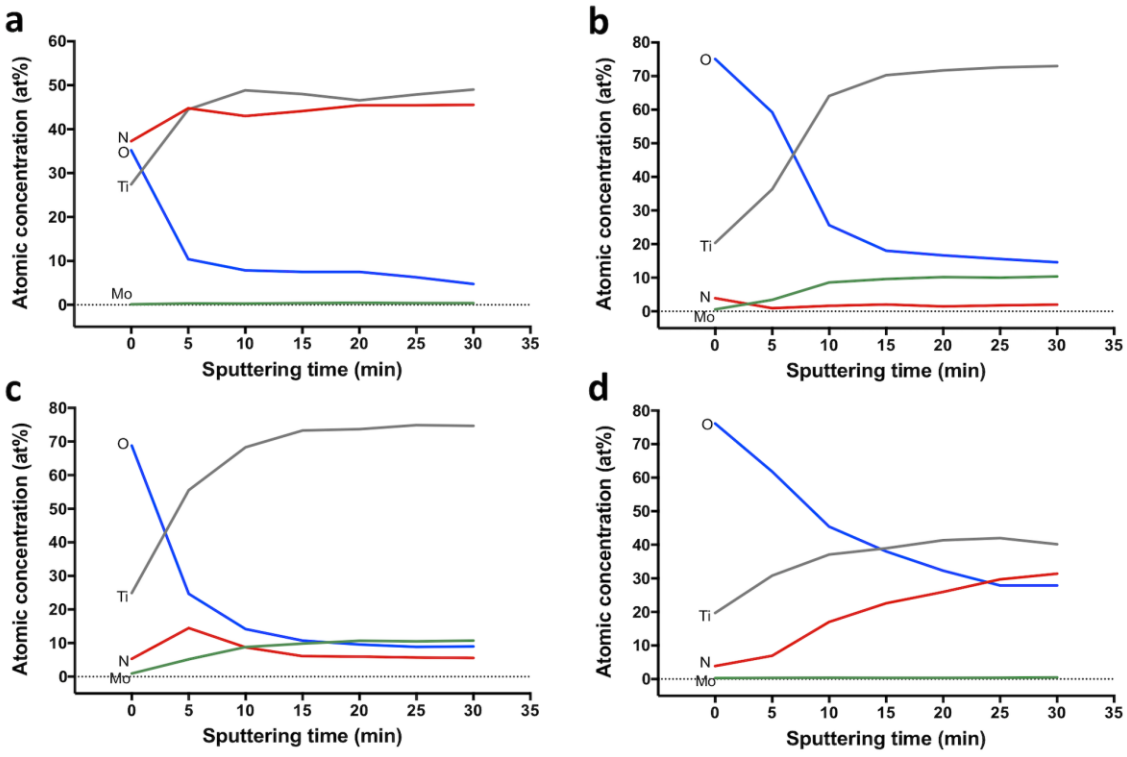

Figure 3.7. XPS results of element depth profiles for (a) laser-N_2 sample before corrosion test (b) untreated sample after corrosion test (c) laser-Ar sample after corrosion test (d) laser-N_2 sample after corrosion test

After the potentiodynamic polarization test, the element depth profiles of all three types of samples (non-scanned, laser-Ar and laser-N_2) were tested by XPS for comparison of the oxidized layer thickness. For the untreated samples (Figure 3.7 (b)), the oxygen concentration remains high in the first 5 minutes, but dramatically decreases after 10 minutes Ar^+ sputtering. In contrast, for the laser-Ar samples (Figure 3.7 (c)), the oxygen concentration changes rapidly within the first 5 minutes Ar^+ sputtering. This thin oxygen-containing layer indicates a good corrosion performance for the laser-Ar sample, in comparison to the untreated samples. The improvement in corrosion behavior of laser-Ar sample is likely due to the β-Ti rich layer, generated from the laser treatment. The formation of a passive layer on the laser-Ar sample is much slower than the non-laser scanned sample case, indicating that the β-Ti rich surface is more stable than the untreated surface.

For laser-N_2 samples, Figure 3.7 (d) shows that the oxygen level remains high for the first 5 minutes and then gradually decreases during the 30 minutes Ar^+ sputtering and the Ti and N ratios are approaching 1:1.

3.3.3 Biocompatibility

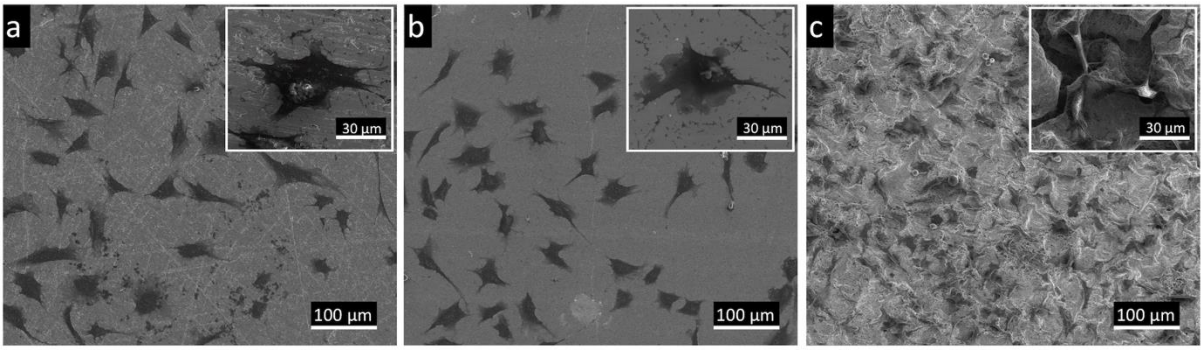

Figure 3.8. Cell density and morphology for (a) untreated sample surface (b) laser-Ar sample surface (c) laser-N2 sample surface

Biocompatibility results can be found in Figure 3.8 to Figure 3.10. The SEM images (Figure 3.8) show that all samples under three different conditions can support the attachment of MLO-Y4 cells within 24h of incubation. The cells are randomly distributed on the sample surfaces with showing polygonal shapes, which is different from the initial round shape when

seeded in α-MEM. However, on laser-N_2 sample surface, some cells appear to have an elongated nucleus with the filopodia build across the undulations of the samples surface. The cells on the laser-N_2 sample surface appear smaller than those on the untreated and laser-Ar samples. This difference indicates that the cell morphology is sensitive to sample surface roughness and/or compositions.

Figure 3.9 shows composite cell viability images for three different types of Ti-Mo samples. All cell nucleus are stained in blue color and the dead cell nucleus are stained in red color. With overlapping, purple colored dots indicate dead cells and blue dots indicate live cells. As shown in Figure 3.10 (a), the cell density of laser-N_2 sample is significantly higher than that of the untreated and laser-Ar samples. Compared with the initial cultured cell density, the cell densities of all samples are increased, which indicates that all Ti-Mo alloy samples would allow MLO-Y4 cell to integrate and proliferate within the 24h of incubation.

The relationship between sample surface properties and cell responses are the result of a complex biological system that includes protein adsorption, receptor-ligand binding and signal transduction [42]. In this study, the laser-N_2 process generated a rough TiN coating on the Ti-Mo alloy samples and the cell culture experiments demonstrated that the laser-N_2 sample surface is more favorable for cell growth. This improvement results from the roughened surface and the higher surface energy of TiN. Firstly, Roughened surfaces are known to enhance the adsorption of fibronectin [8],[42,64,65]. Fibronectin is recognized as one of the key proteins mediating cell adhesion. Hove et al. indicates that both porous and smooth TiN surfaces can improve the proliferation of MC3T3-E1 osteoblast cell compared with that on CoCrMo surface [66]. Brinkmann et al. demonstrates that osteoclasts have improved activities on rough titanium surfaces [67]. Secondly, Balla et al. reported that TiN has higher surface energy compared with Ti6Al4V and surface energy rises in concert with TiN concentration increases [60]. Ng et al. also indicates that TiN has increased hydrophilicity and surface energy compared with Ti-Nb

alloy [44]. Different surface energy and charge polarity can alter the binding of inorganic ions (e.g., Ca^{2+}, Cl^{-}, Na^{+}, HCO_3^{-} etc.) and organic cell adhesive proteins (e.g., fibronectin, vitronectin etc.) [68]. Higher surface energy contributes to increased cellular adhesion and proliferation on metal surfaces [68,69]. Besides, the rough TiN surface prepared under laser scanning can also increase the friction force, thereby improving the initial implant stability by limiting the micro-motions between the bone and implant [70]. In addition, TiN layer is non-toxic and can enhance the implant hardness and wear resistance [47].

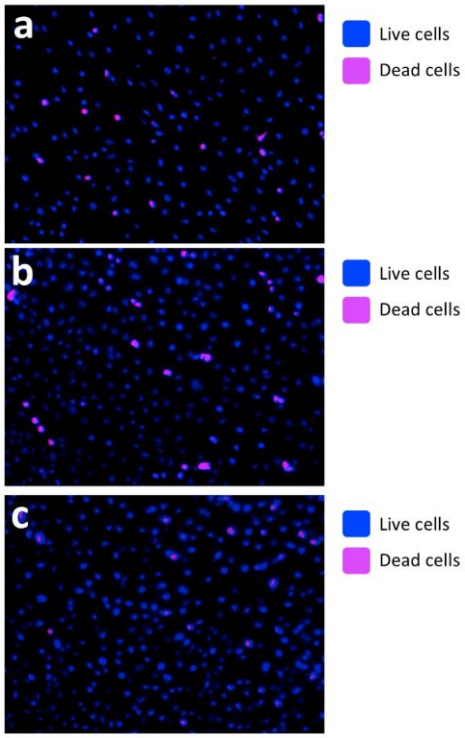

Figure 3.9. Composite cell viability image of (a) untreated sample (b) laser-Ar sample (c) laser-N_2 sample. Blue dots indicate live cell nucleus, purple dots indicate dead cell nucleus

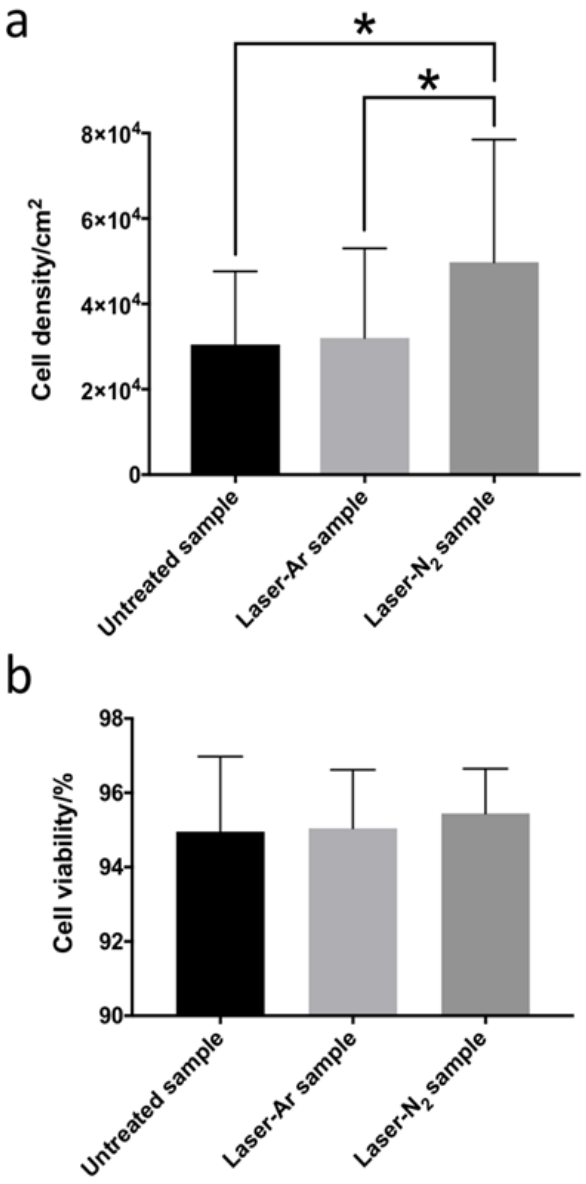

Figure 3.10. (a) Cell densities (b) cell viabilities of different surface conditions. $p<0.05$ is strategically significant and is denoted by *. All data are presented as mean ± standard deviation (SD)

3.4. Conclusions

Laser scanning in an Ar environment promotes the formation of a β–Ti-rich layer on the Ti-10Mo alloy surface and improves electrochemical behavior, even though the element distributions on the surface remain the same. Laser scanning based surface modification in a N_2 environment forms a TiN layer with unique corrugated features on the surface of Ti-10Mo alloy. This rough TiN coating, with higher surface energy than base Ti-10Mo alloy, is found

to act as a barrier to protect substrate material from corrosion and to improve cell integration. The laser-based surface modification under N_2 environment for Ti-Mo alloys has the potential to improve the peri-implant bone healing process and the integration between bone and implant, thus increase implant success. The elongated and smaller sized cells on the rough TiN surface prepared by laser surface modification warrant further investigation.

Chapter 4. The Mechanical Performance of 3D Printed Ni939

4.1 Introduction

Recently, with the development of aerospace and oil industry, there are increasing demands on high-performance nickel based superalloys due to their excellent creep performance, fatigue strength, tensile properties and corrosion resistance at high service temperatures [10,71]. Some of the nickel based superalloys have already been widely applied in aerospace, marine, chemical and petrochemical industries [71], for example Inconel 718 alloy, which can be used up to 650 °C as turbine rotor disc, thin-walled hollow blade and high-pressure pipe [10,72]. A lot of studies have been performed to investigate the mechanical properties of Inconel 718 superalloy manufactured using SLM, and a better tensile property was achieved due to the smaller grain size of SLM samples after solution and ageing heat treatments [72–75]. However, for applications at higher temperatures up to 850 °C, Inconel 718 alloy is no longer qualified and other nickel-based superalloys are needed. Inconel 939 is one of the promising candidates and its cast alloy has already been used in combustion chamber of turbines [10]. Several studies were carried out on the Inconel 939 alloy, and it was pointed out that the presence of coherent γ' precipitates in the cast or SLM samples after solution annealing and single stage ageing improved the high temperature performance [10,76,77].

SLM is a novel additive manufacturing (AM) technique which has been widely applied in AM industry. It has many advantages compared with traditional manufacturing methods (i.e. casting and forging), which produces a part with higher production efficiency, material utilization ratio, dimensional accuracy and manufacturing freedom [72]. In recent years, the demand for complex-shaped Inconel superalloy parts with different wall thicknesses dramatically increases, therefore SLM becomes the ideal manufacturing technique for these new applications [78]. However, due to the ultra-high temperature gradient and cooling rate introduced by laser processing, the SLM parts usually contain defects such as pores and cracks

due to the high thermal stress and micro-segregation. Therefore, post-heat treatments need to be conducted to satisfy the requirements of service conditions. The traditional heat treatments (i.e. annealing, ageing) can only help to develop the desired phases of the material but have limited effects on eliminating the defects in SLM samples.

In order to reduce the defects in SLM samples, Hot Isostatic Pressing (HIP) is commonly applied, which involves both elevated temperature and high isostatic fluid pressure, with a dwelling time of several hours [79,80]. In comparison with HIP, SPS treatment not only can lower the heat treatment temperature and but also reduce treatment time (several tens of minutes) for parts with simple geometries, which is more energy efficient [81]. The SPS treatment is conducted using a conventional SPS machine, which exerts a pulsed DC current with a uniaxial pressure on the sample, and a localized heating will be generated in the sample and the graphite die. Along with the pressure, defects inside the sample can be reduced due to plastic deformation, creep, and diffusion bonding. Therefore, SPS treatment can be an alternative way for post heat treatment of SLM samples. However, to the best knowledge of the author, the application of SPS as a heat treatment strategy for AM parts has not been reported before. To reveal the effect of SPS treatment on the SLM samples, microstructures, and mechanical properties of the samples both before and after SPS treatment were investigated in this study.

4.2 Experiment

4.2.1 Materials and fabrication

Spherical Inconel 939 alloy powders were supplied by LPW Technology, Inc, which were gas atomized with the particle size of 15 – 45 microns and the chemical composition is listed in Table 4.1. The cylindrical shaped SLM samples were prepared using a Concept-Laser Mlab cusing-R system (Lichtenfels, Germany) in Argon atmosphere with the residual oxygen level under 0.2 %. The processing parameters are as follows, laser power 95 W (continuous),

scanning speed 100 mm/s, hatch spacing 50 µm, layer thickness 25 µm and scan strategy "with islands" with island size 5 mm × 5 mm. The islands have a shift of 0.2 mm and the scan direction has a rotation angle of 90 degrees between adjacent layers. This scan strategy can reduce the residual thermal stress inside the sample during fabrication process [72]. Figure 4.1 (a) shows a schematic diagram of the scan strategy [82]. The height and diameter of the final printout cylinder were 30 mm and 14 mm, respectively, as shown in Figure 4.1 (b). The cylinders were cut off from the build platform using a wire Electrical Discharge Machine (EDM).

Table 4.1. Elemental composition of Inconel 939 powders

Elements	Al	B	C	Co	Cr	Fe	Mg	N	Nb	Ni	Si	Ta	Ti	W	Zr
Content (wt.%)	1.9	0.01	0.15	19.2	22.3	0.1	<0.1	0.01	1.0	Bal	0.1	1.5	3.6	2.0	0.11

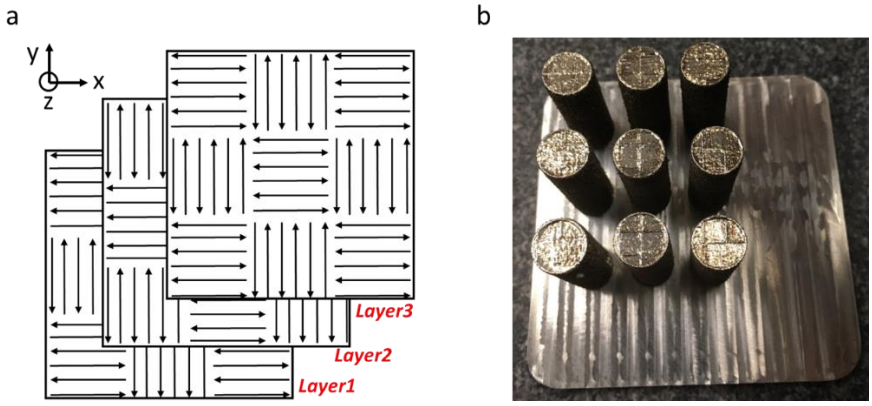

Figure 4.1. (a) Schematic of island laser scan strategy [82] (b) Image of the final print out samples

4.2.2 SPS heat treatment

Figure 4.2 shows the schematic of the SPS machine setup, which has a vacuum chamber indicated by the green box. Prior to the heat treatment, the samples were mechanically ground using SiC papers (600 grit size) to ensure the bottom and top surfaces were parallel and flat. Then the cylindrical shaped sample was wrapped with a graphite foil to ensure easy removal from the graphite die. Afterwards, the sample was put inside the assembly of the graphite die

and two graphite punches before being placed in the furnace chamber. The pressure and pulsed DC power were applied to the sample at the same time. The Fuji SPS system (SPS-211Lx, DR. SINTER LAB, Japan) was used to perform the heat treatment with a ϕ15mm (inner diameter) graphite die. Two target temperatures 800 °C and 1200 °C were chosen. In the remainder of this chapter, the samples are denoted as 800-SPS and 1200-SPS for better distinguishing. 800 °C is usually used as aging treatment temperature and 1200 °C is the solution treatment temperature for nickel based superalloys [10,72,77,83,84]. According to conventional heat treatment process, the purpose of solution heat treatment is to dissolve all the elements into matrix and the ageing heat treatment is to precipitate the γ' phases which has better corrosion and mechanical properties at high temperatures compared with other phases [83]. The as fabricated sample was used for comparison and was denoted as AF sample. During the heat treatment process, the pressure applied to the sample was set as 50 MPa, and the temperature was raised from room temperature to 800 °C and 1200 °C with a rate of 50 °C/min (a pyrometer was used to monitor the temperature), and then the samples were kept at the target temperatures for 5 minutes before cooled down within the chamber to room temperature.

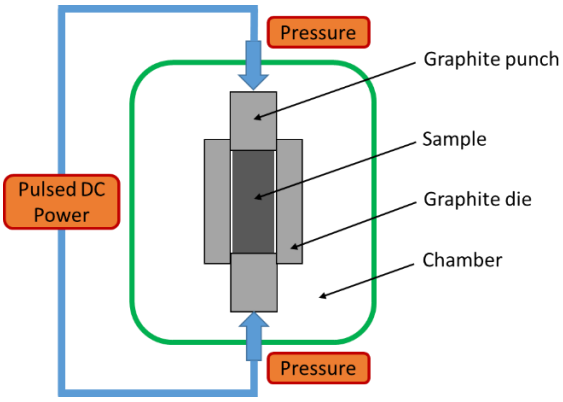

Figure 4.2. Schematic of the SPS setup

4.2.3 Material characterization

A 3 mm thick disk was cut off from each sample for material characterization. The top surface of each sample was mechanically ground using SiC papers of different grit sizes (400, 600, 800, 1000 and 1200 grits successively), then polished with the MetaDiTM Supereme

polycrystalline diamond suspension (6 μm, 3 μm, 1 μm, in sequence). After polishing, the sample surfaces were etched using etching solution, which was nitric acid and hydrochloric acid mixture with volume ratio of 1:3. Finally, the microstructures of sample surfaces were characterized with a Quanta™ 3D DualBeam™ FEG FIB-SEM scanning electron microscope (SEM). The sample phases were investigated on the polished surfaces using a PANalytical X-ray diffraction (XRD) with Cu Kα radiation with wavelength of 1.5406 Å. θ-2θ scans were performed over an angular range of 30°-100° with a scanning step size of 0.026°.

4.2.4 Hardness measurement

Prior to the hardness test, the sample surfaces were mechanically ground and polished with the same procedure as mentioned above. Then the Vikers Hardness test was conducted using SUN-TEC CM-802AT(V/K) hardness testing machine, and 10 hardness values in total were obtained on each sample surface. To avoid the effect of work hardening, the spacing between adjacent testing spots was over three times the diagonal of the indentation. Data were analyzed by one-way Analysis of Variance (ANOVA) method and were presented as mean ± Standard deviation (SD). P-value was used to quantify the statistical significance. $p<0.05$ was considered statistically significant.

4.2.5 Tensile test

Limited by the size of the SLM printed sample, regular dog bone design is not suitable for the small sample. The design of the mini-sized dog bone used for tensile testing is shown in Figure 4.3 (a). The long side of the sample is the SLM build direction, which is indicated by the red arrow. Three dogbone samples of each heat treatment condition were manufactured using wire EDM to ensure the repeatability of the test results, and the image of the samples is shown in Figure 4.3 (b). A set of custom designed grip adapter, which can match the dog bone shoulder, was made by wire EDM machine using Alloy-X nickel rod purchased from

McMaster-Carr. The tensile test was performed on a MTS Alliance RF/100 tensile tester (Figure 4.3 (c)) at room temperature, and the selected strain rate was 8.3×10-4 /s.

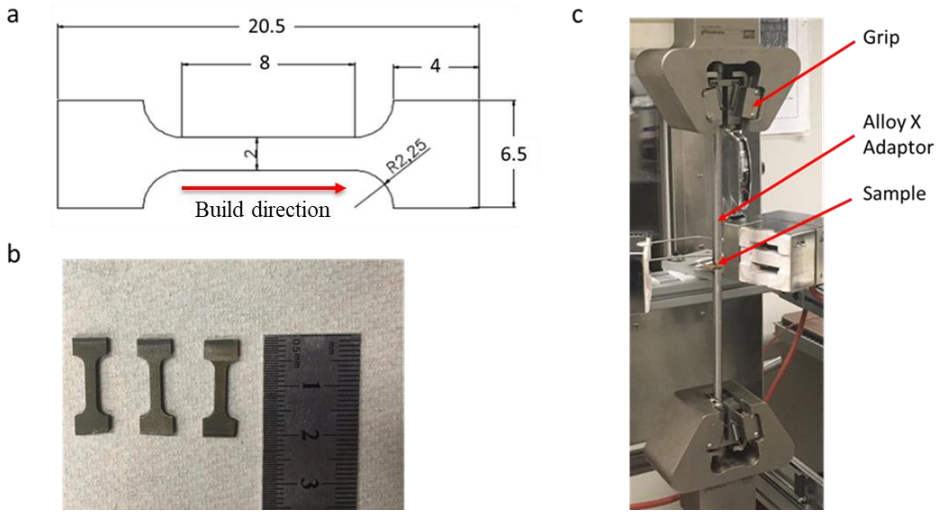

Figure 4.3. (a) The drawing of small sized dog bone sample for tensile testing, (b) image showing the real dog bone samples, (c) image illustrating the setup of tensile tester with Alloy X adaptor

4.3 Results and discussions

4.3.1 Phase constituents and microstructures

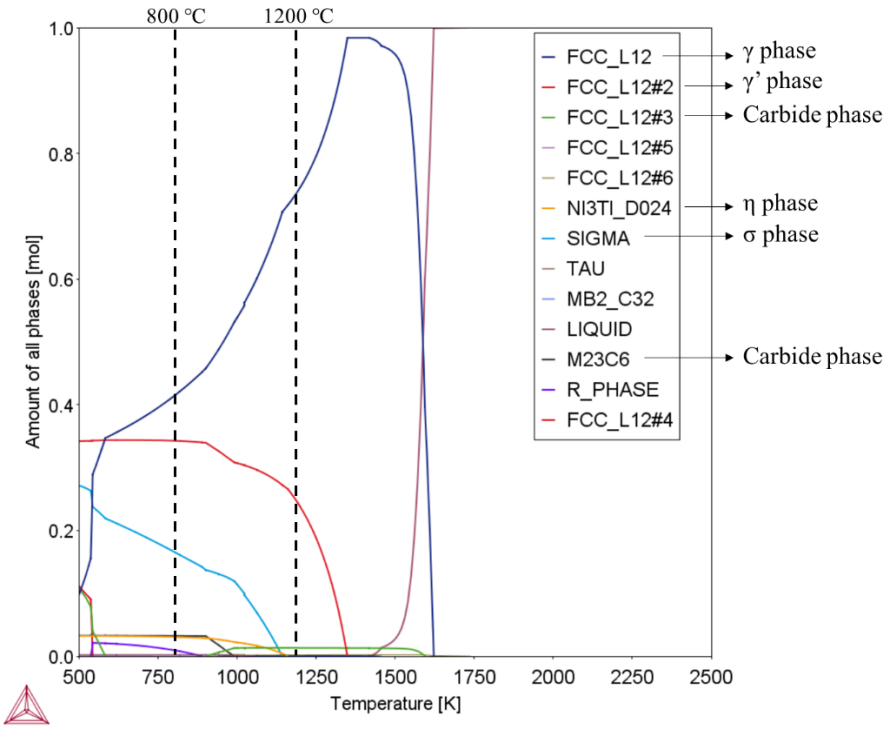

Figure 4.4. The amount of all phases at different temperatures for Inconel 939 alloy obtained from CALPHAD calculation

For a better guidance of the experiments and phase investigation, CALculation of PHAse Diagrams (CALPHAD) calculations were performed using Thermo-Calc software package with TCNI8 database (Ni-Alloys v8.2). Figure 4.4 shows the CALPHAD calculation results which describes the relation between temperatures and the amount of all phases at equilibrium states. It can be found that at 800 °C, the main phases are γ (FCC_L12), γ' (FCC_L12#2), σ (SIGMA), η (NI3TI_D024), and carbide phases (M23C6); at 1200 °C, the main phases are γ (FCC_L12), γ' (FCC_L12#2), carbide phases (FCC_L12#3).

Figure 4.5 shows the XRD results for the samples. Generally, the diffraction patterns of the three samples are almost identical except several small peaks for minor phases. According to Figure 4.5, the main diffraction peaks are FCC structure, which belong to the combination of γ and γ' phases based on the calculation results in Figure 4.4. Similar XRD patterns were also observed by previous study. γ and γ' phases have very close lattice parameters, and therefore the diffraction peaks overlap each other [72]. Besides, weak MC carbide phase peaks (around 35.5°) can also be observed in all the three samples, and based on CALPHAD calculations M can be elements of Ti, Nb, Zr and Cr. No obvious difference between the patterns of AF and 1200-SPS samples are observed. However, a small peak at about 47.0° which corresponds to η and σ phases was observed in 800-SPS sample. Similar XRD results with the 800-SPS case were also obtained by other researchers for Inconel superalloys with different manufacturing methods and treatment temperatures [10,76,78,85]. According to the CALPHAD calculation results shown in Figure 4.4, this observation is associated with the segregation of Ta, Cr and Co which are the elements to form η and σ phases. The reasons why the η phase and σ phase were not detected in the 1200-SPS sample and AF sample are discussed below. Firstly, as mentioned above, heat treatment at 1200 °C is commonly considered as solution treatment process for nickel base superalloys, which improves composition homogeneity of the alloys. Besides, the cooling rate of SPS process is

also high especially at high temperatures, which was reported to be several hundreds of degrees Celsius per minute depending on the sample size [86,87]. Therefore, the phases at 1200 ℃ tended to be retained after SPS treatment, which were mainly γ, γ' and MC phases according to both the CALPHAD calculation results in Figure 4.4 and XRD results in Figure 4.5. The SLM process is an extremely fast melting and solidification process, which is up to 10^6 ℃/s according to previous studies [88]. Such an extremely rapid heating and cooling process retained the high temperature phases, which are mainly γ and MC phases based on Figure 4.4. γ' phase may also exist in AF sample, however, which needs further confirmation with TEM tests. As observed form the XRD results, with different SPS treatment temperatures, different phases were obtained which can lead to different mechanical performance.

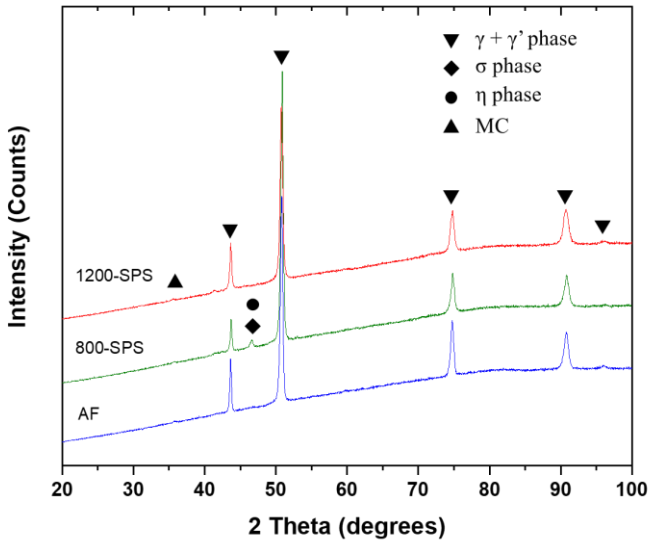

Figure 4.5. XRD test results of AF, 800-SPS and 1200-SPS samples

Figure 4.6 shows the SEM images for the samples at different magnifications. All the images were taken perpendicular to the building direction. Obviously, SPS treatment shows significant effects on tuning the microstructures of the samples. For AF sample, equiaxed cellular structure was observed with the size of around 1 μm as shown in Figure 4.6 (a)(b). Similar structures were also found by other researchers for 3D printed nickel based alloys [72,75,76,84]. In many cases, this microstructure leads to considerably higher strength due to the Hall-Petch effect [76]. White particles are also observed along the cellular structure

boundaries, and it was claimed that these partials are carbide phases [76,83,85]. In the AF sample, defects such as pores and cracks ranging from a few microns to hundreds of microns are obvious (Figure 4.6 (b)(c)), which indicates the poor quality of the SLM samples and necessary heat treatment needs to be performed in order to reduce the defects. It is worth noting that, beside the cracks and sharp-corner shaped defects, spherical pores with the size of several tens of microns (indicated by white arrows in Figure 4.6 (c)) are also visible in the AF sample, which are most likely the key-hole voids caused by excess laser energy input. Similar phenomenon was also reported elsewhere [89]. Interestingly, no such defects are observed in 800-SPS sample and 1200-SPS sample, indicating that they can be removed when the SPS treatment temperature is above 800 ℃.

In 800-SPS sample, flake like phases are uniformly distributed, and cellular structures are no longer observed. Furthermore, with a close observation of the microstructures, it is discovered that there are two kinds of flake like phases with distinguishable microstructures, one is needle shape with brighter contrast and another one is rod like with darker contrast. P. Kanagarajah et al. [10] claimed that the needle like microstructures are corresponding to topologically closed packed σ phase (chromium rich), while the rod-like microstructures are referred to hexagonal η-phase (nickel rich). This observation matches the CALPHAD calculation in Figure 4.4 and XRD results in Figure 4.5. Besides, some white dot like particles which are the carbide phases (MC) can also be observed on the sample surface. Cracks remain in the 800-SPS sample, as shown in Figure 4.6 (f), which indicates that heat treating at 800 °C may not be sufficient enough to fully eliminate the defects in the AF sample. Therefore, SPS treatment at 1200 ℃ was carried out.

According to Figure 4.6 (g)(i), when heat treated at 1200 °C, both the cellular structures and the flake like η and σ phases no longer exist in the sample, and grain structures are clearly visible. The disappearance of η and σ phases is ascribed to the fact that the heat treatment

temperature (1200 ℃) is higher than the solvus temperature of η and σ phases (about 1145 °C and 950 °C, respectively) [76]. Pores are observed along the grain boundaries of SPS-1200 sample, which is most likely due to the preferential etching effect of the etching solution. After heat treatment at 1200 ℃, the grain size becomes larger compared with the cellular structure in AF sample. Besides, the 1200-SPS sample has a large amount of nanoscale round particles which are shown in Figure 4.6 (h). P. Kanagarajah et al. [10] and J. Mohammadreza [85] had the same observations and their TEM and SEM images indicated that these were the γ' precipitates initially evolved during solution treatment but not fully grew due to the short holding time. Furthermore, much reduced defects are observed in the sample and the defects are more spherical shaped with the scale of few microns. This phenomenon can be explained by the following reasons. First, at higher heat treatment temperature (1200 ℃), the bulk deformation of the sample caused by the uniaxial pressure was enhanced due to the thermal softening effect, which effectively closed the defects (i.e. pores and cracks) inside the sample [90,91]. Second, due to the unique characteristics of SPS (pulsed current), microscopic spark discharges were reported existing in the gaps between powder particles [92,93]. Similarly, the spark discharges may also occur in the defects of the samples, heating up the surface of the defects, improving surface mass transfer by evaporation, condensation and diffusion [91,94]. Such mass transfer is beneficial for the formation of neck, which indicates that the mass transfer direction is preferentially towards the contact region of powder particles [95]. Correspondingly, sharp corners of the remaining defects were gradually filled with transferred mass, and the shapes of the defects gradually became spherical. Therefore, due to the pulsed current and pressure, the defects inside the 1200-SPS sample were closed and became spherical shape due to the plastic deformation and rapid mass transfer (evaporation, condensation and diffusion). Table 4.2 shows the density and porosity values of the samples. It is obvious that

porosity decreases with the increase of the heat treatment temperature, which is in line with the microstructure information.

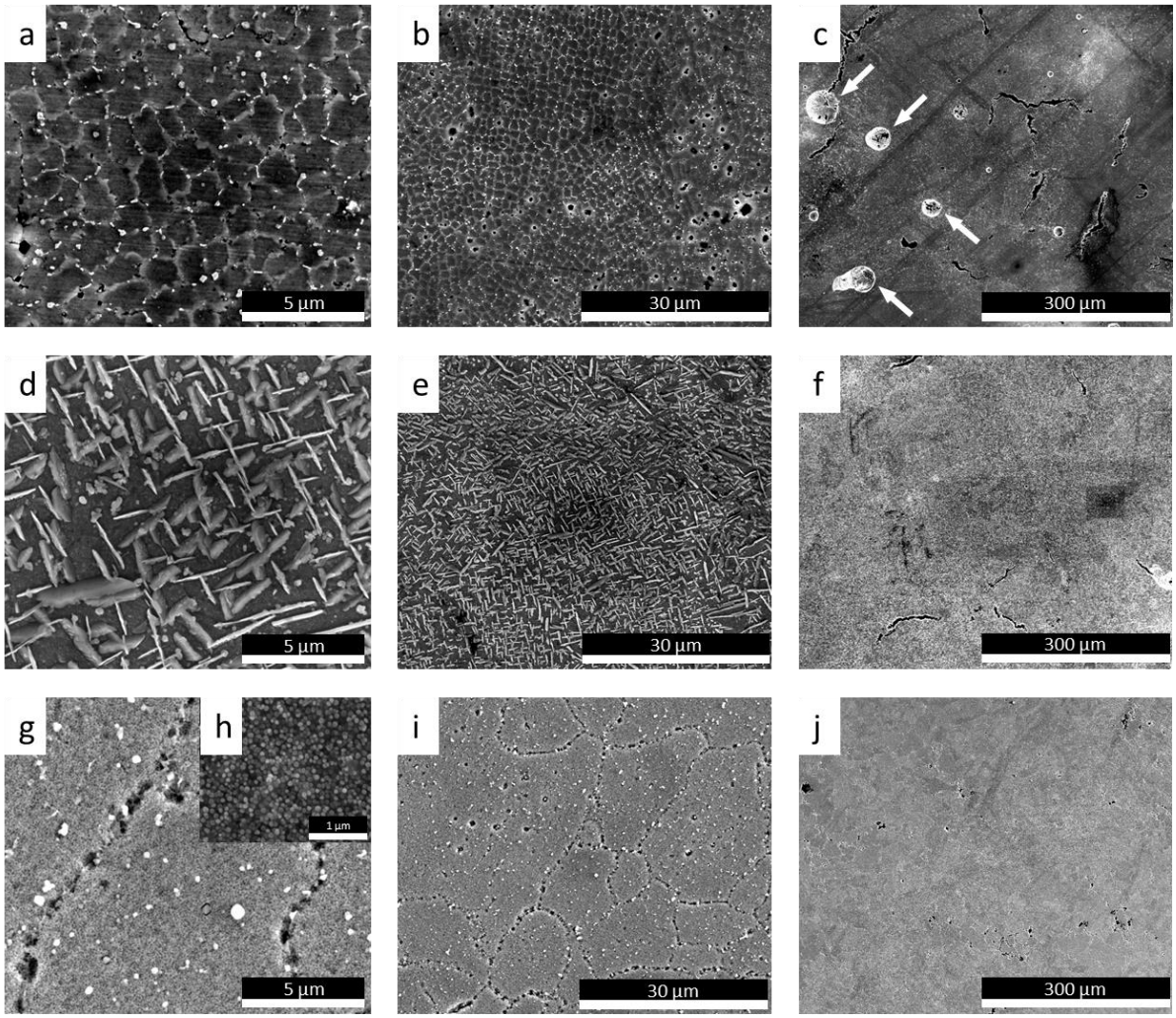

Figure 4.6. SEM images showing the microstructures of the samples with different magnifications. (a) (b) (c) AF sample; (d) (e) (f) 800-SPS sample ; (g) (i) (j) 1200-SPS sample; (h) is the detailed view of (g) inside the grain with higher magnification

Table 4.2 Densities of the samples measured by Archimedes principle

Sample name	Density (g/cm3)	Porosity (compared with casted Inconel 939 (8.17 g/cm3)) / % [96]
AF	7.866	3.72
800-SPS	7.936	2.86
1200-SPS	8.040	1.59

4.3.2 Hardness test result

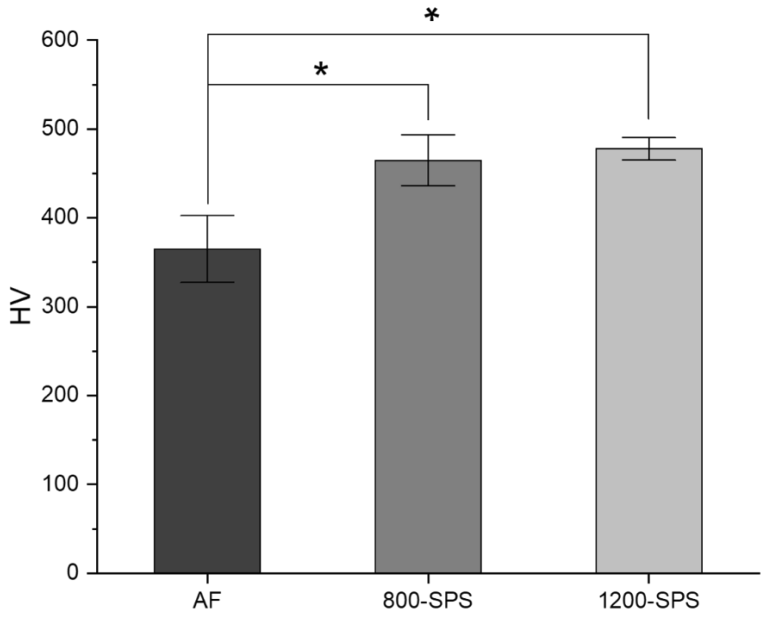

Figure 4.7. The hardness test results for samples in different conditions

The hardness test results are shown in Figure 4.7. Obviously, the hardness value of AF sample is dramatically lower than that of the 800-SPS and 1200-SPS samples. It is denoted by * to show statistically significant. This observation can be explained as follows. According to the phase and microstructure analyses (Figure 4.5 and Figure 4.6), it is clear that compared with AF sample, although no cellular structures are visible, η and σ flake like phases and nano-sized γ' phase exist in the 800-SPS sample and 1200-SPS sample, respectively. Based on previous studies, σ phase is a brittle phase, and the hardness of η phase is much larger than that of the matrix (γ phase) [85,97]. Therefore, both of the phases act as barriers to dislocation motions, causing precipitation hardening effect that increases the hardness of the 800-SPS sample [72]. Similar phenomenon was also reported by previous study [98]. In the SPS-1200 sample, γ' phase serves as the strengthening phase because its hardness (8-11 GPa) is much larger than that of the γ matrix (2-5 GPa) [99]. Due to the coherent relation between γ phase and γ' phase, the hardness of the material is effectively improved. According to Figure 4.7, no significant difference of hardness was observed between 800-SPS sample and 1200-SPS

sample. However, the hardness of σ phase and η phase at room temperature were reported around five times and two times of that of γ' phase, respectively [85,100]. Hardness of 800-SPS sample was expected higher than that of 1200-SPS sample. This discrepancy is attributed to the precipitate size in the samples. σ phase and η phase are flake like structures, with the width of several hundred nanometers and the length of several microns, while γ' phase in 1200-SPS sample is particle shape with much smaller size (several tens of nanometers). Strength increase (σ_p) due to precipitates is described as

$$\sigma_p = k\frac{f}{r} \qquad (2)$$

Where, k, f, and r are constant, volume fraction of the precipitates, and average diameter of the precipitates, respectively. Assume that the amounts of precipitates in 800-SPS sample and 1200-SPS-sample are close, the γ' phase with much smaller size is more efficient in strengthening the material, even though it shows much reduced hardness compared with σ phase and η phase. Similar observation was also obtained elsewhere [85]. Besides, standard deviations of hardness for the AF sample and 800-SPS sample are larger than that of the 1200-SPS sample, which is most probably due to the much-decreased defects (i.e. cracks and pores) in the latter.

4.3.3 Tensile test result

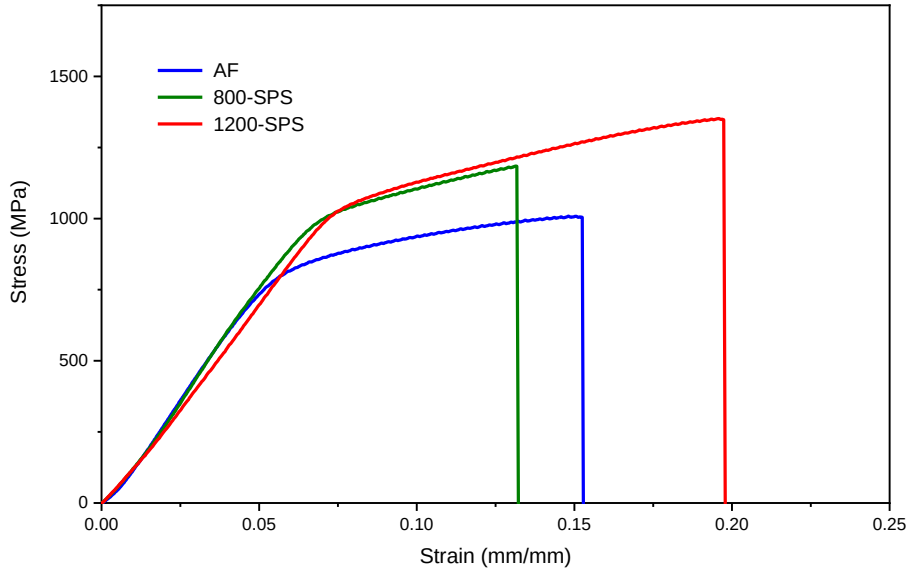

Figure 4.8. Image showing the tensile test results for the samples at room temperature

Table 4.3. Values of tensile test results for the samples at room temperature

Sample name	Yield strength (MPa)	Ultimate tensile strength (GPa)	Strain-to-failure value (mm/mm)
AF	720	0.981	0.153
800-SPS	900	1.149	0.132
1200-SPS	950	1.294	0.196

As shown in Figure 4.8 and Table 4.3, the SPS-1200 sample has both the highest strength (yield strength and ultimate tensile strength) and strain-to-failure value. In contrast, the SPS-800 sample shows the medium strength but the lowest strain-to-failure value, and the AF sample exhibits the lowest strength but the medium strain-to-failure value. This observation is in line with previous studies [10,72,83]. The observed strengths of the samples are consistent with the hardness test results in 3.2, which is reasonable because the hardness and strength of the same material typically show linear relations with each other [101]. Therefore, similar to the analysis in 4.3.2, the strength improvements of the 800-SPS sample and 1200-SPS sample originate from the precipitates (σ and η phases in the former and nano-sized γ' phase in the latter), which restrain the movement of dislocations. However, the strength of the 800-SPS

sample is lower than that of the 1200-SPS sample, which is most likely due to the denser defects in the former. With close observation of the stress-strain curves in Figure 4.8, the curve slopes of the 800-SPS sample and the 1200-SPS-sample are a little bit higher than that of the AF sample, indicating a slightly higher strain-hardening rate of the former. This phenomenon is ascribed to the interactions between dislocations and precipitates during the plastic deformation process. Back-stress to the following dislocations is generated and accumulating by either the former dislocations cutting through the precipitates (leaving residual stress) or the dislocation bypassing the precipitates by looping them [102].

Compared with the AF sample, the 800-SPS sample shows a reduced strain-to-failure value, while the 1200-sample displays a significantly improved value. According to Figure 4.6 (d), dense flake-like η and σ phases distribute uniformly in the 800-SPS sample, which increases the dislocation congestion and stress concentration that lead to microcrack generation and accelerate material failure [72,103]. Besides, η and σ phases are more brittle compared with γ and γ' phases, which can also result in the decrease of the strain-to-failure value [10]. The enhanced ductility of the 1200-SPS sample is due to the following reasons. First, compared to the other two samples, the 1200-SPS sample contains much reduced defects, especially the crack-type defects (as shown in Figure 4.6 (c)(f)(j)), and the remaining defects are mainly spherical Figure 4.6 (j)), making the sample much less prone to stress concentration due to sharp corners. Second, the shapes of the nano-sized γ' phases are particle-like, showing no clearly sharp corners, which are unlike that of the η and σ precipitates in the 800-SPS sample. Again, the 1200-SPS sample shows a lower tendency to stress concentration. Thirdly, due to the nanosize and relatively soft feature of γ' phase in 1200-SPS sample, the interaction between dislocation and the γ' nano precipitates was reported as cutting through type (a shearing mechanism), which was beneficial to maintaining a good ductility of the material [102].

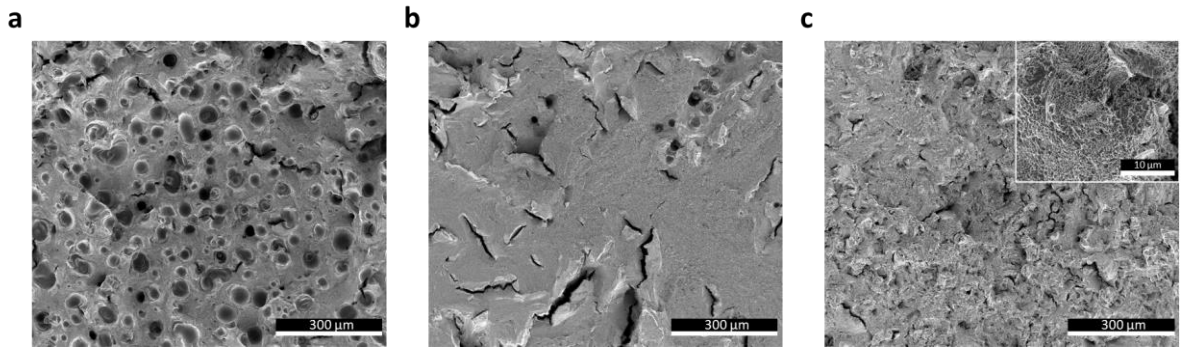

Figure 4.9. SEM fractography after the tensile test (a) AF sample (b) 800-SPS sample (c) 1200-SPS sample

Figure 4.9 shows the SEM fractography after the tensile test. For the AF sample (Figure 4.9 (a)), a large number of dimples are evenly distributed in the fracture surface, which is a typical feature of ductile failure [104,105]. The dimples are formed from microvoids initiated from the MC carbide phase and the micro pores in the AF sample, and the voids will grow by plastic deformation and will coalesce with adjacent voids to form coarser dimples [106,107]. However, due to the large amount of defects, the AF sample only shows the medium deductibility among the three samples. For the 800-SPS sample, as shown in Figure 4.9 (b), the fracture surface is much smoother compared with the other two conditions. Combining the fact that the 800-SPS sample has the worst strain-to-failure value, this fracture is more like a brittle fracture. Besides, some obvious straight cracks formed on the fracture surface, which are most likely originate from the brittle η and σ phases, since the cracks have a similar shape and orientation as the brittle phases [10]. From the detailed view of Figure 4.9 (c), it indicates that the 1200-SPS sample has the dimpled intergranular fracture since many micro voids can be observed at localized strain discontinuity [104,107,108]. The γ’ nano precipitates in the 1200-SPS sample can restrain the movement of dislocations, which can prevent the microvoids from coalescing.

4.4 Conclusion

In this chapter, SPS heat treatment was performed on Inconel 939 SLM samples at 800 ℃ and 1200 ℃ with a pressure of 50 MPa. The phase compositions, microstructures, hardness and tensile tests characters were investigated before and after heat treatment. And the main findings are summarized as follows:

- SPS can be a potential post heat treatment technique for reducing defects in SLM samples. With the increase of the treatment temperature, the defects were gradually removed. Crack-like defects were negligible in the 1200-SPS sample, and the remaining defects became more spherical-shaped.
- Typical cellular microstructures were observed in the AF sample, which, however, no longer existed in the heat-treated samples. Flake-like precipitates (η and σ phases) appeared in the 800-SPS sample, and nano-sized γ’ phase generated in the 1200-SPS sample.
- The hardness and the tensile strength of the 800-SPS sample was increased due to the flake-like η and σ phases. However, the strain-to-failure value was decreased due to stress concentration (at the sharp corners of both the precipitates and the crack-like defects) and precipitate brittleness.
- The 1200-SPS sample showed the highest tensile strength and stain-to-failure value attributed to much reduced defects (especially the crack-like defects) and the nano-sized particle-like γ’ phase.

Chapter 5. Apply Deep Learning for Materials Science

5.1. Introduction

The first computer program which could learn checkers game was developed in 1952 by Arthur Samuel. In 1958, the first generation of artificial neural networks called Perceptron was designed and used for pattern and shape recognition. Since the start of the 21st century, many researchers and businesses have realized the potential of machine learning (ML) to improve the efficiency of human tasks. After that, machine learning has been widely applied in machine vision recognition, game playing, economic analysis, data mining, bioinformatics and many other areas [16–19]. ML is a subset of artificial intelligence which uses ML algorithms and statistical models to perform a particular task without conventional human interventions. ML models learn from examples and experience in the form of data instead of hardcoded rules that instruct the machine to solve a problem step by step [109]. ML can learn a particular function by given a specific set of data from which the ML model can learn. In many areas, ML is already able to achieve a higher level of performance than humans. Based on the amount and type of supervision needed during training, ML can be classified into four major categories: supervised learning, unsupervised learning, semi-supervised learning, and Reinforcement Learning [110].

Artificial Neural Network (ANN) is one of the main ML algorithms in supervised learning and it is the core of Deep Learning (DL). DL uses layers of algorithms to pass information through each layer, and the next layer will take the output of the previous layer as input. The first layer and the last layer are called the input layer and output layer, and all the layers between the two are referred as hidden layers. Each layer is typically a simple, uniform algorithm containing one kind of activation function. The character of this model requires a large amount of parallel computation, which will take a much longer time by central processing units (CPUs). However, with the tremendous increase in computation power of Graphics

Processing Units (GPUs), large ANNs can be trained in a reasonable amount of time. ANNs have the ability to learn and model non-linear and complex relationships and it can make the models generalize and predict on unseen data.

Another important model in DL is called Convolutional Neural Networks (CNNs). It has been used in image recognition since the 1980s. It has beaten many other models in some complex visual tasks. More and more researchers have put effort into developing DL models using CNNs, for applications like self-driving cars, image search, video classifications and even natural language processing (NLP) [110]. Besides, with the advantages of the large quantity of data and the computation power, DL has already been applied in many big projects such as Google Images, Apple's Siri, YouTube and DeepMind's AlphaGo. Beyond all these mainstream tasks, many researchers in other fields started to employ these methods to their fields, such as materials science. Experiments used to play very important role in finding and characterizing new materials, which is very time-consuming and expensive due to its high requirements on resources and equipment [111]. Nowadays, materials researchers rely on physical and chemical laws to conduct computer simulations and combine them with experiments, which dramatically decreases the time and cost of materials design [20][111]. Meanwhile, with the extensive data accumulated during large scale simulations and experiments in materials research, the big data driven ML can form a new approach in the study of materials science. In this chapter, my attempts of applying DL in material data predictions and object recognition will be discussed.

5.2. Using deep learning model to predict APBE

5.2.1 The approach

Because of the recent development of machine learning (ML) algorithms and the resounding success of data-driven efforts in other domains, informatics strategies are beginning to take shape within materials science [112]. Currently, materials researchers generate large

amounts of data from all different kinds of sensors or simulation models. The data driven informatics methods are becoming applicable to determine material properties that are hard to measure or compute using traditional methods [112]. The conventional material research technics, such as DFT calculations, MD simulations, typically require a long research and development cycle and have difficulty keeping pace with materials science requirements today. ML can substantially reduce the computational costs and shorten the development cycle; hence, it is one of the most efficient ways of replacing DFT calculations, MD simulations or even repetitive laboratory experiments [20].

In the study of Inconel 939 alloy, antiphase boundary (APB) separates two domains of the same ordered phase. The magnitude of the strengthening effect by γ' precipitates is closely related to the magnitude of antiphase boundary energy (APBE), which is an essential parameter in precipitation strengthening theories (PST) [113]. As a result, the APBE is a significant factor that is related to Inconel alloy fatigue life. Currently, many researchers are trying to use molecular dynamic (MD) simulations or other simulation methods to calculate the APBE [20,112,114]. However, for one alloy which contains many elements, it usually takes several days to calculate the energy at one temperature alone using high performance computers (HPC). In contrast, ML is a much faster and economical way to predict relatively close APBE values compared with the current simulation methods. The preliminary study reported in this chapter is on predicting the APBE of nickel superalloys based on element components and temperatures.

Fundamentally, all ML algorithms operate by extracting features from a set of training data provided by a human. Each feature will be corresponding to a label which is the value that needs to be predicted [115]. In this case, the features are the element compositions and temperatures, and the label is the APBE values. Each of the elements and temperature will act as inputs of the ML model and each input will be assigned with a weight w_i. After a linear

combination of all the inputs and a bias term, the value is fed into the non-linear activation function and then output a value. This process is called forward propagation. Figure 5.1 (a) shows this process in formula format. The output value will be compared with the label value which is the true value that provided by human. A loss function J(W) will evaluate the errors and calculate the derivative to each of the weight, which is to evaluate the contribution of each weight to the error. This process is called gradient descent or back propagation. Ultimately, the weights will be updated to minimize the error. Figure 5.1 (b) shows a simple back propagation example. A deep learning neural network contains several hidden layers between the inputs and outputs and all the nodes are fully connected, as shown in Figure 5.1 (c).

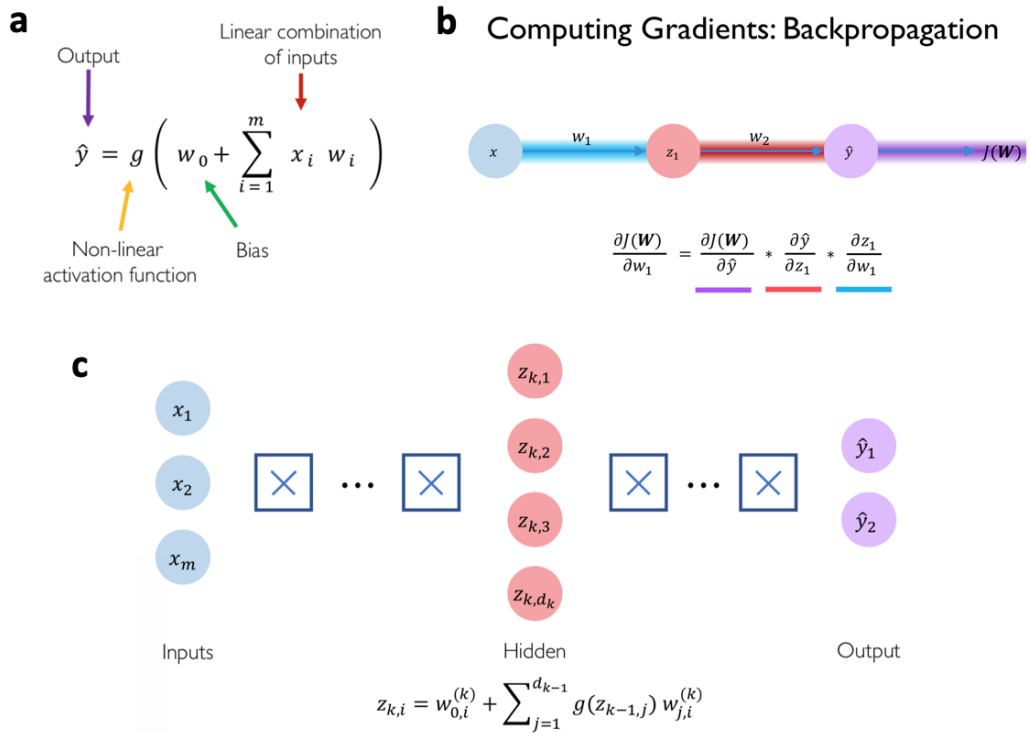

Figure 5.1. (a) forward propagation in formula format (b) an example of backpropagation (c) deep learning neural network [116]

5.2.2 Data preparation and the ML model

The codes are generated using Python in Jupyter Notebook and several ML packages are used, such as Pandas, Numpy, Matplotlib, Tensorflow etc. In the data set, I used simulation results from MD calculations. Because of the limitation of computational resources, only 162

data points are available for 3 elements nickel alloy and 24 data points for 5 elements nickel alloy. These data were provided by Mohammad Dodaran who is the Ph.D. student from Dr. Shao's group. These data were calculated by MD simulations with Monte Carlo sampling scheme. Table 5.1 shows some statistics about the data. Based on these data, a neural network was created which contains 3 hidden layers. The first two hidden layers have 100 nodes and the third hidden layer has 10 nodes. The output layer only has 1 node since only one output is needed. 'relu' is the activation function for all layers. All the 3 elements data points and 12 five elements data points were used as the training data. The fraction for the training data set and test data set is 0.8 and 500 epochs were performed. Table 5.2 shows the summary of the model.

Table 5.1. The statistics of training data

Inputs	Count	Mean	Std.	Min.	Max.
Ni	139	70.41	4.04	57.75	74.93
Al	139	22.77	3.29	8.74	24.98
Cr	139	0.84	2.03	0.00	9.00
Co	139	2.30	5.12	0.00	23.00
Mo	139	0.65	1.73	0.00	7.00
Ti	139	3.03	5.00	0.00	15.00
Temp.	139	800.72	350.05	300.00	1300.00

Table 5.2. The model summary

```
_________________________________________________________________
Layer (type)                 Output Shape              Param #
=================================================================
dense_48 (Dense)             (None, 100)               800
_________________________________________________________________
dense_49 (Dense)             (None, 100)               10100
_________________________________________________________________
dense_50 (Dense)             (None, 10)                1010
_________________________________________________________________
dense_51 (Dense)             (None, 1)                 11
=================================================================
Total params: 11,921
Trainable params: 11,921
Non-trainable params: 0
```

5.2.3 Results and discussion

Based on this model, the final test set mean absolute error is around 4 mJ/m^2. As shown in Figure 5.2, the mean absolute error for both training data set and test data set decreased

dramatically during the first 50 epochs. The test error kept at around 4 mJ/m^2 after 200 epochs. Figure 5.3 (a) shows the accuracy of the training data and test data: the orange dots are the training data and blue dots are testing data. The 45-degree line indicates the variance of predicted value with the true value. As shown in Figure 5.3 (a), most of the data are predicted accurately based on the deep learning model. However, there are two points which corresponding to low temperature APB energies are not able to fit in this model. A validation was also performed using the rest 12 five elements data points. It is can be found in Figure 5.3 (b) that the predicted values are very close to the true values for the APB energies at high temperatures. However, the low temperature APB energies are off from the 45-degree line. This might due to the lack of enough low temperature data and the model treats these data as noise since these points are far away from the regression curve. Typically, thousands of examples are needed even for very simple problems, therefore, the 162 data points available are not enough [110]. Besides, in order to generalize well, the training data should be able to represent of the new cases, however, the amount of high temperature data is much higher than the low temperature ones, which makes the model predict poorly for low temperature data. Finally, these data are all based on the simulation results and how accurate does these values compared with the real APBE values is still unknown. As a result, the model won't fit these data accurately if the training data is full of errors. Beyond the data, the deep learning model also has many parameters can be adjusted to improve the accuracy, such as hidden layer number, node numbers, learning rate etc. There is still more work to be done to optimize the model.

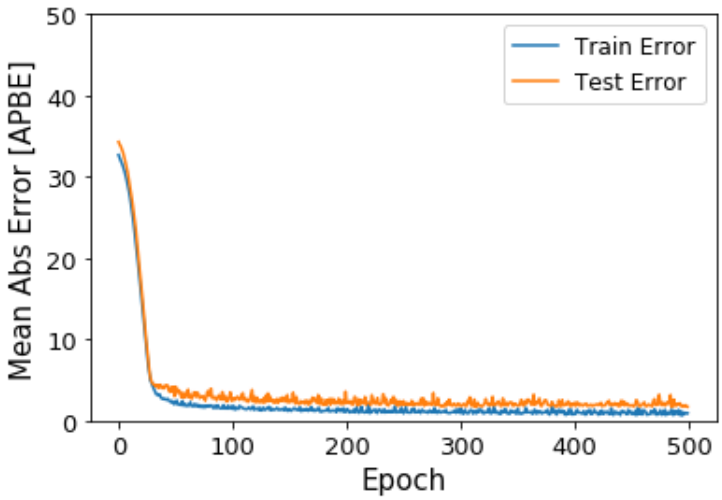

Figure 5.2. The mean absolute error change with epoch

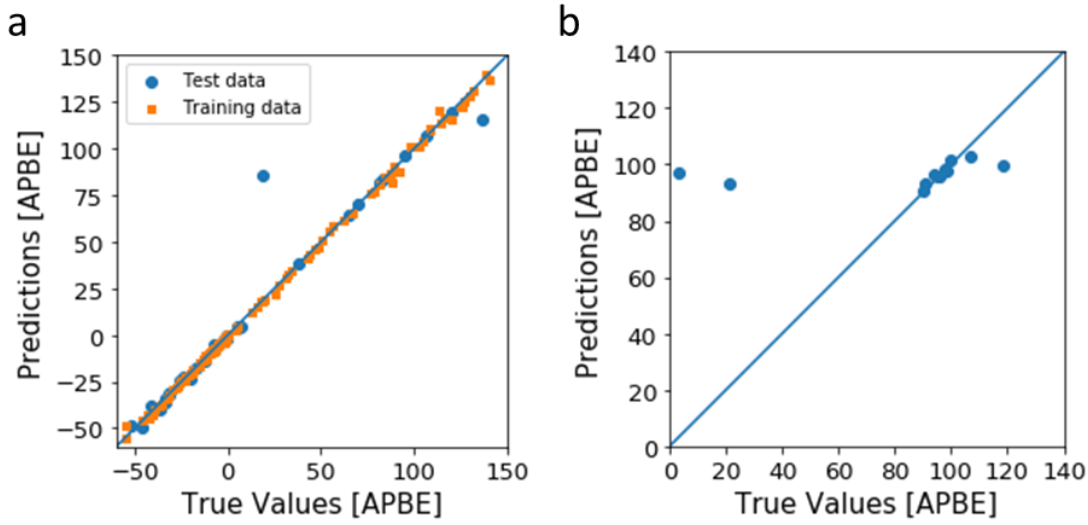

Figure 5.3. (a) the accuracy of training data and test data (b) the accuracy of validation data

Furthermore, the DL model is compared with two other models: Random Forest Regressor model and K Neighbors Regressor model. The Random Forest is an estimator which can fits numbers of classifying decision trees on various sub-samples of the dataset. It can use averaging to improve the accuracy and control overfitting [117]. The training and validation results of Random Forest Regressor model are shown in Figure 5.4 (a)(b). It can be found that the validation results are not as good as the DL model, even they achieved similar results in the training and testing process. K Neighbors Regressor is based on k-nearest neighbors, which can predict the target by local interpolation of the targets associated with the nearest neighbors

in the training set [118]. K Neighbors Regressor model training and validation results are shown in Figure 5.5 (a)(b). Figure 5.5 (a) indicates that most of the training and testing data are far away from the 45-degree line, and the validation result (Figure 5.5 (b)) is underperformed when comparing with DL model.

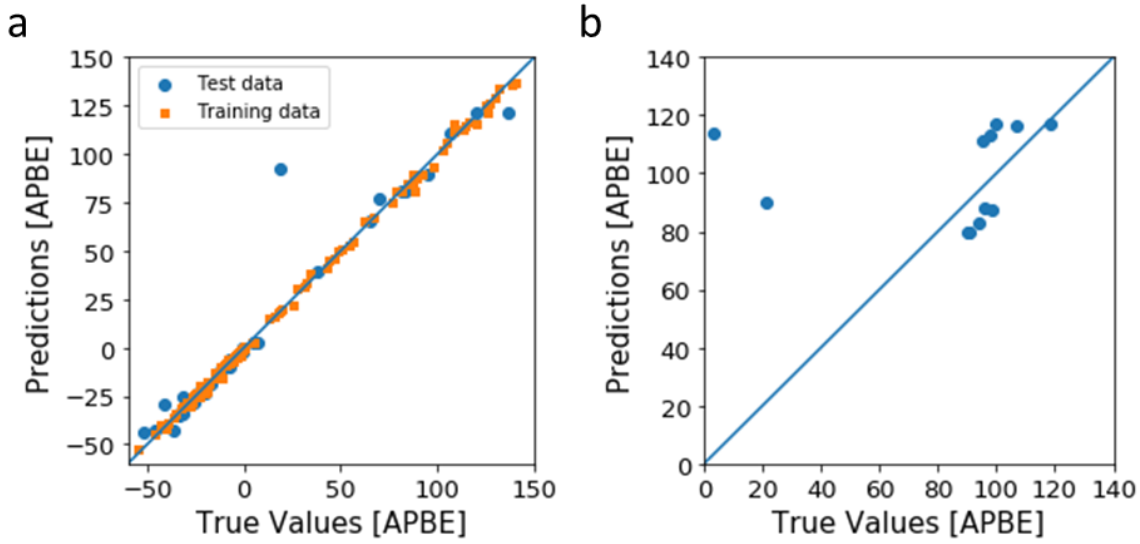

Figure 5.4. Random Forest Regressor model (a) the accuracy of training data and test data (b) the accuracy of validation data

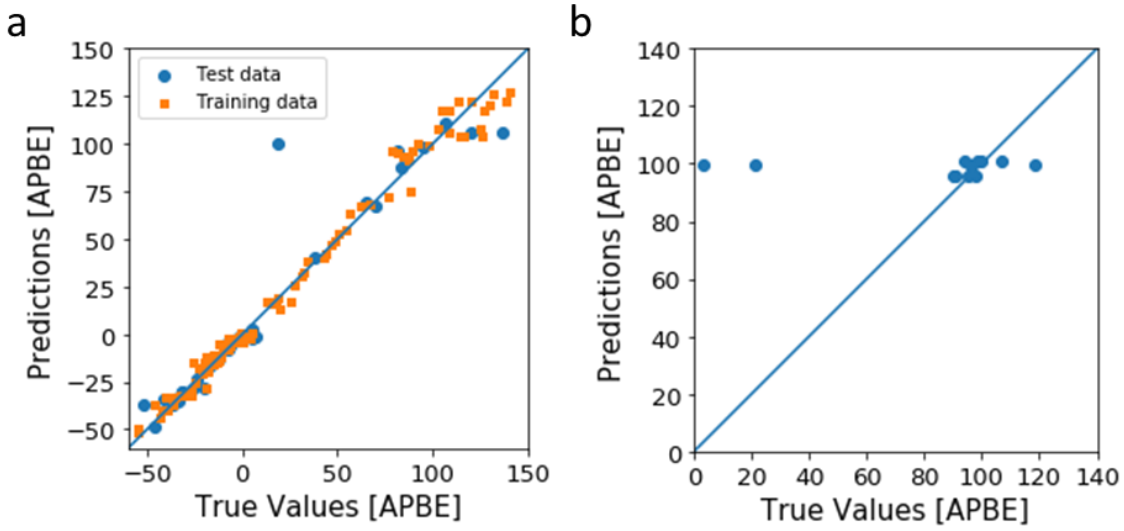

Figure 5.5. K Neighbors Regressor model (a) the accuracy of training data and test data (b) the accuracy of validation data

5.3. The application of Convolutional Neural Networks (CNNs) to recognize sample defects

5.3.1 Introduction

Convolutional Neural Networks (CNNs) have been used in image analysis since the 1980s and it is inspired by studying the brains' visual cortex [110]. CNN is a feedforward Artificial Neural Network (ANN) which can accept images directly as an input of the network to avoid complex preprocessing procedures that are carried out in traditional image recognition algorithms [20]. Due to the increase of computation power and available data, CNNs have achieved superhuman performance on many complex visual tasks, such as images search, self-driving cars, automatic video classification and more [20,110,119]. Over the past few years, many fundamental architectures have been developed, such as LeNet-5 architecture (1998), AlexNet (2012), GoogLeNet (2014), and ResNet (2015), which made the error rate fell from over 26% to only 3% in ILSVRC ImageNet challenge [110,120]. Meanwhile, the architecture gets deeper and deeper from only few layers to hundreds of layers.

Nowadays, SLM techniques are becoming widely used in different industries. One of the crucial aspects of SLM's application is to eliminate the defects, such as pores and cracks, in SLM printed parts. As SLM is a complicated process, and many conditions cannot be controlled during printing, the defects are hard to avoid initially, especially for some newly developed alloys. Therefore, applying multiple times of scanning using different printing parameters, such as scan speed, scan patterns, and laser power, can be used to eliminate different types of defects. As a result, automatic detection and classification of defect types are becoming a prevalent task for improving SLM parts' quality. With the rapid development of CNNs and their state-of-art results in various computer vision tasks, many researchers in the literature use different CNN models to detect and classify the images in other research areas. The purpose of this section is to demonstrate the capability of different CNN models for classifying and detecting cracks and pores, which are the two common defects in SLM parts.

This study provides a new perspective for eliminating cracks and pores using different scan strategies during the SLM printing process. There are three levels of complexity I attempted to achieve in this study. The level-one is defects classification; by using a simple CNN, the goal is to classify a defect in the image into either Crack or Pore. A simple CNN consisting three convolutional layers and two dense layers was used. The level-two is target detection; the model is designed to detect cracks and pores on a typical SEM image and draw a bounding box around the defects. The outcome of level-two study is the capability to provide defects location and type information for advanced AM processing control. The model I selected for target detection is YOLOv4, which is the latest variant (forth version) of a popular object detection algorithm YOLO – You Only Look Once [121,122]. This target detector is faster and more accurate than the other available detectors such as, LRF, SSD, M2Det etc; besides, it can be trained on conventional GPUs with 8-16 GB-VRAM which makes its broad use possible [121]. The third level of complexity I have attempted is image segmentation; besides providing the second level information, level-three model can also generate the defects' shape information, which can be used for further simulations and analysis under certain conditions. The level-three model I selected for image segmentation is Detectron2, which is Facebook AI Research's (FAIR) software system that implements state-of-the-art object detection algorithms, including Faster R-CNN, Mask R-CNN, RetinaNet and Densepose [123–125]. Detectron2 is a newer version of Detectron and it is implemented in Pytorch with more modular design [123]. It has become the most widely used open source projects of FAIR because of its enhanced flexibility and extensibility [123].

5.3.2 The structure of different models

A typical CNN model is illustrated in Figure 5.6 which is used for recognizing handwritten digits. The CNNs usually consist of convolutional layers, pooling layers, and fully connected layers. The neurons in the first convolutional layer are only connected to their

corresponding receptive fields and the neuron's weights can be represented as a filter. Each filter will construct a feature map and all the feature maps will be combined together to form a convolutional layer. This architecture allows the network to focus on low-level features and then assemble them into higher-level features in the next hidden layer [110]. The pooling layer is added to reduce the computational load by reducing the image size. At the end of the convolutional layers, all the feature maps will be flattened and followed by several fully connected layers and the last layer outputs the prediction results.

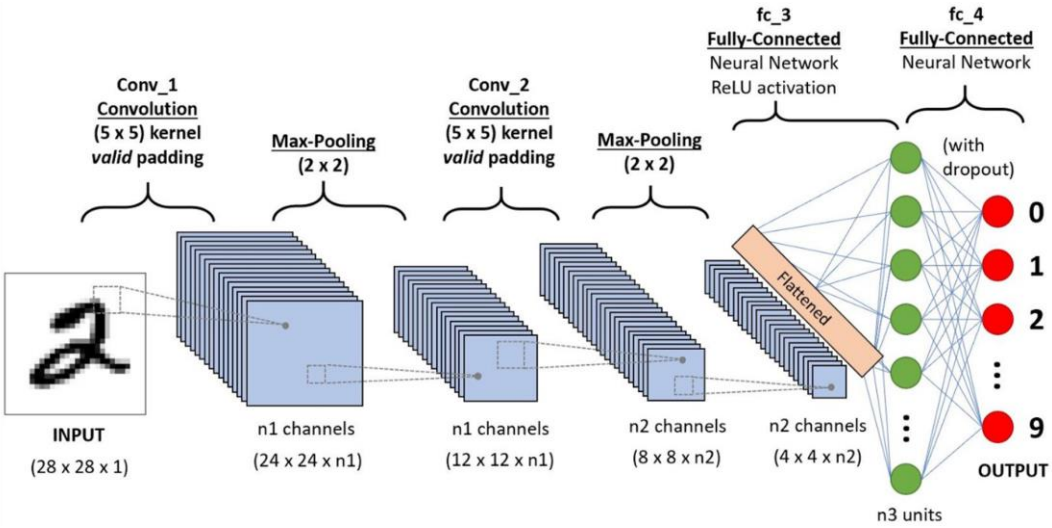

Figure 5.6. A CNN model to classify handwritten digits [120]

The YOLOv4 is a combination of a series of computer vision techniques which mainly consist of three parts, (1) Backbone: CSPDarknet53 [126]; (2) Neck: Spatial Pyramid Pooling (SPP) [127], Path Aggregation Network (PAN) [128]; (3) Head: YOLOv3 [129]. In the Backbone stage, the image is taken as input and goes through a CNN to extract features. YOLOv4 uses CSPDarknet53 as the Backbone, which is developed based on DenseNet [130]. CSPDarknet53 can separate the feature maps into two copies; one copy goes to dense block and the second copy can go directly to the next stage. This unedited version of the feature map can remove the computational bottlenecks [126,130]. Figure 5.7 (a) shows the structure of CSPDarknet53 [126]. The role of the Neck stage is to mix and combine feature maps from different stages of the Backbone [130]. The Neck consists of an SPP block and a PAN. The

SPP block can generate a fixed-length output with the most important features, and the PAN can achieve better propagation of layer information from bottom to top or top to bottom [130,131]. Figure 5.7 (b) shows the structure of SPP and Figure 5.7 (c) shows the structure of PAN [131,132]. The final Head stage will perform the last dense prediction, including the predicted bounding box's coordinates, the confidence score, and the classification label [131].

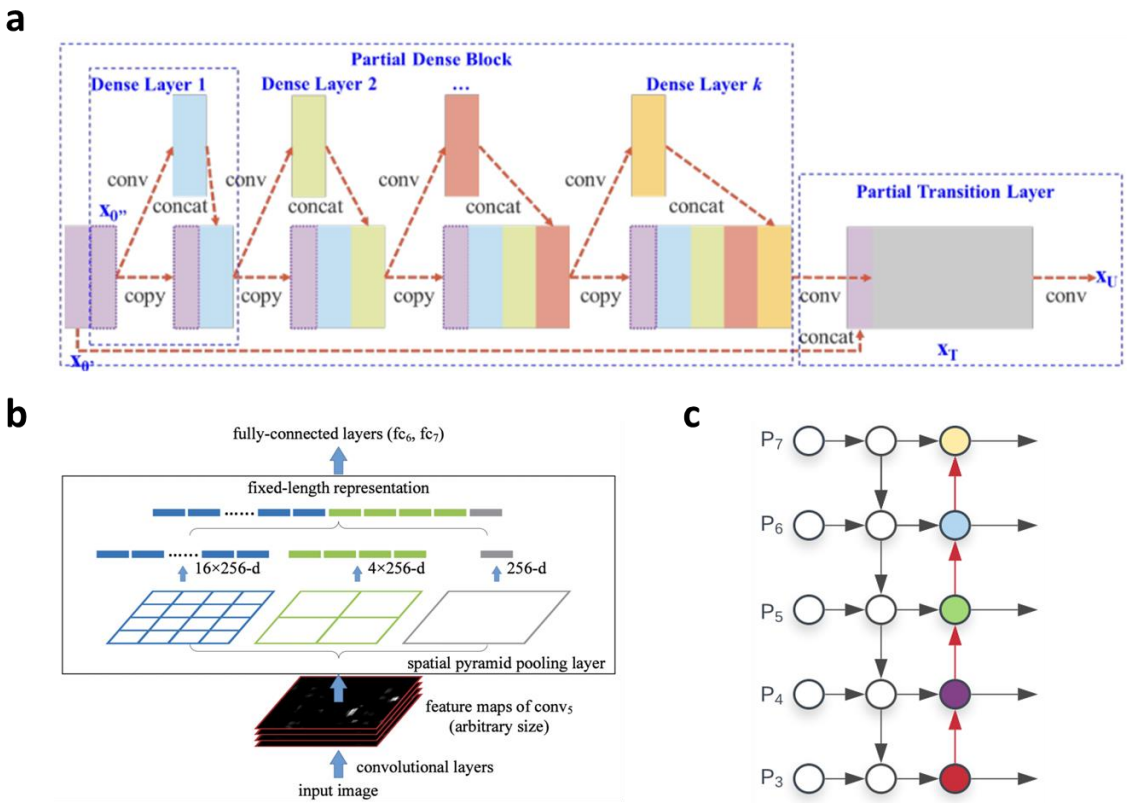

Figure 5.7. (a) The structure of CSPDarknet53 [126] (b)) The structure of SPP [131] (c) The structure of PAN [132]

Use Base R-CNN with Feature Pyramid Network (Base-RCNN-FPN) as an example, the structure of Detectron2 mainly includes three parts, Backbone Network, Region Proposal Network (RPN) and ROI Head (Box Head). The Backbone Network can extract multi-scale feature maps with various receptive fields from the input image; RPN can detect the object regions from the multi-scale feature maps, and by default, it will output a thousand proposed boxes with confidence score; at last, the Box Head can use the proposal boxes to crop the feature maps into different sized features, and through fully connected layers, it can find out

the box locations and the classification labels [133]. The above functions are achieved through different classes in each stage. For example, FPN and ResNet are the classes within the Backbone Network; the RPN stage includes StandardRPNHead and RPNOutput classes; and the ROI Head includes ROIPooler, FastRCNNConvFCHead, FastRCNNOutputLayers and FastRCNNOutputs classes [133]. Figure 5.8 shows the detailed structure of Detectron2 [133].

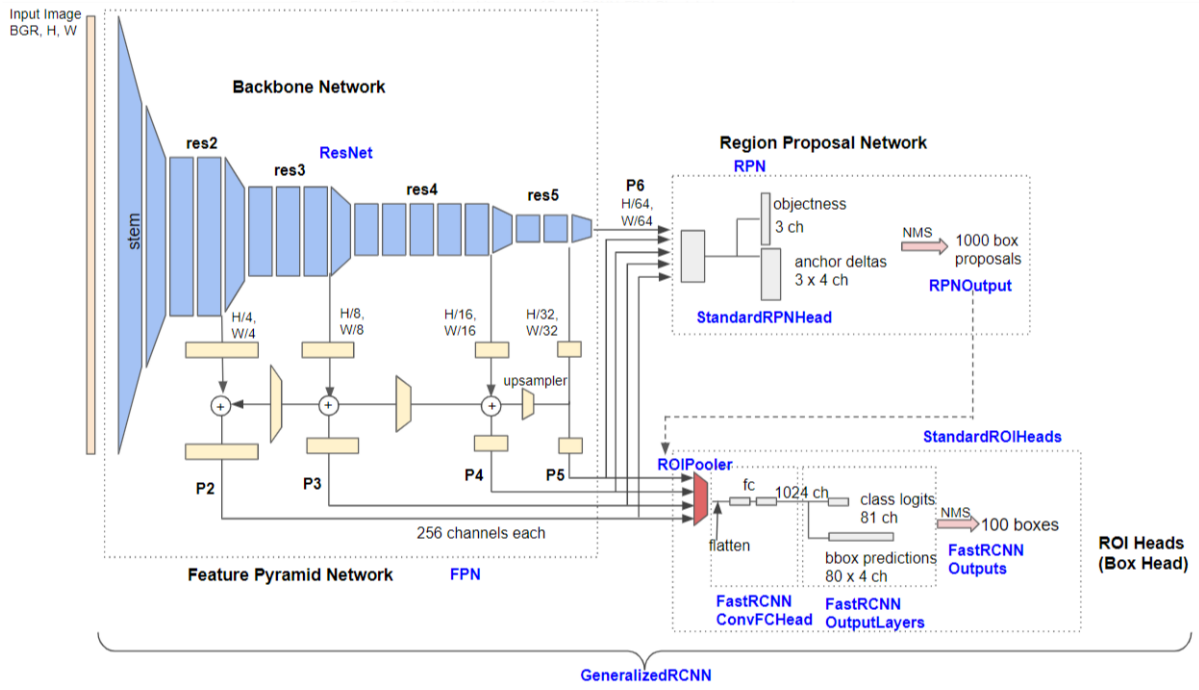

Figure 5.8. Detailed structure of Detectron2. (Blue labels are the class names) [133]

5.3.3 Image data preparation

Using CNNs for SLM defects classification and detection often involves three sub-tasks: 1) collecting images that include cracks and pores, 2) manually creating labels for a number of images, 3) train different CNN models using various techniques with the labeled images [134]. These tasks vary differently according to the different levels of complexity I attempted to achieve.

For level-one defects classification, a total of 200 images, with single defect in each image, were collected as screenshots from SLM printed Ni939 samples' SEM images, which

contain multiple cracks and pores. Therefore, there is only one defect need to be classified on each of these generated images. Two file folders are created (‘Cracks’ and ‘Pores’) to include the single defect images, and the folder names act as the defects’ class labels. Besides, 5 images in each category were used as validation data to test the model accuracy during the training process. A simple CNN model was trained using these images to distinguish between cracks and pores. Figure 5.9 shows some example images of the training data.

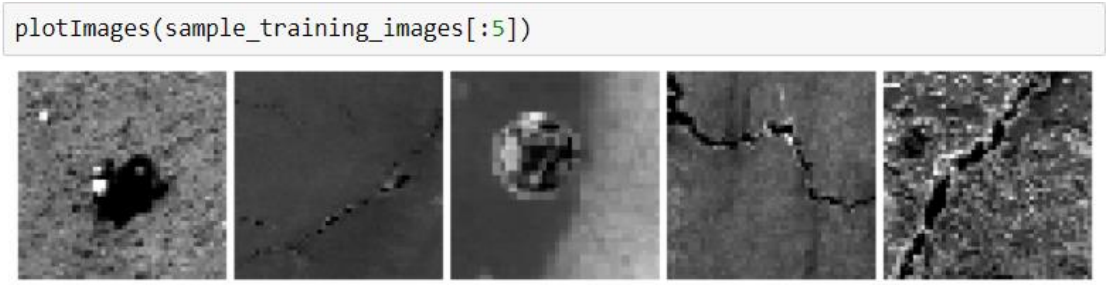

Figure 5.9 Examples of training data for the level-one CNN model

For target detection and image segmentation, I used the same group of images. A total of 11 SLM printed Ni939 sample images are collected from our daily research SEM image resources. Among the 11 images, nine images were used as training, and the rest two images were used as testing. According to the common practice, there are two image annotation softwares commonly used for labeling the data. The cracks and pores on these images were manually labeled using LabelImg, which can only draw the bounding box around the defects [135]. These labeled images were then used for training YOLOv4. The second software is Labelme, an image annotation tool that can outline the shape of the cracks and pores [136]. These labeled images were used for training Detectron2. Figure 5.10 (a)(b) shows an example labeled image using LabelImg and Labelme, respectively.

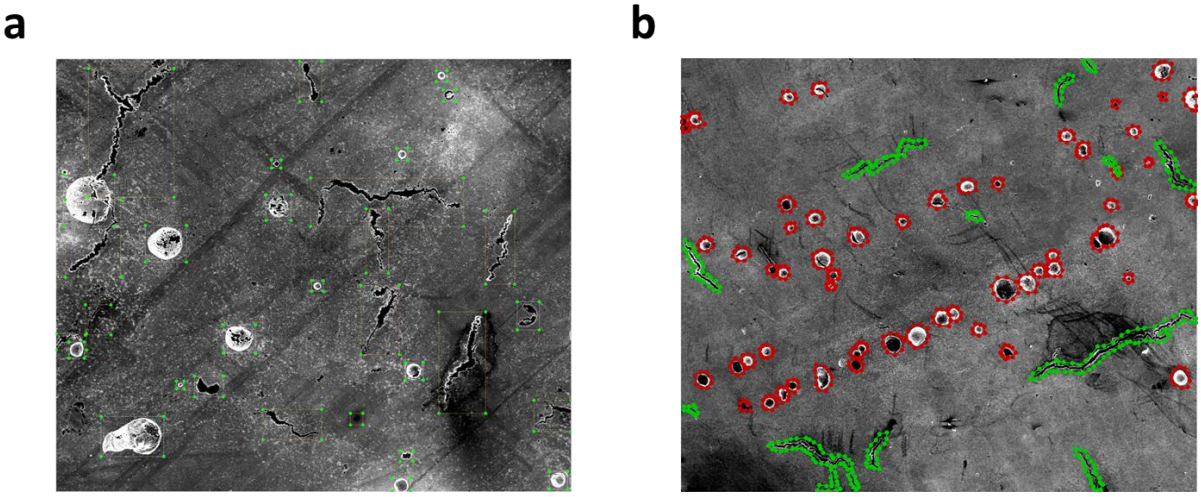

Figure 5.10 (a) An example of the labeled image using LabelImg for training YOLOv4 (b) An example of the labeled image using Labelme for training the Detectron2 model

5.3.4 Training process for different models

For training the level-one CNN model, the 200 single defect images are randomly shuffled and imported to Python at the same size of 50 x 50 pixels. Ten images with five images for each category were used as validation data to test the model's performance. The codes are generated using Python in Jupyter Notebook, and the ML packages include os, Numpy, Matplotlib, Tensorflow. All the images were imported to the CNN model with the label either 'Cracks' or 'Pores', and the model was built for binary classification. The CNN model has three convolutional layers, and each followed by a maxpooling layer. Two Dense layers are added at the end, and the activation functions are 'relu'. 'adam' is used as the optimizer and the loss function is 'BinaryCrossEntropy'. Table 5.3 shows a summary of the model. The model was trained for 50 epochs with training and validation accuracy tracked during the training process.

Table 5.3. The summary of CNN model

```
model.summary()
```

```
Model: "sequential_3"
_________________________________________________________________
Layer (type)                 Output Shape              Param #
=================================================================
conv2d_9 (Conv2D)            (None, 50, 50, 16)        448
_________________________________________________________________
max_pooling2d_9 (MaxPooling2 (None, 25, 25, 16)        0
_________________________________________________________________
conv2d_10 (Conv2D)           (None, 25, 25, 32)        4640
_________________________________________________________________
max_pooling2d_10 (MaxPooling (None, 12, 12, 32)        0
_________________________________________________________________
conv2d_11 (Conv2D)           (None, 12, 12, 64)        18496
_________________________________________________________________
max_pooling2d_11 (MaxPooling (None, 6, 6, 64)          0
_________________________________________________________________
flatten_3 (Flatten)          (None, 2304)              0
_________________________________________________________________
dense_6 (Dense)              (None, 512)               1180160
_________________________________________________________________
dense_7 (Dense)              (None, 1)                 513
=================================================================
Total params: 1,204,257
Trainable params: 1,204,257
Non-trainable params: 0
```

For training the YOLOv4 model, the darknet was cloned and rebuilt from AlexeyAB's repository to Google Colab [137,138]. As shown in Figure 5.10 (a), the labeled image contains the defects bounding box and defects' category information. The coordinates of the bounding box are included in a .txt file for each image. The yolov4-custom configuration file is adjusted based on two classes, and the training parameters include batch = 64, subdivision = 16, max_batches = 3600, steps = 2880, 3240, width = 416, height = 416. The classes are set to two for the three YOLO layers, and the filters = 21 in the three convolutional layers before the YOLO layers [139]. The pre-trained weights for the convolutional layers are loaded to the YOLOv4 network before training to achieve higher accuracy and shorten the training time. The model is trained for 3600 iterations, and the best weights are stored in Google Drive for later validation.

For training the Detectron2 model, a total of 828 pores and 301 cracks were manually labeled from the nine SEM images using Lableme software. As shown in Figure 5.10 (b), it

can be found that the shapes of the defects are outlined with a different color. These images contain instance and shape information compared with the YOLOv4 model. These detailed data can be exported to other software for further analysis and simulations, such as Finite Element Analysis (FEA) and crack propagation predictions under specific load conditions. The codes were generated using Python in Google Colab, and the ML packages include Pytroch, Detectron2, OpenCV, Numpy etc. Firstly, the labeled data were converted to coco format and registered as coco instances. Model Mask-RCNN-R50-FPN was chosen from the Detectron2 model zoo. The other training parameters include image_per_batch = 2, Base_learning_rate = 0.0025, training_iterations = 15000, batch_size_per_image = 512. The training curves were tracked using Tensorboard during the training process. After training, the rest two images were used to test the performance of the model.

5.3.5 Results and discussion

Figure 5.11 shows the 'accuracy' and 'loss' changes with epochs for the level-one CNN model. The training and validation accuracy almost reached 100%, and the loss got nearly to 0 only after ten epochs of training. In general, by just looking at the training curve, this indicates the model is overfitting, which means the model achieved high accuracy by just simply remembering each image category. This is a very common phenomenon, especially for the case with a small dataset [140]. Usually, the overfitted model cannot generalize well on the new data. As a result, six new test images that the model never saw during training were imported to the CNN model to test if it could classify the defects correctly. Figure 5.12 shows the classification results; as you can see, all the defects are classified correctly. Based on these six new images, the model performs perfectly and achieves very high accuracy. Based on the fact that all the training, validation and new test data are evenly distributed, it can be concluded that the model is not overfitting. The high accuracies are achieved mainly because this is a relatively simple dataset with obvious signals for each category. The pores are round shape and the cracks

are long narrow line shape, which can be easily distinguished. Another possible reason for this superior performance is that all the data is manually selected without any mistakes and confusion images, which can minimize the errors during the training and validation process.

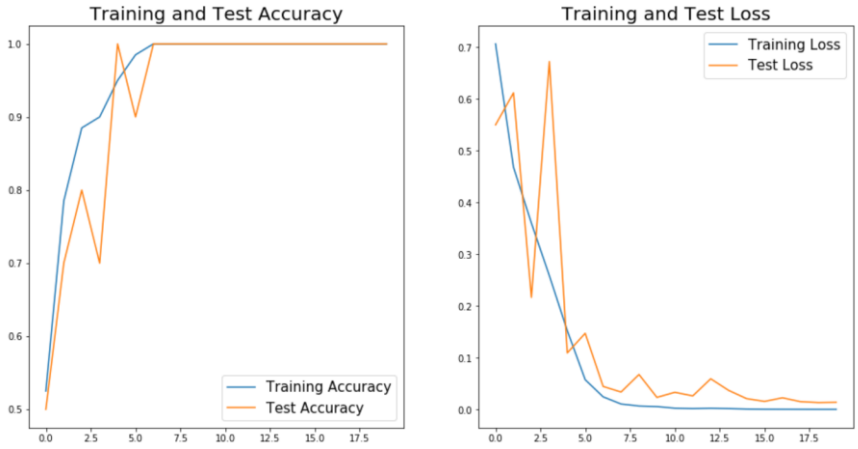

Figure 5.11. The accuracy and loss of training and validation for the level-one CNN model

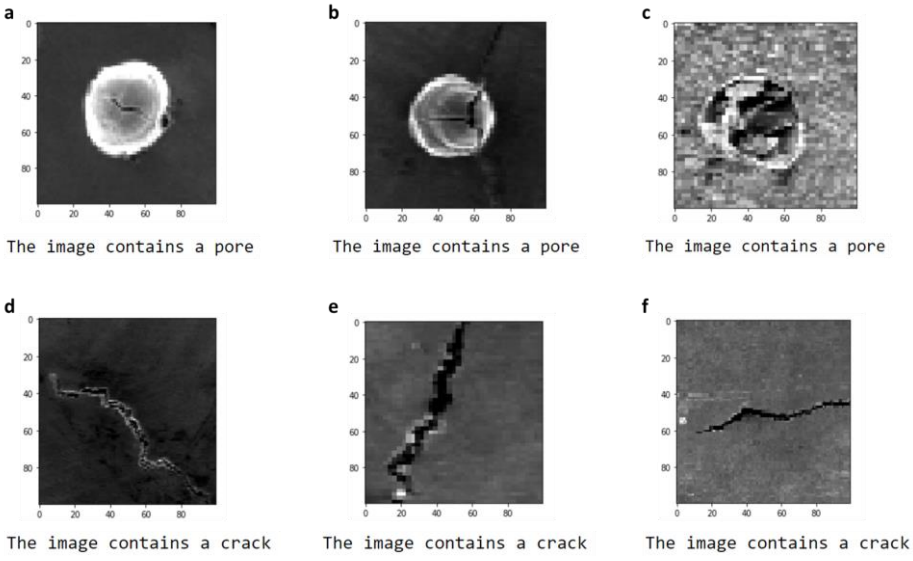

Figure 5.12. The test result for the level-one CNN model using six unknown data

The YOLOv4 model is trained using Google Colab Tesla P100-PCIE-16GB GPU for 3600 iterations, and the best weights are generated by the code and auto saved in Google drive. The final total loss reached around 16 and the Average Precision (AP) achieved about 50%. Figure 5.13 (a) shows the total loss and the AP curve recorded during the training process. It can be found that the total loss value indicated in the blue line falls below 20 after about 1200

iterations of training. After this, the loss value starts to bounce between 20 and 12 with tiny drops with the increase of training iterations. It indicates that the model already reached the local minimum. Even the training keeps going, and there will not have an obvious drop for the total loss value. However, the loss value is still very high compared with other applications which the loss value can drop under 2 [139,141]. After 1000 iterations of training, the AP value (red line) has been tracked for every 100 iterations of training with its value marked above the line. Between 1000 and 3600 iterations of training, the AP value does not have a noticeable increase. On the contrary, it dropped few times, indicating the model already has some degree of overfitting. As a result, the training process can have an early stop. However, around 50% AP value is deficient compared with some other applications [139,141–143]. The high loss and low AP value are most likely because of the complexity of the training data. (1) Some of the tiny features are ignored when labeling the image since there are too many, which is impossible to label all of them. (2) Some of the defects have an irregular shape that is different from most of the other defects. (3) There are some overlap defects, which can cause confusion to the model. Some examples of the above data are represented in Figure 13 (b). These complexities can make the model hardly fit all the data; therefore, the total loss and AP had no improvements after about 1000 training iterations. Besides, the relatively small training dataset size also contributes to the quick converge of the training process.

Before testing on new images, the configuration file is set to batch = 1, subdivision = 1, threshold = 0.3, to test on a single image. Figure 5.14 shows the test result. The bounding box, defects category, and the confidence score are marked on the image. It can be found that some defects are not recognized by this model. Some examples of the missed defects are marked with a red arrow in Figure 5.14 (a). By just visualizing the test result, the trained YOLOv4 model can generate acceptable results with about 90% recognition rate. The above testing result only covers one set of parameters in the configuration file; however, many

parameters may affect the final test results. Among them, the initial learning rate (LR) and scales are two important parameters. The LR needs to be high at the beginning of the training process with little knowledge of the features; however, the LR needs to be lowered with the increase of iterations. The scales are the factors to multiply LR after the specified step numbers [141]. Since the model has little improvements after about 1000 iterations of training, the max_batches is set to 1000 and the steps are set to 800, 900, which can save the training time. Table 5.4 shows the comparison of testing results with different LR and scales. Among them, the IoU stands for Intersection over Union, which computes the area of intersection over the union area of the ground truth bounding box and the predicted bounding box. It acts as the threshold to determine Ture Positive (TP) and False Positive (FP). When the model fails to detect an object which is present in the ground truth image, it will be classified as False Negative (FN). Below are the equations for calculating Average Precision (AP) and Recall values [117].

$$AP = \frac{1}{N}\sum\frac{TP}{TP+FP} \quad (3)$$

$$Recall = \frac{1}{N}\sum\frac{TP}{TP+FN} \quad (4)$$

Basically, the AP value describes the accuracy of the predicted objects and the Recall value indicates the completeness of the predicted results. Both of these two values are the higher the better. As a result, the No. 6 parameters achieved the best results. Figure 5.15 shows a comparison of the testing results on a same image using (a) No. 6 (b) No. 5 and (c) No. 1 parameters. In Figure 5.15, (b) has more detections, however it includes a lot FP detections, which drops the AP to only 73%. Figure 5.15 (c) has less detections compared with (a), but it cannot cover all the defects included in the ground truth image. Therefore, the Recall value for No. 1 is only 0.35.

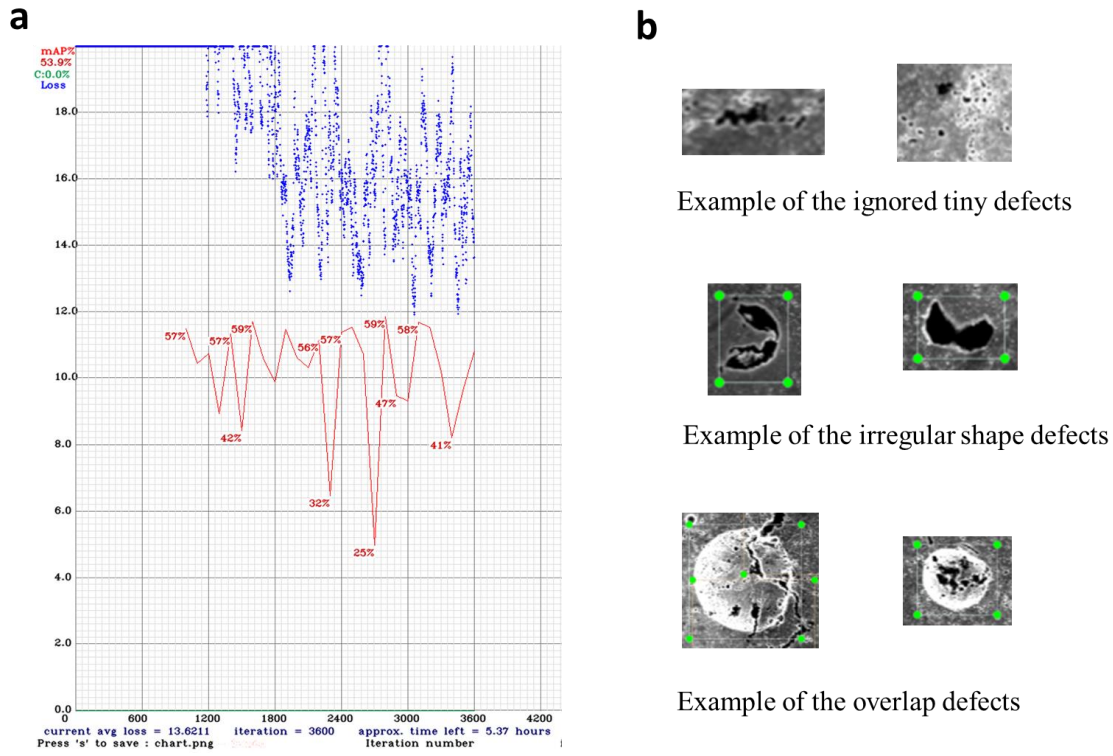

Figure 5.13. (a) The total loss and AP curve of YOLOv4 training process (The X-axis is the training iterations, Y-axis is the total loss, the blue curve is the total loss and the red curve is the AP) (b) Examples of the data complexity

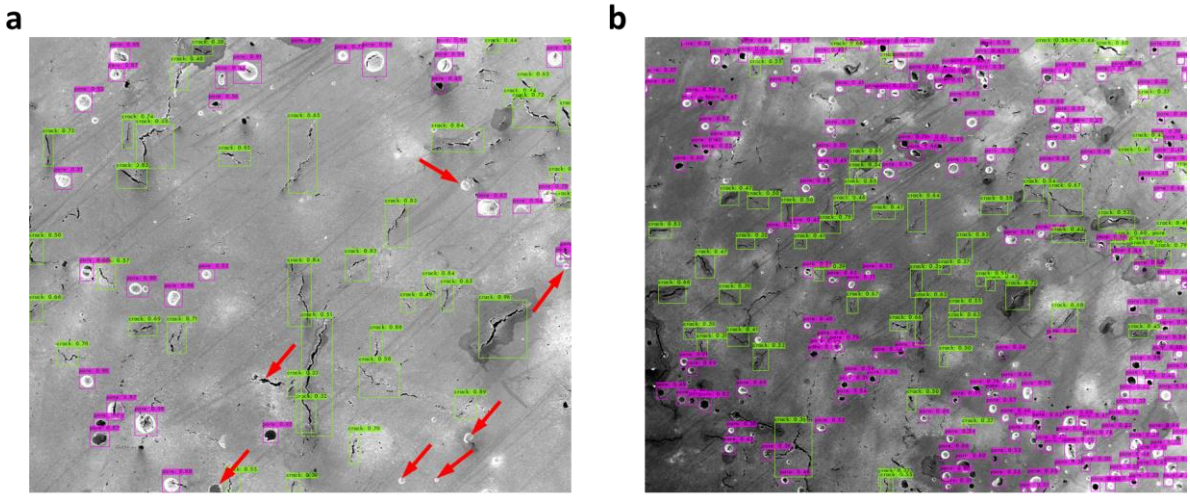

Figure 5.14. The test result of the YOLOv4 model with the best weights and threshold of 0.3 (the red arrows indicate some of the missed defects)

Table 5.4. The comparison of testing result with different LR and scales

No.	LR	Scales	AP	Recall	TP	FP	FN	average IoU
1		0.1, 0.1	77%	0.35	150	46	274	54.16%
2	0.001	0.2, 0.2	79%	0.49	208	56	216	54.44%
3		0.3, 0.3	75%	0.49	207	69	217	52.19%
4		0.1, 0.1	79%	0.47	199	52	225	56.34%
5	0.0005	0.2, 0.2	73%	0.48	205	77	219	49.48%
6		**0.3, 0.3**	**80%**	**0.5**	**210**	**51**	**214**	**57.19%**

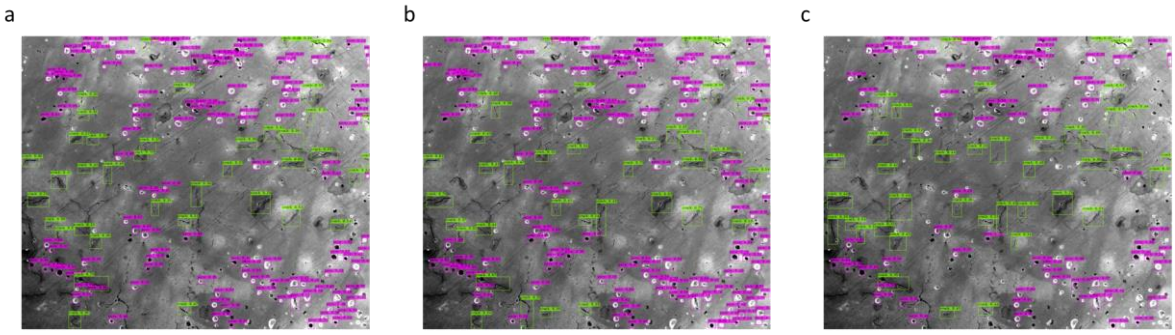

Figure 5.15. The testing results on the same image using trained YOLOv4 model with (a) No. 6 parameters (b) No. 5 parameters (c) No. 1 parameters

The Detectron2 model is trained using Google Colab Tesla P100-PCIE-16GB GPU for 15000 iterations. The total loss value is tracked using Tensorboard, and the curve is shown in Figure 5.16. It can be seen that the total loss value drops with the increase of training iterations and finally reach about 0.2. However, the total loss number cannot indicate model performance on the new data since it may have overfitting. Therefore, testing the trained model on the new images is necessary. Before testing, the testing threshold is set to 0.3, and the detections_per_image is set to 1000. It is used to cover a large number of defects in the testing images. Figure 5.17 shows the testing results using the trained Detectron2 model. The image used for testing is the same as testing the YOLOv4 model. However, besides the bounding box, the result outlines the defects' shape, which is an extra information compared with YOLOv4. Similarly, there are also a few missed defects, which are marked in the red arrows in Figure 5.17 (a). By just visualizing the testing results using the Detectron2 model, the trained model

can identify more than 90% of the defects. However, for some more complicated images with much higher defects density, the testing result of the Detectron2 model is not as good as the YOLOv4 model. By comparing Figure 5.14 (b) and Fig 5.17 (b) (both of these two images are set the test threshold to 0.3), it can be found that the Detectron2 model missed more defects compared with the YOLOv4 model. Nevertheless, the Detectron2 model only takes about 3 hours to train 15000 iterations, and the YOLOv4 model takes more than 9 hours to train 3600 iterations using the same GPU. Therefore, the Detectron2 model is more efficient than the YOLOv4 model based on the training process.

Detectron2 Model Zoo has different baseline models, which are combinations of different Backbones and Train Schedules [144]. Three models are selected to compare the performance of different baselines, and all the evaluations are performed using the same images as used in the previous testing. The results are shown in Table 5.5. Among them, the mAP value is the average AP for IoU from 0.5 to 0.95 with a step size of 0.05. AP50 is the AP with IoU=0.5, and AP75 is the AP when IoU=0.75. AR10 is the average Recall value given 10 detections per image. Similarly, AR100 and AR 1000 are the average Recall value when the maximum detection per image are 100 and 1000 respectively. It can be found in Table 5.5 that for all three models, the AP and AR values only have minor various with the increase of training iterations from 5000 to 10000. It indicates that all the models will converge quickly because of the small training dataset. When the IoU threshold becomes larger, the AP value will drop dramatically, so that the mAP value is low compared with YOLOv4. The AR value reaches the highest when the maximum detection per image reaches 1000. However, when the number is small, the AR value decreases significantly. Based on the mAP and AR1000 value, No.3 model with 1000 iteration training has the best testing result and the No. 1 model with 5000 iteration training is the worst among Table 5.5. Figure 5.18 (a)(b) shows a comparison of

the testing result images between the best and worst model. By just visualizing, it can be obviously find out that No. 1 model misses more defects than No. 3 model.

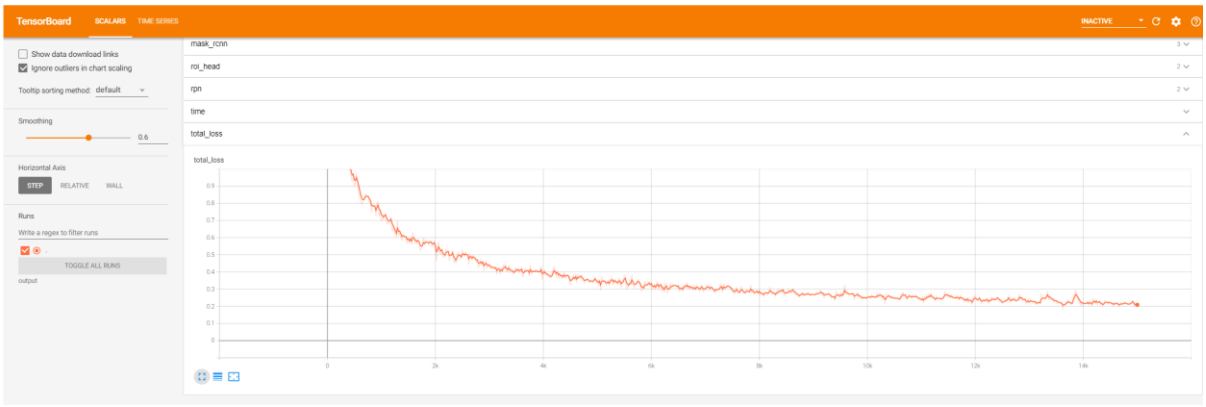

Figure 5.16. The total loss curve of Detectron2 during the training process

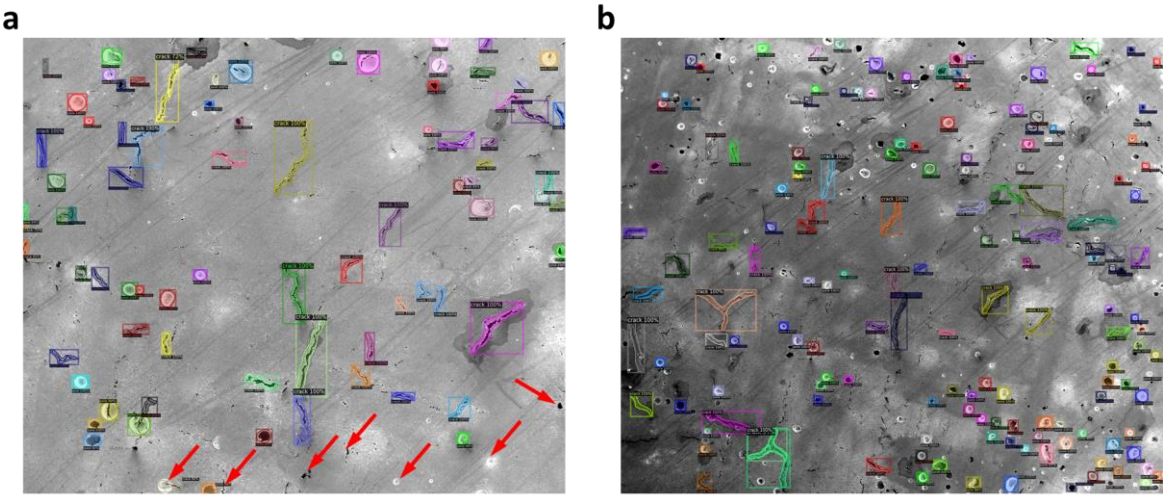

Figure 5.17. The test result of the Detectron2 model with the threshold of 0.3 (the red arrow indicates some of the missed defects)

Table 5.5. The comparison of testing results with different models and iteration numbers

No.	Model	Iterations	mAP	AP50	AP75	AR10	AR100	AR1000
1	X101-FPN 3x	5000	0.178	0.394	0.134	0.06	0.217	0.234
		10000	0.178	0.384	0.119	0.061	0.223	0.237
2	R50-FPN 3x	5000	0.23	0.505	0.164	0.058	0.26	0.283
		10000	0.231	0.524	0.17	0.054	0.272	0.288
3	R101-DC5 3x	5000	0.237	0.59	0.133	0.045	0.27	0.324
		10000	**0.237**	**0.569**	**0.155**	**0.042**	**0.271**	**0.33**

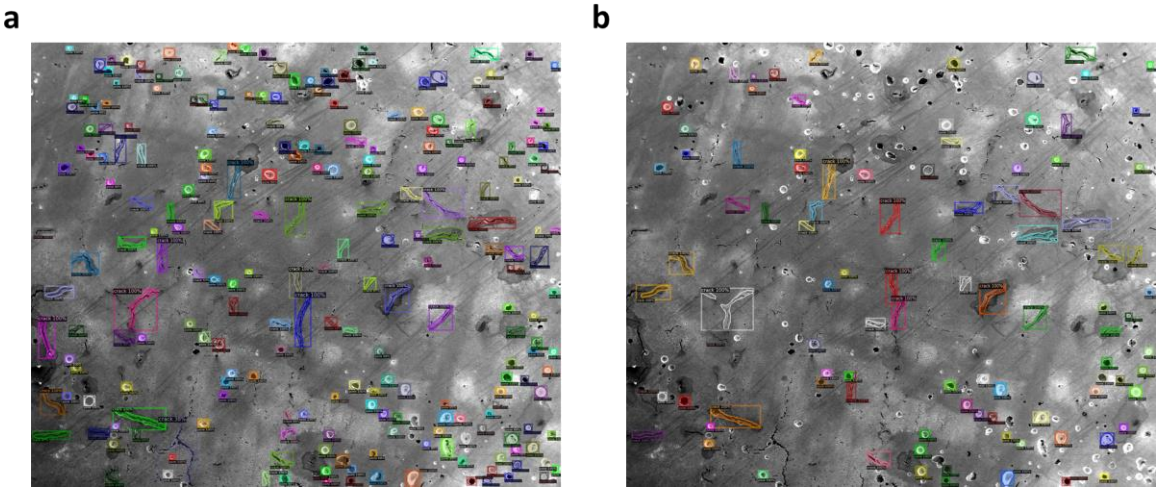

Figure 5.18. The testing results on the same image using (a) No. 3 model (b) No. 1 model

5.4 Defects detection on videos

In order to achieve in-situ monitoring and modification of the 3D printing process, the defects detection on videos needs to be tested to approve its feasibility. Based on the previous section, the Detectron2 R101_DC5_3x model has the highest accuracy, and it can provide the most information for potential analysis. Therefore, this model is selected for the detection test.

5.4.1 Video preparation and model training

About 1800 SLM Ni939 sample cross-section CT scan images are accumulated using 3D x-ray microscopy (Zeiss XRM 620 Versa, US). Because of the size limitation, a sequence of 100 images were imported to ImageJ software to generate a 14 seconds video with a frame rate of 7 fps. This video was then used for testing the trained Detectron2 model.

Ten different images were chosen from the above CT scan images to generate the training data. The training data were manually labeled with cracks and pores with the same process as section 5.3.3 using Labelme software. Detectron2 R101_DC5_3x model is trained using Google Colab for 5000 iterations with a learning rate of 0.0025. All other parameters are the same as in section 5.3.4. Before testing on the video, the weight path in the configuration file is changed to the trained model's final weight; the test threshold is set to 0.3; the detection per image is increased to 1000 per image.

5.4.2 Video testing result

A comparison of the original video and the output video after defects detection using the trained Detectron2 model is shown in Figure 5.19. For the convenience of inserting the video, both the original and the detection videos are transferred from MP4 format to GIF format by keeping the same resolution and the picture ratio. It can be found that the trained Detectron2 model can detect almost all the pores and cracks which exist in the original video; furthermore, the detections also present the defects category, defect location, and the defects shape information in a very short period of time for each frame (based on the evaluator function that included in the Detectron2, it only takes about 0.22 seconds to generate the above information for each frame). This information can be beneficial for simulating the material crack and fatigue predictions under certain load conditions. Based on the simulation results, the 3D printing machine can modify or eliminate the defects by changing different scan parameters or scan strategies. However, due to the limitation of the current facilities and resources, further work needs to be done in the future.

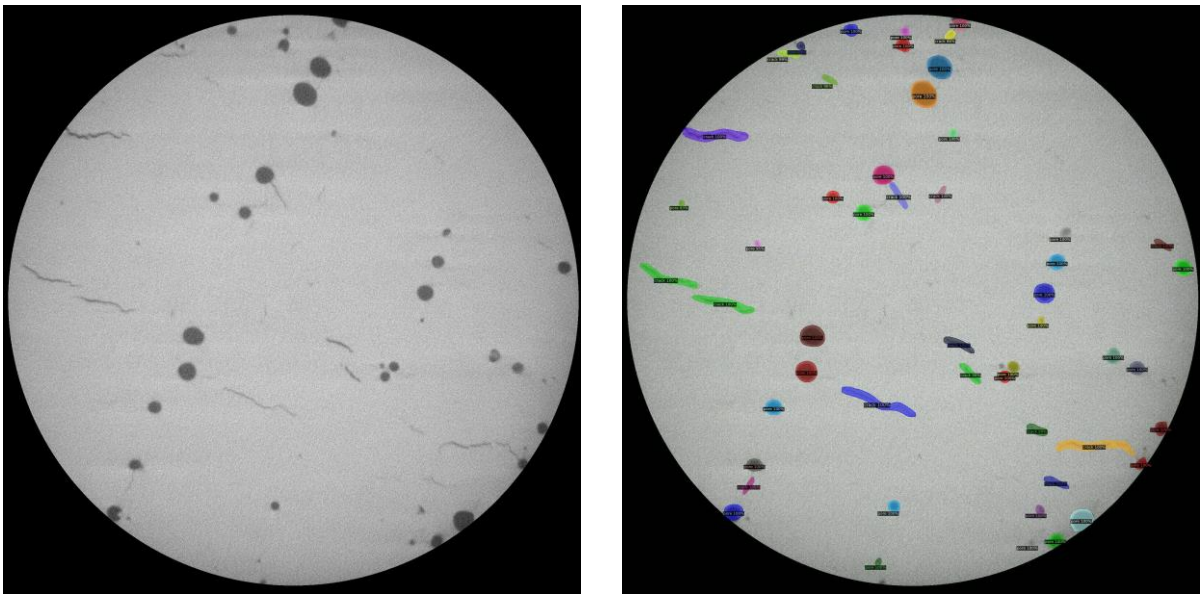

Figure 5.19. The comparison of the original video (left) and the output video (right) of the defect's detection using trained Detectron2 model. (Both of the videos are in GIF format.)

5.5 Conclusions

- A simple DNN model is created to predict the APBE based on the limited training data. Because of lacking low-temperature data, some of the testing data at lower temperatures cannot fit well with the trained DNN model. However, the DL model still achieves the best performance compared with Random Forest Regressor model and K Neighbors Regressor model.
- Three different levels of material image analysis complexities are achieved in this study; the defects classification, the defects detection, and the defects image segmentation are successfully performed using a simple CNN model, YOLOv4 and Detectron2, respectively. By tuning some parameters in each application, the CNN model can accurately classify cracks and pores. The other two models can identify more than 90% of the defects in the testing images.
- Defects detection is successfully applied on video by using a sequence of CT scan images. The trained Detectron2 model can identify almost all the pores and cracks that exist in the original video. It lays a foundation for the future in-situ correction of the 3D printing process.

Overall, the deep learning models can be successfully applied to materials science related regression and image classification tasks in this chapter. It demonstrates that ML can be a new direction for some materials science research to become more efficient and economical. However, the functions of these tasks performed in this chapter are still very limited due to data shortage. Compared with some of DL applications' main field, such as self-driving cars, natural language processing, etc., usually millions of data are needed. As a result, building a database or collecting more data closely related to the research purpose are the main obstacles for applying ML in the materials science field.

Appendix. Reprint Permissions

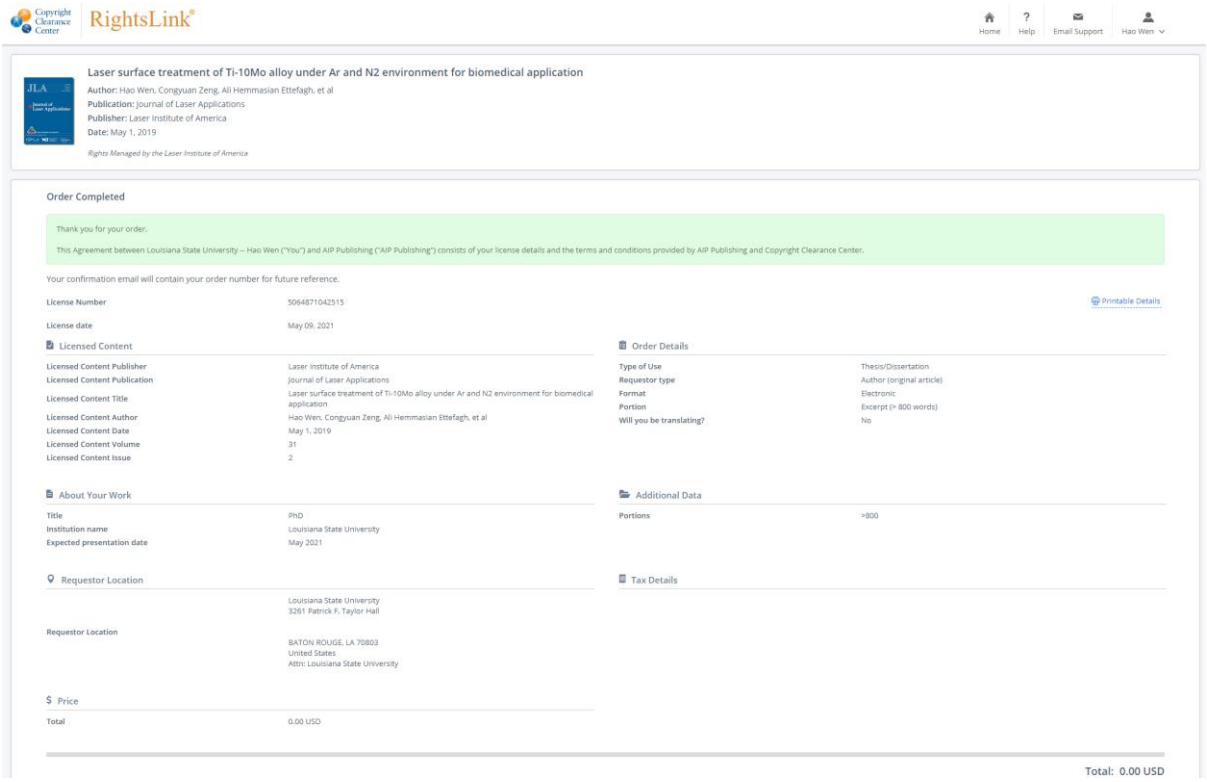

Laser surface treatment of Ti-10Mo alloy under Ar and N2 environment for biomedical application

Author: Hao Wen, Congyuan Zeng, Ali Hemmasian Ettefagh, et al
Publication: Journal of Laser Applications
Publisher: Laser Institute of America
Date: May 1, 2019

Rights Managed by the Laser Institute of America

Order Completed

Thank you for your order.

This Agreement between Louisiana State University -- Hao Wen ("You") and AIP Publishing ("AIP Publishing") consists of your license details and the terms and conditions provided by AIP Publishing and Copyright Clearance Center.

Your confirmation email will contain your order number for future reference.

License Number	5064871042515
License date	May 09, 2021

Printable Details

Licensed Content

Licensed Content Publisher	Laser Institute of America
Licensed Content Publication	Journal of Laser Applications
Licensed Content Title	Laser surface treatment of Ti-10Mo alloy under Ar and N2 environment for biomedical application
Licensed Content Author	Hao Wen, Congyuan Zeng, Ali Hemmasian Ettefagh, et al
Licensed Content Date	May 1, 2019
Licensed Content Volume	31
Licensed Content Issue	2

Order Details

Type of Use	Thesis/Dissertation
Requestor type	Author (original article)
Format	Electronic
Portion	Excerpt (> 800 words)
Will you be translating?	No

About Your Work

Title	PhD
Institution name	Louisiana State University
Expected presentation date	May 2021

Additional Data

Portions	>800

Requestor Location

Louisiana State University
3261 Patrick F. Taylor Hall

Requestor Location

BATON ROUGE, LA 70803
United States
Attn: Louisiana State University

Tax Details

Price

Total	0.00 USD

Total: 0.00 USD

Terms and Conditions

Laser Institute of America -- Terms and Conditions: Permissions Uses

Laser Institute of America ("LIA") hereby grants to you the non-exclusive right and license to use and/or distribute the Material according to the use specified in your order, on a one-time basis, for the specified term, with a maximum distribution equal to the number that you have ordered. Any links or other content accompanying the Material are not the subject of this license.

1. You agree to include the following copyright and permission notice with the reproduction of the Material:"Reprinted with permission from [FULL CITATION]. Copyright [PUBLICATION YEAR], Laser Institute of America." For an article, the copyright and permission notice must be printed on the first page of the article or book chapter. For photographs, covers, or tables, the copyright and permission notice may appear with the Material, in a footnote, or in the reference list.
2. If you have licensed reuse of a figure, photograph, cover, or table, it is your responsibility to ensure that the material is original to LIA and does not contain the copyright of another entity, and that the copyright notice of the figure, photograph, cover, or table does not indicate that it was reprinted by LIA, with permission, from another source. Under no circumstances does LIA, purport or intend to grant permission to reuse material to which it does not hold copyright.
3. You may not alter or modify the Material in any manner. You may translate the Material into another language only if you have licensed translation rights. You may not use the Material for promotional purposes. LIA reserves all rights not specifically granted herein.
4. The foregoing license shall not take effect unless and until LIA or its agent, Copyright Clearance Center, receives the Payment in accordance with Copyright Clearance Center Billing and Payment Terms and Conditions, which are incorporated herein by reference.
5. LIA or the Copyright Clearance Center may, within two business days of granting this license, revoke the license for any reason whatsoever, with a full refund payable to you. Should you violate the terms of this license at any time, LIA, Laser Institute of America, or Copyright Clearance Center may revoke the license with no refund to you. Notice of such revocation will be made using the contact information provided by you. Failure to receive such notice will not nullify the revocation.
6. LIA makes no representations or warranties with respect to the Material. You agree to indemnify and hold harmless LIA, Laser Institute of America, and their officers, directors, employees or agents from and against any and all claims arising out of your use of the Material other than as specifically authorized herein.
7. The permission granted herein is personal to you and is not transferable or assignable without the prior written permission of LIA. This license may not be amended except in a writing signed by the party to be charged.
8. If purchase orders, acknowledgments or check endorsements are issued on any forms containing terms and conditions which are inconsistent with these provisions, such inconsistent terms and conditions shall be of no force and effect. This document, including the CCC Billing and Payment Terms and Conditions, shall be the entire agreement between the parties relating to the subject matter hereof.

This Agreement shall be governed by and construed in accordance with the laws of the State of New York. Both parties hereby submit to the jurisdiction of the courts of New York County for purposes of resolving any disputes that may arise hereunder.

Questions? customercare@copyright.com or +1-855-239-3415 (toll free in the US) or +1-978-646-2777.

A.1. Reprint permission from the publisher for Chapter 3.

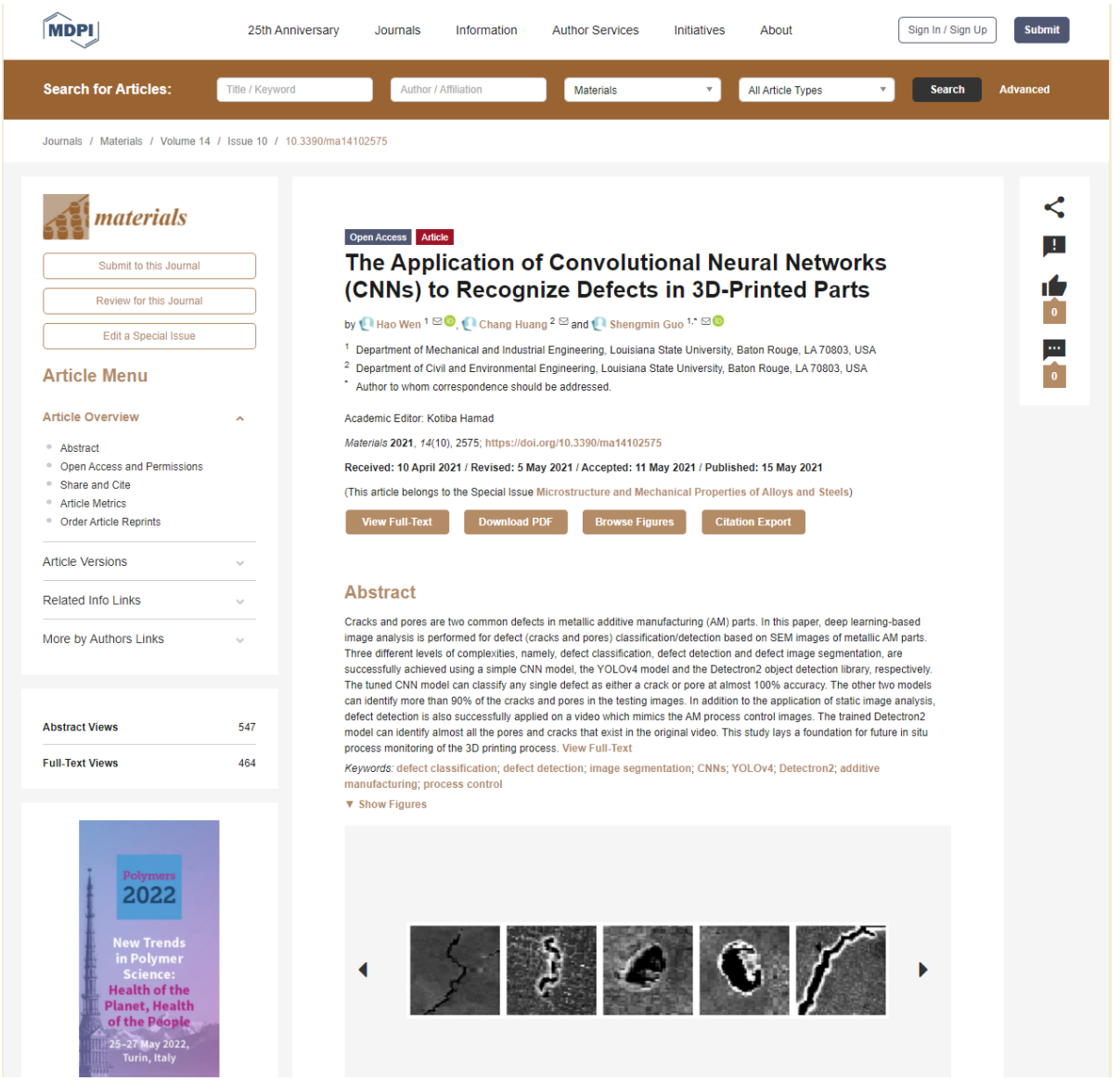

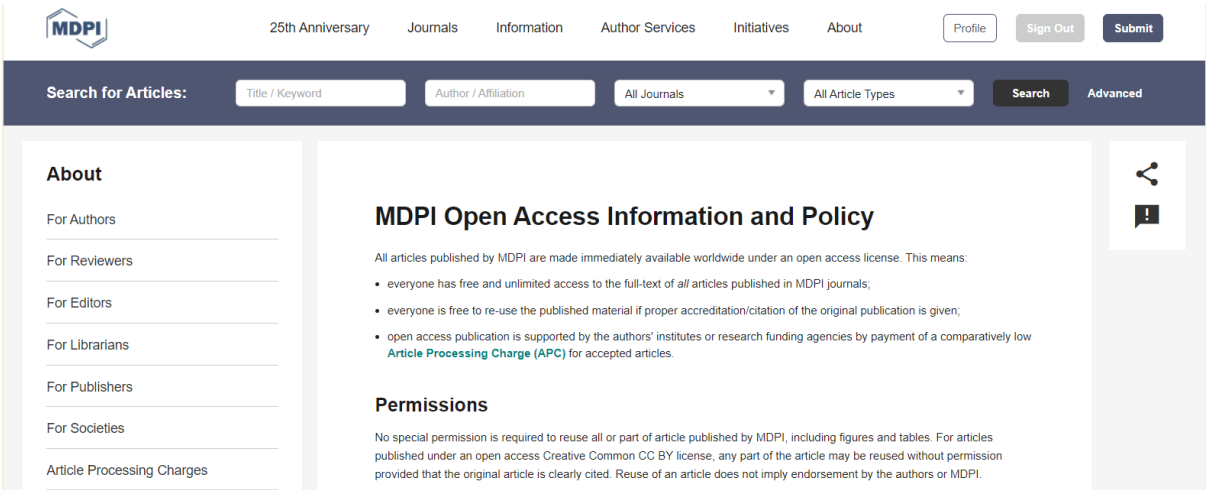

A.2. Reprint permission from the publisher for Section 5.3 of Chapter 5.

References

[1] Kruth, J. P., Levy, G., Klocke, F., and Childs, T. H. C., 2007, "Consolidation Phenomena in Laser and Powder-Bed Based Layered Manufacturing," CIRP Ann. - Manuf. Technol., 56(2), pp. 730–759.

[2] Attar, H., Calin, M., Zhang, L. C., Scudino, S., and Eckert, J., 2014, "Manufacture by Selective Laser Melting and Mechanical Behavior of Commercially Pure Titanium," Mater. Sci. Eng. A, 593, pp. 170–177.

[3] Craeghs, T., Thijs, L., Verhaeghe, F., Kruth, J.-P., and Humbeeck, J. Van, 2010, "A Study of the Microstructural Evolution during Selective Laser Melting of Ti–6Al–4V," Acta Mater. DOI:10.1016/j.actamat.2010.02.004.

[4] Melting, S. L., "Optimized for Selective Laser Melting SLM Solutions ' Material Competence Selective Laser Melting Pioneers."

[5] Mazumder, J., *Laser Assisted Surface Coatings*.

[6] Agarwal, A., and Dahotre, N. B., *Laser Surface Engineering of Steel for Hard Refractory Ceramic Composite Coating*.

[7] Xiao, R., and Zhang, X., 2014, "Problems and Issues in Laser Beam Welding of Aluminum-Lithium Alloys," J. Manuf. Process., 16(2), pp. 166–175.

[8] Olsson, R., Powell, J., Palmquist, A., Brånemark, R., Frostevarg, J., and Kaplan, A. F. H., 2018, "Production of Osseointegrating (Bone Bonding) Surfaces on Titanium Screws by Laser Melt Disruption," J. Laser Appl. DOI:10.2351/1.5078502.

[9] Oliveira, N. T. C., Guastaldi, F. P. S., Perrotti, V., Hochuli-Vieira, E., Guastaldi, A. C., Piattelli, A., and Iezzi, G., 2013, "Biomedical Ti-Mo Alloys with Surface Machined and Modified by Laser Beam: Biomechanical, Histological, and Histometric Analysis in Rabbits," Clin. Implant Dent. Relat. Res., 15(3), pp. 427–437.

[10] Kanagarajah, P., Brenne, F., Niendorf, T., and Maier, H. J., 2013, "Inconel 939 Processed by Selective Laser Melting: Effect of Microstructure and Temperature on the Mechanical Properties under Static and Cyclic Loading," Mater. Sci. Eng. A, 588, pp. 188–195.

[11] Sjöberg, G., Imamovic, D., Gabel, J., Caballero, O., Brooks, J. W., Ferté, J. P., and Lugan, A., 2004, "Evaluation of the IN 939 Alloy for Large Aircraft Engine Structures," Proc. Int. Symp. Superalloys, pp. 441–450 DOI:10.7449/2004/superalloys_2004_441_450.

[12] Schnell, A., Hoebel, M., Samuleson, J., Power Arabia FZE, A., Ali Freezone, J., and Power Switzerland, A., 2011, "A Study of the Weldability of Gamma Prime Hardened Superalloys" DOI:10.4028/www.scientific.net/AMR.278.434.

[13] Han, Q., Gu, Y., Setchi, R., Lacan, F., Johnston, R., Evans, S. L., and Yang, S., 2019, "Additive Manufacturing of High-Strength Crack-Free Ni-Based Hastelloy X Superalloy," Addit. Manuf., 30.

[14] Shaw, S. W. K., *RESPONSE OF IN-939 TO PROCESS VARIATIONS*.

[15] Hughes, W. P., Berry, T. F., and Yount, R. E., 1968, *A Study of the Strain-Age Crack Sensitivity of RENE' 41*.

[16] Chen, F., Deng, P., Wan, J., Zhang, D., Vasilakos, A. V., and Rong, X., 2015, "Data Mining for the Internet of Things: Literature Review and Challenges," Int. J. Distrib.

Sens. Networks, 2015.

[17] Gao, J., Jiang, Q., Zhou, B., and Chen, D., 2019, "Convolutional Neural Networks for Computer-Aided Detection or Diagnosis in Medical Image Analysis: An Overview," Math. Biosci. Eng., 16(6), pp. 6536–6561.

[18] Silver, D., Schrittwieser, J., Simonyan, K., Antonoglou, I., Huang, A., Guez, A., Hubert, T., Baker, L., Lai, M., Bolton, A., Chen, Y., Lillicrap, T., Hui, F., Sifre, L., Van Den Driessche, G., Graepel, T., and Demis, H., *Mastering the Game of Go without Human Knowledge*.

[19] In, H. P., Kim, Y.-G., Lee, T., Moon, C.-J., Jung, Y., and Kim, I., 2004, *A Security Risk Analysis Model for Information Systems*.

[20] Wei, J., Chu, X., Sun, X., Xu, K., Deng, H., Chen, J., Wei, Z., and Lei, M., 2019, "Machine Learning in Materials Science," InfoMat, 1(3), pp. 338–358.

[21] Schütt, K. T., Arbabzadah, F., Chmiela, S., Müller, K. R., and Tkatchenko, A., 2017, "Quantum-Chemical Insights from Deep Tensor Neural Networks," Nat. Commun., 8.

[22] Schütt, K. T., Sauceda, H. E., Kindermans, P.-J., Tkatchenko, A., and Müller, K.-R., 2017, "SchNet - a Deep Learning Architecture for Molecules and Materials" DOI:10.1063/1.5019779.

[23] Cecen, A., Dai, H., Yabansu, Y. C., Kalidindi, S. R., and Song, L., 2018, "Material Structure-Property Linkages Using Three-Dimensional Convolutional Neural Networks," Acta Mater., 146, pp. 76–84.

[24] Jha, D., Ward, L., Paul, A., Liao, W. keng, Choudhary, A., Wolverton, C., and Agrawal, A., 2018, "ElemNet: Deep Learning the Chemistry of Materials From Only Elemental Composition," Sci. Rep., 8(1).

[25] Huszarik, S., 2014, *YLR-SERIES USER GUIDE*.

[26] *Scan Heads Installation and Operation Manual Scan Heads Installation and Operation Manual Scan Heads Installation and Operation Manual*.

[27] "Optical Transmission Curve," BOROFLOAT®.

[28] Hemmasian Ettefagh, A., Wen, H., Chaichi, A., Islam, M. I., Lu, F., Gartia, M., and Guo, S., 2020, "Laser Surface Modifications of Fe-14Cr Ferritic Alloy for Improved Corrosion Performance," Surf. Coatings Technol., 381.

[29] Ettefagh, A. H., Wen, H., Lu, F., and Guo, S., 2018, "Phase Evolution and Corrosion Performance of Laser Processed Oxide Dispersion Strengthened Ferritic Alloys," *ASME International Mechanical Engineering Congress and Exposition, Proceedings (IMECE)*, American Society of Mechanical Engineers (ASME).

[30] Zeng, C., Wen, H., Zhang, B., Sprunger, P. T., and Guo, S. M., 2020, "Diffusion of Oxygen and Nitrogen into Titanium under Laser Irradiation in Air," Appl. Surf. Sci., 505.

[31] Zeng, C., Wen, H., Hemmasian Ettefagh, A., Zhang, B., Gao, J., Haghshenas, A., Raush, J. R., and Guo, S. M., 2020, "Laser Nitriding of Titanium Surfaces for Biomedical Applications," Surf. Coatings Technol., 385.

[32] "CIMMSymposium2019 Seetala-Yang_2019_5_28."

[33] Cardoso, F. F., Ferrandini, P. L., Lopes, E. S. N., Cremasco, A., and Caram, R., 2014, "Ti-Mo Alloys Employed as Biomaterials: Effects of Composition and Aging Heat Treatment on Microstructure and Mechanical Behavior," J. Mech. Behav. Biomed.

Mater. DOI:10.1016/j.jmbbm.2013.11.021.

[34] Oliveira, N. T. C., Aleixo, G., Caram, R., and Guastaldi, A. C., 2007, "Development of Ti-Mo Alloys for Biomedical Applications: Microstructure and Electrochemical Characterization," Mater. Sci. Eng. A DOI:10.1016/j.msea.2006.11.061.

[35] Xie, F., He, X., Lv, Y., Wu, M., He, X., and Qu, X., 2015, "Selective Laser Sintered Porous Ti-(4-10)Mo Alloys for Biomedical Applications: Structural Characteristics, Mechanical Properties and Corrosion Behaviour," Corros. Sci. DOI:10.1016/j.corsci.2015.03.005.

[36] Xie, F. X., He, X. B., Cao, S. L., Lu, X., and Qu, X. H., 2013, "Structural Characterization and Electrochemical Behavior of a Laser-Sintered Porous Ti-10Mo Alloy," Corros. Sci. DOI:10.1016/j.corsci.2012.10.036.

[37] Zhuravleva, K., Bönisch, M., Prashanth, K. G., Hempel, U., Helth, A., Gemming, T., Calin, M., Scudino, S., Schultz, L., Eckert, J., and Gebert, A., 2013, "Production of Porous β-Type Ti-40Nb Alloy for Biomedical Applications: Comparison of Selective Laser Melting and Hot Pressing," Materials (Basel). DOI:10.3390/ma6125700.

[38] Schwab, H., Prashanth, K., Löber, L., Kühn, U., and Eckert, J., 2015, "Selective Laser Melting of Ti-45Nb Alloy," Metals (Basel). DOI:10.3390/met5020686.

[39] Li, Y., Yang, C., Zhao, H., Qu, S., Li, X., and Li, Y., 2014, "New Developments of Ti-Based Alloys for Biomedical Applications," Materials (Basel). DOI:10.3390/ma7031709.

[40] Zhou, Y. L., and Luo, D. M., 2011, "Corrosion Behavior of Ti-Mo Alloys Cold Rolled and Heat Treated," J. Alloys Compd., 509(21), pp. 6267–6272.

[41] Grassi, S., Piattelli, A., de Figueiredo, L. C., Feres, M., de Melo, L., Iezzi, G., Alba, R. C., and Shibli, J. A., 2006, "Histologic Evaluation of Early Human Bone Response to Different Implant Surfaces," J. Periodontol., 77(10), pp. 1736–1743.

[42] Deligianni, D., Katsala, N., Ladas, S., Sotiropoulou, D., Amedee, J., and Missirlis, Y., 2001, "Effect of Surface Roughness of the Titanium Alloy Ti-6Al-4V on Human Bone Marrow Cell Response and on Protein Adsorption.," Biomaterials, 22(11), pp. 1241–51.

[43] Marticorena, M., Corti, G., Olmedo, D., Guglielmotti, M. B., and Duhalde, S., 2007, "Laser Surface Modification of Ti Implants to Improve Osseointegration," J. Phys. Conf. Ser., 59(1), pp. 662–665.

[44] Ng, C.-H., Chan, C.-W., Man, H.-C., Waugh, D., and Lawrence, J., 2016, "Modifications of Surface Properties of Beta Ti by Laser Gas Diffusion Nitriding," J. Laser Appl. DOI:10.2351/1.4944000.

[45] Dahotre, S. N., Vora, H. D., Rajamure, R. S., Huang, L., Banerjee, R., He, W., and Dahotre, N. B., 2014, "Laser Induced Nitrogen Enhanced Titanium Surfaces for Improved Osseo-Integration," Ann. Biomed. Eng. DOI:10.1007/s10439-013-0898-z.

[46] Razavi, R. S., Gordani, G. R., and Man, H. C., 2011, "A Review of the Corrosion of Laser Nitrided Ti-6Al-4V," Anti-Corrosion Methods Mater. DOI:10.1108/00035591111130523.

[47] Datta, S., Das, M., Balla, K., Bodhak, S., and Murugesan, V. K., 2018, "Mechanical, Wear, Corrosion and Biological Properties of Arc Deposited Titanium Nitride Coatings" DOI:10.1016/j.surfcoat.2018.03.019.

[48] Mareci, D., Chelariu, R., Gordin, D. M., Romas, M., Sutiman, D., and Gloriant, T., 2010, "Effect of Mo Content on Electrochemical Behaviour of TiMo Alloys for Dental

Applications," Mater. Corros., 61(10), pp. 829–837.

[49] Kumar, S., and Narayanan, T. S. N. S., 2008, "Corrosion Behaviour of Ti–15Mo Alloy for Dental Implant Applications," J. Dent., 36(7), pp. 500–507.

[50] Capela, M. V., Acciari, H. A., Capela, J. M. V., Carvalho, T. M., and Melin, M. C. S., 2008, "Repeatability of Corrosion Parameters for Titanium–Molybdenum Alloys in 0.9% NaCl Solution," J. Alloys Compd., 465(1–2), pp. 479–483.

[51] "Protocol for Preparing Simulated Body Fluid (SBF)," http://www.life.kyutech.ac.jp/~tmiya/SBF-e.html.

[52] Kato, Y., Windle, J. J., Koop, B. A., Mundy, G. R., and Bonewald, L. F., 2010, "Establishment of an Osteocyte-like Cell Line, MLO-Y4," J. Bone Miner. Res., 12(12), pp. 2014–2023.

[53] Mavrogenis, A. F., Dimitriou, R., Parvizi, J., and Babis, G. C., 2009, "Biology of Implant Osseointegration," J. Musculoskelet. Neuronal Interact., 9(2), pp. 61–71.

[54] Al-mana, O. A. A., 2011, "Laser Nitrided and TiN Coated Ti-6Al-4V Alloy Surfaces Omar A . Al-Mana," Dublin City University.

[55] Zháňal, P., Harcuba, P., Hájek, M., Smola, B., Stráský, J., Šmilauerová, J., Veselý, J., and Janeček, M., 2018, "Evolution of ω Phase during Heating of Metastable β Titanium Alloy Ti–15Mo," J. Mater. Sci., 53(1), pp. 837–845.

[56] Razavi, R. S., Salehi, M., Ramazani, M., and Man, H. C., 2009, "Corrosion Behaviour of Laser Gas Nitrided Ti-6Al-4V in HCl Solution," Corros. Sci. DOI:10.1016/j.corsci.2009.06.016.

[57] Yilbas, B. S., Khaled, M., Karatas, C., Uslan, I., Keles, O., Usta, Y., and Ahsan, M., 2006, "Electrochemical Properties of the Laser Nitrided Surfaces of Ti-6Al-4V Alloy," Surf. Coatings Technol., 201(3–4), pp. 679–685.

[58] Thair, L., Mudali, U. K., Rajagopalan, S., Asokamani, R., and Raj, B., 2003, "Surface Characterization of Passive Film Formed on Nitrogen Ion Implanted Ti-6Al-4V and Ti-6Al-7Nb Alloys Using SIMS," Corros. Sci., 45(9), pp. 1951–1967.

[59] Yilbas, B. S., Hashmi, M. S. J., and Shuja, S. Z., 2001, "Laser Treatment and PVD TiN Coating of Ti-6Al-4V Alloy," Surf. Coatings Technol. DOI:10.1016/S0257-8972(01)01038-6.

[60] Balla, V. K., Bhat, A., Bose, S., and Bandyopadhyay, A., 2012, "Laser Processed TiN Reinforced Ti6Al4V Composite Coatings," J. Mech. Behav. Biomed. Mater., 6, pp. 9–20.

[61] Perillo, P. M., 2015, "Corrosion Behaviour of Titanium Nitride Coating on Titanium and Zircaloy-4," Am. J. Mater. Sci. Appl., 3(2), pp. 18–25.

[62] Biswas, A., Li, L., Chatterjee, U. K., Manna, I., Pabi, S. K., and Dutta Majumdar, J., 2008, "Mechanical and Electrochemical Properties of Laser Surface Nitrided Ti-6Al-4V," Scr. Mater. DOI:10.1016/j.scriptamat.2008.03.020.

[63] Perry, A. J., Baouchi, A. W., Petersen, J. H., and Pozder, S. D., 1992, "Crystal Structure of Molybdenum Nitride Films Made by Reactive Cathodic Arc Evaporation," Surf. Coatings Technol. DOI:10.1016/S0257-8972(09)90060-3.

[64] Wysocki, B., Idaszek, J., Zdunek, J., Rozniatowski, K., Pisarek, M., Yamamot, A., and Swieszkowski, W., 2018, "The Influence of Selective Laser Melting (SLM) Process Parameters on In-Vitro Cell Response," Int. J. Mol. Sci. Artic.

DOI:10.3390/ijms19061619.

[65] Khang, D., Kim, S. Y., Liu-Snyder, P., Palmore, G. T. R., Durbin, S. M., and Webster, T. J., 2007, "Enhanced Fibronectin Adsorption on Carbon Nanotube/Poly(Carbonate) Urethane: Independent Role of Surface Nano-Roughness and Associated Surface Energy," Biomaterials, 28(32), pp. 4756–4768.

[66] Hove, R. P. Van, Nolte, P. A., Semeins, C. M., and Klein-nulend, J., 2012, "Differences in Proliferation , Differentiation , and Cytokine Production by Bone Cells Seeded on Titanium – Nitride and Cobalt – Chromium – Molybdenum Surfaces," 28(2), pp. 278–287.

[67] Brinkmann, J., Hefti, T., Schlottig, F., Spencer, N. D., and Hall, H., 2012, "Response of Osteoclasts to Titanium Surfaces with Increasing Surface Roughness: An in Vitro Study," Biointerphases DOI:10.1007/s13758-012-0034-x.

[68] Bodhak, S., Bose, S., and Bandyopadhyay, A., 2009, "Role of Surface Charge and Wettability on Early Stage Mineralization and Bone Cell-Materials Interactions of Polarized Hydroxyapatite," Acta Biomater., 5(6), pp. 2178–2188.

[69] Hallab, N. J., Bundy, K. J., O'Connor, K., Moses, R. L., and Jacobs, J. J., 2001, "Evaluation of Metallic and Polymeric Biomaterial Surface Energy and Surface Roughness Characteristics for Directed Cell Adhesion," Tissue Eng., 7(1), pp. 55–71.

[70] Kuzyk, P., and Schemitsch, E., 2011, "The Basic Science of Peri-Implant Bone Healing," Indian J. Orthop., 45(2), p. 108.

[71] Zhang, B., Bi, G., Nai, S., Sun, C. N., and Wei, J., 2016, "Microhardness and Microstructure Evolution of TiB2 Reinforced Inconel 625/TiB2 Composite Produced by Selective Laser Melting," Opt. Laser Technol., 80, pp. 186–195.

[72] Gao, Y., Zhang, D., Cao, M., Chen, R., Feng, Z., Poprawe, R., Schleifenbaum, J. H., and Ziegler, S., 2019, "Effect of δ Phase on High Temperature Mechanical Performances of Inconel 718 Fabricated with SLM Process," Mater. Sci. Eng. A, 767.

[73] Jia, Q., and Gu, D., 2014, "Selective Laser Melting Additive Manufacturing of Inconel 718 Superalloy Parts: Densification, Microstructure and Properties," J. Alloys Compd., 585, pp. 713–721.

[74] Amato, K. N., Gaytan, S. M., Murr, L. E., Martinez, E., Shindo, P. W., Hernandez, J., Collins, S., and Medina, F., 2012, "Microstructures and Mechanical Behavior of Inconel 718 Fabricated by Selective Laser Melting," Acta Mater., 60(5), pp. 2229–2239.

[75] Jia, Q., and Gu, D., 2014, "Selective Laser Melting Additive Manufactured Inconel 718 Superalloy Parts: High-Temperature Oxidation Property and Its Mechanisms," Opt. Laser Technol., 62, pp. 161–171.

[76] Shaikh, A. S., *Development of a γ' Precipitation Hardening Ni-Base Superalloy for Additive Manufacturing*.

[77] Slama, C., and Abdellaoui, M., 2000, *Structural Characterization of the Aged Inconel 718*.

[78] Gao, B., Sui, Y., Wang, H., Zou, C., Wei, Z., Wang, R., and Sun, Y., 2019, "Effects of Cooling Rate on the Solidification and Microstructure of Nickel-Based Superalloy GTD222," Materials (Basel)., 12(12).

[79] Kunze, K., Etter, T., Grässlin, J., and Shklover, V., 2015, "Texture, Anisotropy in Microstructure and Mechanical Properties of IN738LC Alloy Processed by Selective Laser Melting (SLM)," Mater. Sci. Eng. A, 620, pp. 213–222.

[80] Carter, L. N., Attallah, M. M., and Reed, R. C., 2012, *Laser Powder Bed Fabrication of Nickel-Base Superalloys: Influence of Parameters; Characterisation, Quantification and Mitigation of Cracking*.

[81] Lee, G., Olevsky, E. A., Manière, C., Maximenko, A., Izhvanov, O., Back, C., and McKittrick, J., 2018, "Effect of Electric Current on Densification Behavior of Conductive Ceramic Powders Consolidated by Spark Plasma Sintering," Acta Mater., 144, pp. 524–533.

[82] Congyuan Zeng, Bin Zhang, Ali Hemmasian Ettefagh, Hao Wen, Hong Yao, W.J. Meng, Shengmin Guo, Mechanical, thermal, and corrosion properties of Cu-10Sn alloy prepared by laser-powder-bed-fusion additive manufacturing, Additive Manufacturing, Volume 35, 2020, 101411, ISSN 2214-8604, https://doi.org/10.1016/j.addma.2020.101411.

[83] Zhang, D., Niu, W., Cao, X., and Liu, Z., 2015, "Effect of Standard Heat Treatment on the Microstructure and Mechanical Properties of Selective Laser Melting Manufactured Inconel 718 Superalloy," Mater. Sci. Eng. A, 644, pp. 32–40.

[84] Kanagarajah, P., Brenne, F., Niendorf, T., and Maier, H. J., 2013, "Inconel 939 Processed by Selective Laser Melting: Effect of Microstructure and Temperature on the Mechanical Properties under Static and Cyclic Loading," Mater. Sci. Eng. A DOI:10.1016/j.msea.2013.09.025.

[85] Jahangiri, M., 2019, "Different Effects of Γ′ and η Phases on the Physical and Mechanical Properties of Superalloys," J. Alloys Compd., 802, pp. 535–545.

[86] Zhang, F., Reich, M., Kessler, O., and Burkel, E., 2013, "The Potential of Rapid Cooling Spark Plasma Sintering for Metallic Materials," Mater. Today, 16(5), pp. 192–197.

[87] Voisin, T., Monchoux, J. P., Hantcherli, M., Mayer, S., Clemens, H., and Couret, A., 2014, "Microstructures and Mechanical Properties of a Multi-Phase β-Solidifying TiAl Alloy Densified by Spark Plasma Sintering," Acta Mater., 73, pp. 107–115.

[88] Ma, M., Wang, Z., and Zeng, X., 2017, "A Comparison on Metallurgical Behaviors of 316L Stainless Steel by Selective Laser Melting and Laser Cladding Deposition," Mater. Sci. Eng. A, 685, pp. 265–273.

[89] Kiss, A. M., Fong, A. Y., Calta, N. P., Thampy, V., Martin, A. A., Depond, P. J., Wang, J., Matthews, M. J., Ott, R. T., Tassone, C. J., Stone, K. H., Kramer, M. J., van Buuren, A., Toney, M. F., and Nelson Weker, J., 2019, "Laser-Induced Keyhole Defect Dynamics during Metal Additive Manufacturing," Adv. Eng. Mater., 21(10).

[90] Zhaohui, Z., Fuchi, W., Lin, W., Shukui, L., and Osamu, S., 2008, "Sintering Mechanism of Large-Scale Ultrafine-Grained Copper Prepared by SPS Method," Mater. Lett., 62(24), pp. 3987–3990.

[91] Diouf, S., and Molinari, A., 2012, "Densification Mechanisms in Spark Plasma Sintering: Effect of Particle Size and Pressure," Powder Technol., 221, pp. 220–227.

[92] Song, S. X., Wang, Z., and Shi, G. P., 2013, "Heating Mechanism of Spark Plasma Sintering," Ceram. Int., 39(2), pp. 1393–1396.

[93] Perera, D. S., Tokita, M., and Moricca, S., 1998, "Comparative Study of Fabrication of Si3N4/SiC Composites by Spark Plasma Sintering and Hot Isostatic Pressing," J. Eur. Ceram. Soc., 18(4), pp. 401–404.

[94] Liu, R., Wang, W., Chen, H., Lu, Z., Zhao, W., and Zhang, T., 2019, "Densification of Pure Magnesium by Spark Plasma Sintering-Discussion of Sintering Mechanism," Adv.

Powder Technol., 30(11), pp. 2649–2658.

[95] Khoshghadam-Pireyousefan, M., Mohammadzadeh, A., Heidarzadeh, A., and Brabazon, D., 2021, "Fundamentals of Spark Plasma Sintering for Metallic, Ceramic, and Polymer Matrix Composites Production," *Reference Module in Materials Science and Materials Engineering*, Elsevier DOI:10.1016/b978-0-12-803581-8.11907-1.

[96] VACUUM ALLOYS, "Https://Cannonmuskegon.Com/Products/Vacuum-Alloys/."

[97] Long, F., Yoo, Y. S., Jo, C. Y., Seo, S. M., Jeong, H. W., Song, Y. S., Jin, T., and Hu, Z. Q., 2009, "Phase Transformation of η and σ Phases in an Experimental Nickel-Based Superalloy," J. Alloys Compd., 478(1–2), pp. 181–187.

[98] Sun, W., Qin, X., Guo, J., Lou, L., and Zhou, L., 2015, "Microstructure Stability and Mechanical Properties of a New Low Cost Hot-Corrosion Resistant Ni-Fe-Cr Based Superalloy during Long-Term Thermal Exposure," Mater. Des., 69, pp. 70–80.

[99] Oh, J. H., Choi, I. C., Kim, Y. J., Yoo, B. G., and Jang, J. il, 2011, "Variations in Overall- and Phase-Hardness of a New Ni-Based Superalloy during Isothermal Aging," Mater. Sci. Eng. A, 528(19–20), pp. 6121–6127.

[100] Westbrook, J. H., 1957, "Temperature Dependence of the Hardness of Secondary Phases Common in Turbine Bucket Alloys," JOM, 9(7), pp. 898–904.

[101] Zhang, P., Li, S. X., and Zhang, Z. F., 2011, "General Relationship between Strength and Hardness," Mater. Sci. Eng. A, 529(1), pp. 62–73.

[102] Ming, K., Bi, X., and Wang, J., 2018, "Realizing Strength-Ductility Combination of Coarse-Grained Al0.2Co1.5CrFeNi1.5Ti0.3 Alloy via Nano-Sized, Coherent Precipitates," Int. J. Plast., 100, pp. 177–191.

[103] Long, F., Yoo, Y. S., Jo, C. Y., Seo, S. M., Song, Y. S., Jin, T., and Hu, Z. Q., 2009, "Formation of η and σ Phase in Three Polycrystalline Superalloys and Their Impact on Tensile Properties," Mater. Sci. Eng. A, 527(1–2), pp. 361–369.

[104] Hu, X.-A., Zhao, G.-L., Liu, F.-C., and Liu, W.-X., "Microstructure and Mechanical Behavior of Inconel 625 Alloy Processed by Selective Laser Melting at High Temperature up to 1000 °C" DOI:10.1007/s12598-019-01321-3.

[105] Xu, Z., Murray, J. W., Hyde, C. J., and Clare, A. T., *Effect of Post Processing on the Creep Performance of Laser Powder Bed Fused Inconel 718 A*.

[106] "Four Basic Types of Fracture Mechanisms | Gear Solutions Magazine Your Resource to the Gear Industry."

[107] Park, S. Y., Kim, K. S., Kim, M. C., Kassner, M. E., and Lee, K. A., 2020, "Effect of Post-Heat Treatment on the Tensile and Cryogenic Impact Toughness Properties of Inconel 718 Manufactured by Selective Laser Melting," Adv. Eng. Mater., 2001005, pp. 1–10.

[108] Caliari, F. R., Candioto, K. C. G., Reis, D. A. P., Couto, A. A., Neto, C. D. M., and Nunes, C. A., 2011, "Study of the Mechanical Behavior of an Inconel 718 Aged Superalloy Submitted Study of the Mechanical Behavior of an Inconel 718 Aged Superalloy Submitted to Hot Tensile Tests," (October) DOI:10.4271/2011-36-0328.

[109] Royal Society (Great Britain), *Machine Learning : The Power and Promise of Computers That Learn by Example*.

[110] Géron, A., *Hands-On Machine Learning with Scikit-Learn and TensorFlow*.

[111] Schmidt, J., Marques, M. R. G., Botti, S., and Marques, M. A. L., 2019, "Recent

Advances and Applications of Machine Learning in Solid-State Materials Science," npj Comput. Mater., 5(1).

[112] Ramprasad, R., Batra, R., Pilania, G., Mannodi-Kanakkithodi, A., and Kim, C., 2017, "Machine Learning in Materials Informatics: Recent Applications and Prospects," npj Comput. Mater., 3(1).

[113] Dodaran, M., Ettefagh, A. H., Guo, S. M., Khonsari, M. M., Meng, W. J., Shamsaei, N., and Shao, S., 2020, "Effect of Alloying Elements on the γ' Antiphase Boundary Energy in Ni-Base Superalloys," Intermetallics, 117.

[114] Rajan, K., 2005, "Materials Informatics," Mater. Today, 8(10), pp. 38–45.

[115] Lecun, Y., Bengio, Y., and Hinton, G., 2015, "Deep Learning," Nature, 521(7553), pp. 436–444.

[116] Alexander Amini, A. S., "Introduction to Deep Learning."

[117] "Evaluating Performance of an Object Detection Model | by Renu Khandelwal | Towards Data Science."

[118] "Sklearn.Neighbors.KNeighborsRegressor — Scikit-Learn 0.24.1 Documentation."

[119] Francis, J., and Bian, L., 2019, "Deep Learning for Distortion Prediction in Laser-Based Additive Manufacturing Using Big Data," Manuf. Lett., 20, pp. 10–14.

[120] Sumit Saha. A Comprehensive Guide to Convolutional Neural Networks. 2018. Available online: https://towardsdatascience.com/a-comprehensive-guide-to-convolutional-neural-networks-the-eli5-way-3bd2b1164a53 (ac-cessed o n 30 Mar 2021).

[121] Bochkovskiy, A.; Wang, C.Y.; Liao, H.Y.M. YOLOv4: Optimal Speed and Accuracy of Object Detection. arXiv 2020, arXiv : 2004.10934.

[122] Redmon, J.; Farhadi, A. YOLOv3: An Incremental Improvement. arXiv 2018, arXiv: 1804.02767, ISSN: 23318422, 2018.

[123] Wu, Y.; Kirillov, A.; Massa, F.; Lo, W.Y.; Girshick, R. Detectron2: A PyTorch-Based Modular Object Detection Library. 2019. Available online: https://ai.facebook.com/blog/-detectron2-a-pytorch-based-modular-object-detection-library-/ (accessed on 28 Jan 2021).

[124] Wu, Y.; Kirillov, A.; Massa, F.; Yen, W.; Lo, R.G. Detectron2. 2019. Available online: https://github.com/facebookresearch/detectron2 (accessed on 14 Jan 2021).

[125] Ross, G.; Ilija, R.; Georgia, G.; Piotr Doll, K.H. Detectron. 2018. Available online: https://github.com/facebookresearch/Detectron (accessed on 14 Jan 2021).

[126] Wang, C.-Y.; Liao, H.-Y.M.; Yeh, I.-H.; Wu, Y.-H.; Chen, P.-Y.; Hsieh, J.-W. CSPNET: ANew Backbone that can Enhence Learning Capability of, C.N.N. ArXiv 2019, ArXiv: 1911.11929v1.

[127] He, K.; Zhang, X.; Ren, S.; Sun, J. Spatial Pyramid Pooling in Deep Convolutional Networks for Visual Recognition. ArXiv 2015, ArXiv: 1406.4729v4.

[128] Liu, S.; Qi, L.; Qin, H.; Shi, J.; Jia, J. Path Aggregation Network for Instance Segmentation. ArXiv 2018, ArXiv: 1803.01534v4.

[129] Redmon, J.; Farhadi, A. YOLOv3: An Incremental Improvement. arXiv 2018, arXiv: 1804.02767, ISSN: 23318422, 2018.

[130] Solawetz, J. Breaking down YOLOv4. 2020. Available online:

https://blog.roboflow.com/a-thorough-breakdown-of-yolov4/ (accessed on 28 Jan01 2021).

[131] Rugery, P. Explanation of YOLO V4 a One Stage Detector. Available online: https://becominghuman.ai/explaining-yolov4-a-one-stage-detector-cdac0826cbd7 (accessed on 28 Jan01 2021).

[132] Tan, M., Pang, R., and Le, Q. V., 2020, EfficientDet: Scalable and Efficient Object Detection DOI:10.1109/CVPR42600.2020.01079.

[133] Honda, H. Digging into Detectron 2—Part 1-5. Available online: https://medium.com/@hirotoschwert/digging-into-detectron-2-part-5-6e220d762f9 (accessed on 29 Jan 2021).

[134] Pham, V.; Pham, C.; Dang, T. Road Damage Detection and Classification with Detectron2 and Faster R-CNN. ArXiv 2020, ArXiv: 2010.15021.

[135] Lin, T. LabelImg. 2017. Available online: https://github.com/tzutalin/labelImg (accessed on 13 Jan 2021).

[136] Wada, K. Labelme: Image Polygonal Annotation with Python. 2016. Available online: https://github.com/wkentaro/labelme (accessed on 13 Jan 2021).

[137] Google.Welcome to Colaboratory." . Available online: https://colab.research.google.com/notebooks/intro.ipynb#scrollTo=5fCEDCU_qrC0 (accessed on 26 Jan 2021).

[138] Bochkovskiy, A. Darknet. Github. 2020. Available online: https://github.com/AlexeyAB/darknet (accessed on 26 Jan 2021).

[139] YOLOv4 Training Tutorial. Available online: https://colab.research.google.com/drive/1_GdoqCJWXsChrOiY8sZMr_zbr_fH-0Fg?usp=sharing (accessed on 26 Jan 2021).

[140] Francesc Munoz-Martin, J., and Ying, X., An Overview of Overfitting and Its Solutions. J. Phys.: Conf. Ser. 2019, 1168 022022 , doi:10.1088/1742-6596/1168/2/022022.

[141] Tai, S.-K., Dewi, C., Chen, R.-C., Liu, Y.-T., Jiang, X., and Yu, H., 2020, "Deep Learning for Traffic Sign Recognition Based on Spatial Pyramid Pooling with Scale Analysis," Appl. Sci., 10(19), p. 6997.

[142] Lawal, M. O., 2021, "Tomato Detection Based on Modified YOLOv3 Framework," Sci. Rep., 11(1), p. 1447.

[143] Jing, J., Zhuo, D., Zhang, H., Liang, Y., and Zheng, M., 2020, "Fabric Defect Detection Using the Improved YOLOv3 Model," J. Eng. Fiber. Fabr., 15, p. 155892502090826.

[144] Detectron2/MODEL_ZOO.Md at Master Facebookresearch/Detectron2. Available online: https://github.com/facebookresearch/detectron2/blob/master/ (accessed on 27 Feb 2021).

Vita

Hao Wen was born in Shanxi, China, in 1989. He graduated from Jimei Univeristy, Fujian, China, and received his Bachelor Degree in Marine Engineering in June 2012. In May 2014, he grauated from Stevens Institute of Technology and received his Master's Degree in Maritime Systems. In January 2018, he enrolled in the Department of Mechanical Enginnering, Louisiana State University, as a Ph.D student under the supervision of Dr. Shengmin Guo, and he transferred to Engineering Science program in 2019.